IMPERIAL COLLEGE LONDON

DEPARTMENT OF LIFE SCIENCES

FLUID FLOW IN THE BRAIN PARENCHYMA DURING SLEEP AND SEDATION: A CRITICAL TEST OF THE GLYMPHATIC HYPOTHESIS

Andawei Miao

SUBMITTED IN PART FULFILMENT OF THE REQUIREMENTS FOR THE DEGREE OF DOCTOR OF PHILOSOPHY IN LIFE SCIENCES OF IMPERIAL COLLEGE LONDON

JANUARY 2023

Declaration

I declare that all material presented in this thesis is my own work unless otherwise stated and if so, it has been properly referenced.

Copyright

Abstract

The reasons we have to sleep have baffled neuroscientists for decades. A recently proposed glymphatic hypothesis suggested that one of the purposes of sleep is to clean toxic metabolites from the brain during sleep. Since the introduction of this idea, there have been controversies. The glymphatic hypothesis claimed that there is bulk flow in the brain parenchyma that actively sweeps metabolic wastes from the periarterial space towards the perivenous space, and this clearing effect is only turned-on during sleep. However, so far there is not a single published study that has directly tested the movement of fluid in the brain parenchyma which is supposed to be increased during sleep. In this study, a novel method utilising fluorescence recovery after photo-bleaching in combination with a fibre-optic photometry system was developed. This allows an absolute number of diffusion coefficient to be measured in the parenchyma of freely behaving mice. At the same time, a miniature brain activity logger that attached on to the animal skull continuously measures EEG/EMG activity of the brain. Combining these two approaches, fluid flow rates in the brain parenchyma were compared between different vigilance states of the animal and during sedation. The data collected indicated that local fluid flow rate in the frontal cortex of the parenchyma stays unchanged regardless to the vigilance states or sedation by dexmedetomidine and is not affected by circadian time of the day. The results suggested fluid flow in the parenchyma is diffusive. This conclusion does not support the proposed glymphatic hypothesis.

Acknowledgements

I would like to express my sincere gratitude to my esteemed supervisors: Professor Nicholas Franks and Professor William Wisden for the invaluable advice and most generous support at every stage of the project. Without their help, I would not be able to learn how science works and produce such fruitful research results. The knowledge, confidence, encouragement, and inspiration they have given to me will carry me through all the challenges I will be facing for the rest of my entire life.

我要感谢我的父母对我的养育之恩，以及对我项目期间毫无保留的关怀。感谢父母在童年、少年期间对我性格、品行、理想、能力潜移默化的影响。感谢他们使我成长为了一个有理想有能力的年轻人。

I would like to give very special thanks to Bryan Hsieh, my trusted friend, co-author, teammate, and flatmate. Without his generous help and strong faith, I would not be able to experience a smooth and enjoyable research and life experience during my PhD study in London.
海內存知己，天涯若比鄰。永遠不會忘記在倫敦與我並肩奮鬥的蟹老板。

Special thanks are given to my Shifu, Dr Edward Harding, who introduced me into research life and lab experiments. I wish all the best for his career in research.

I would like to thank the members and previous members of the lab: Raquel, Mathieu, Panos, Kyoko, Berta, Wei, Xiao, Giulia, Chris and Ed for work-related and emotional supports from day to day.

感谢那个曾经在英国陪我走过了最艰难、最美好日子的人，是你给了我勇气，修炼了我的性格，让我有勇气去自信、细致、乐观地热爱生活、面对人生。

最后，感谢在英国的和曾经在英国的，我记忆中的朋友们。

This project, tuition fees and living expenses of the PhD programme were supported by the Medical Research Council and the UK Dementia Research Institute.

Table of Contents

List of Publications during PhD

Harding, E. C., Yu, X., **Miao, A.**, Andrews, N., Ma, Y., Ye, Z., Lignos, L., Miracca, G., Ba, W., Yustos, R., Vyssotski, A. L., Wisden, W. & Franks, N. P. (2018). A Neuronal Hub Binding Sleep Initiation and Body Cooling in Response to a Warm External Stimulus. *Current biology*: CB, 28(14), 2263–2273.e4.

Ma, Y., Miracca, G., Yu, X., Harding, E. C., **Miao, A.**, Yustos, R., Vyssotski, A. L., Franks, N. P. & Wisden, W. (2019). Galanin Neurons Unite Sleep Homeostasis and α2-Adrenergic Sedation. *Current biology*: CB, 29(19), 3315–3322.e3.

Tossell, K., Yu, X., Soto, B.A., Vicente, M., Miracca, G., Giannos, P., **Miao, A.**, Hsieh, B., Ma, Y., Yustos, R., Vyssotski, A. L., Constandinou, T., Franks, N. P. & Wisden, W. (2020). Sleep deprivation triggers somatostatin neurons in prefrontal cortex to initiate nesting and sleep via the preoptic and lateral hypothalamus. *BioRxiv.* (Submitted; under review).

List of Abbreviations

ACSF - Artificial Cerebrospinal Fluid

APP - Amyloid Precursor Proteins

AQP-4 - Aquaporin-4

Aβ - β-amyloid

BBB - Brain-Blood Barrier

CNS - Central Nerve System

CSF - Cerebrospinal Fluid

DEX - Dexmedetomidine

EEG - Electroencephalogram

EMG - Electromyograph

FPC - Fibre Photometry Console

FRAP - Fluorescent Recovery After Photo-bleaching

$GABA_A$ - γ-aminobutyric Acid Type A

ISF - Interstitial Fluid

ISO - Isoflurane

MRI - Magnetic Resonance Imaging

NREM - Non-Rapid Eye Movement

REM - Rapid Eye Movement

PBS – Phosphate Buffered Saline

RTI - Real-Time Iontophoretic

TMA - Tetramethyl-Ammonium

Chapter 1 Introduction

1.1 Why do we sleep?

From the brain-less cnidarian of *Hydra* to the intelligent life of humans, sleep, or sleep-like behaviours are evolutionarily conserved across the animal kingdom (Kanaya *et al*., 2020; Anafi *et al*., 2019). In mammals, sleep can be defined as a rapidly reversable state with limited responsiveness, reduced motor activity and reduced metabolism (Siegel, 2009). Being unconscious with drastically reduced vigilance poses great risk to an organism's survivability, yet sleep is undeniable. Acute sleep deprivation in animals and humans reveals that loss of sleep significantly impairs one's cognitive ability and immune functions (Alhola and Polo-Kantola, 2007; Besedovsky *et al*., 2012, Dijk and Landolt, 2019). Chronic sleep loss in humans has also been associated with health consequences such as obesity, diabetes, cardiovascular diseases and anxiety (Cooper *et al.*, 2018; Grandner *et al.*, 2016; McMakin and Alfano, 2015; Khan and Aouad, 2017). Sleep is found to be vital to the survival of animal since complete sleep restriction in animals can cause detrimental effects on the body systems and forced sleep deprivation can eventually lead to the death of the organism (Rechtschaffen *et al.*, 1983; Bentivoglio *et al*., 1997; Vaccaro *et al.*, 2020). Despite the absolute necessity of sleep, the exact physiological reasons that why do we sleep have baffled scientists for centuries. Evidenced from animal observation, sleep deprivation studies and more recent dissection of the neuronal circuits for sleep regulation, several theories have been proposed, trying to answer the most mysterious question of modern neuroscience.

1.1.1 Sleep for inactivity

Endothermic animals living in the temperate climates such as bears, and certain birds enter a physiological state of hibernation known as torpor (a behaviour of unseasonal inactivation for energy conservation in some birds) when temperature or food supplies are too low. These animals temporarily cease self-maintaining of high body temperatures and stay inactive (Ruf and Geiserm, 2015). Such hibernation behaviours resemble a sleep-like state and imply similar

functions of sleep: to survive adversary environments, predators and other potential harm from the darkness of the night by staying inactive. According to the inactivity theory, sleep is described as an adaptive behaviour during which the duration of normal activity is optimistically regulated (Siegel, 2009). In fact, the ways how animals sleep is heavily dependent on the species' ecological niche, natural behaviour and their brain structures. Predatory animals with little adversary such as tigers and lions sleep the longest and deepest whereas herbivorous animals such as giraffes sleep for the shortest and spend much more time in high vigilance to avoid danger (Siegel, 2005). Animals grazing on low calorific-density food or marine bottom feeders may stay constantly awake (Gillooly *et al.*, 2001; Pryaslova *et al*., 2009) and marine mammals such as dolphins and killer whales may spend weeks in constant activity during the postpartum period and only sleep with half of the brain functioning (Lyamin *et al.*, 2005 & 2019). All these facts show that sleep patterns in animals are highly diverse and adaptable. Perhaps it is a species-specific adaptive behaviour that utilises time of inactivity to preserve energy for more time of efficient activity when risk is minimal, but survivability is optimal.

1.1.2 Sleep for energy conservation

Sleep is often accompanied by reduced physical activity and lower body temperature. Similar to the inactivation theory, a lowered metabolic rate helps to reduce the body's demand for energy during the period when it is least efficient to carry out survival behaviours such as hunting and mating (Brinkman *et al*., 2018). It has been reported for up to 10% of reduction of body metabolism and 25% brain metabolism observed during sleep in humans (Jung *et al.*, 2011; Madsen *et al.*, 1991). Energy conservation is paramount in newly born animals due to a large surface to volume ratio of their bodies, and this may partially explain why there is an increased demand for sleep among infants (Siegel, 2005).

1.1.3 Sleep for restoration

In recent years, development in neurobiology has started to shed new insights on the physiological roles that sleep may play for the survival of the organisms. When vertebrate animals sleep, electrical signatures are detectable in the brain and muscles which can be used to categorise sleep into different stages, namely non-rapid eye movement (NREM) and rapid eye

movement (REM) sleep. These electrical patterns are the results of bioelectrical oscillations induced by calcium activities of the neurones (Blumberg *et al.*, 2020). Species of mammals and birds may have considerably different brain circuitries and structural organisations to perform various levels of cognitive tasks (Krueger *et al.*, 2019). However, the fact that they share the very similar brain oscillations during sleep implies that the requirement of sleep may originate from a more fundamental level, for example, the regulation of cellular activity.

These new observation and evidence led to the restorative theory of sleep function which suggests that sleep is a neurological process purposed to replenish what has been depleted by intensive brain activity. In general, restorative sleep serves housekeeping functions such as the anabolism of brain macromolecules and the catabolism of waste products that maintain the essential structural and functional integrities of the brain (Frank and Heller, 2018). Sleep or sleep-like behavioural states are often accompanied by risky unconsciousness of the individual, which indicates if there are some functional needs of sleep, such process must be incompatible with being conscious. In other words, the physiological function of sleep could not be performed effectively when the animal is being consciously active.

Some evidence suggests that synaptic remodelling occurs during sleep to rebalance brain network. Such process may produce cognitive activity therefore must be carried out during sleep (Cirelli and Tononi, 2021). With the help of advanced multichannel electrophysiological recording and functional activity imaging, Adamantidis *et al.* (2019) indicated that the delta and theta oscillations which occur during NREM and REM sleep facilitate in network rebalancing and such oscillations may only be possible without normal brain activity. Furthermore, specific neuronal circuits in the preoptic area of the hypothalamus which initiate body cooling also simultaneously induce NREM sleep (Harding *et al.*, 2018). This further elaborates the idea of energy preservation during sleep. What makes the lowered body temperature more evidential for sleep functions is that although only 1 or 2 degrees of temperature drop is enough to induce the expression of cold-induced RNA binding proteins that are directly involved in the structural remodelling of neurones (Hoekstra *et al.*, 2019). Many sedative drugs which completely impairs normal brain cognitive activities are also able to reproduce similar changes in brain temperature (Franks, 2008).

Such comparisons suggest a strong mechanistic connection between unconsciousness and synaptic remodulation.

In summary, based on empirical evidence, the restorative theory proposed that sleep serves the function of restoring imbalanced cellular metabolism at the night which has been accumulated during a wakeful day. As a further development of the restorative theory, one recent hypothesis has drawn particular attention: the glymphatic hypothesis which describes a mechanistic model that the brain actively clears harmful metabolites during NREM sleep.

1.2 The glymphatic hypothesis of brain clearance

The glymphatic hypothesis proposed a possible function of sleep that many harmful brain metabolites such as amyloid beta are cleared out from the brain tissue, and this glymphatic function is predominantly active when the brain undergoes sleep (Jessen *et al.*, 2015). This idea is apparently able to fundamentally justify the necessity for sleep across the species of mammals and birds who share great similarities in their ways of sleeping. Since the introduction of this hypothesis by Maiken Nedergaard and colleagues in 2012, it had launched new frontiers in the fields of neurophysiology research, neurodegenerative disease research and research of sleep due to the innovative and inspirational natures of this profound idea. However, like any newly introduced hypothesis, the glymphatic system has been under substantial debate and controversies. The current study is purposed to critically assess the glymphatic hypothesis by challenging one of its most fundamental mechanistic assumptions from a biophysical point of view. Firstly, the precise details of the glymphatic model along with the experimental evidence supporting the establishment of this model are to be introduced. In order to understand how the glymphatic system is supposed to function, types of brain fluids with their circulation and functions along with their key roles in the glymphatic pathway firstly need to be explained and emphasised on.

1.2.1 Brain fluids

Similar to many other organs, brain is a soft structure with high water content approximated at 80 per cents (Oros-Peusquens *et al.*, 2019). There are four main types of fluid existing in the brain:

the intracellular fluid, the cerebrospinal fluid (CSF), the interstitial fluid (ISF) and the blood in the vascular system. These fluids each has its origin and drainage and may interchange with each other. Collectively, these fluids support the cellular metabolism of brain cells by transporting nutrients to them and removing harmful by-products they generated (Sakka *et al.*, 2011).

Intracellular fluids are fluids found inside the brain cells which function as a solvent for biochemical reactions inside the cells. Intracellular fluid is contained by the cell membrane (Guyton and Hall, 2000). Water and the solutes of intracellular fluid may be exchanged with ISF in the extracellular space by crossing the cell membrane. In neurones, amyloid precursor proteins (APP) are formed in the intracellular fluid and transported to the cell membrane as a transmembrane protein concentrated at synaptic connections to regulate synaptic functions (Müller and Zheng, 2012). Transmembrane APP may undergo a series of sequential proteolytic cleavage resulting in the disassociation of it extracellular fragment, which becomes soluble amyloid beta peptides (Aβ) (Tomita *et al*., 1998). These soluble Aβ may aggregate into plaques which principally contribute to the pathological development of Alzheimer's disease. They may also be re-uptaken by the neurones and return to the intracellular fluids where they may again aggregate into plaques which are cytotoxic as well (O'brien and Wong, 2011; Lai and Mclaurin, 2011).

Cerebrospinal fluid is a colourless physiological fluid surrounding the brain and the spinal cord of all vertebrates. There are several main layers of structure between the cranium (skull bone) and the brain soft tissue (parenchyma) (Millen and Woollam, 1962), illustrated in Figure 1-1. From outer to inner, there are the dura mater, the arachnoid membrane and the pia mater in layers to form the meninges to separate the brain and spinal cord from the rest of the body (Greenberg *et al.*, 1994; Ghannam, 2019). Within the central nervous system (CNS), CSF is primarily contained in the subarachnoid space (Johanson *et al.*, 2008) and the brain ventricular system. The arachnoid membrane is loosely connected with the pia mater with the arachnoid trabeculae (a soft connective tissue formed by irregularly shaped fibroblast bridges) within the subarachnoid space (Haines and Mihailoff, 2017). There are also arterioles and venules in the subarachnoid space which can exchange with CSF relatively freely (Nakada and Kwee, 2019). The brain ventricular system consists of four interconnected cavities (the brain ventricles) in the brain (Lun *et al.*, 2015).

CSF is considered to be predominantly produced from the choroid plexuses of each of the ventricles (Kimelberg, 2004; Redzic, 2011). CSF is being produced continuously and circulating from the lateral ventricles to the third and fourth ventricles sequentially (Johanson *et al*., 2008; Brinker *et al*., 2014). The choroid plexuses are highly folded and vesiculated tissues formed by specialised ependymal epithelium layer attached to a basement membrane (Keep and Jones, 1990; Damkier *et al.*, 2013). At the choroid plexuses, a blood-CSF barrier is formed and the tight junctions between the ependymal cells control what macromolecules enter the CSF from the blood (Johanson *et al.*, 2008). In the brain, CSF serves several biological functions: firstly, it offers a mechanical buffer against physical injuries to the brain structure; secondary, it provides a circulating pathway for nutrients and hormonal signalling molecules during brain development and normal brain activities (Lehtinen *et al.*, 2013; Hladky and Barrand, 2014).

CSF is considered as a key component of the glymphatic system not only because the glymphatic function is directly measured by the influx of CSF into the parenchyma, but according to the glymphatic theory, when CSF exits the parenchyma, it drains into the parenchymal venous circulation and eventually joins the cervical lymphatic system and finally exits the brain (Johnston *et al.*, 2014; Murtha *et al.*, 2014; Jessen *et al*., 2015). Classically, CSF in the brain is found to be drained into the arachnoid villi and the meningeal lymphatics and then leaves the brain (Weed, 1914; Ma *et al.*, 2017). The glymphatic pathway has suggested a new route for CSF to leave the brain by convectively flow into the parenchyma. This convective flow is suggested to be driven by arterial and respirational pulsations (Hestre *et al.*, 2018; Klose, *et al.*, 2000; Yamada *et al.*, 2013; Jessen *et al*., 2015). Remarkably, the circulation of CSF in the cerebral aqueducts and the ventricles is due to the same cause (Nilsson *et al*., 1992; Egnor *et al.*, 2002; Johanson *et al.*, 2008; Brinker *et al.*, 2014; Abbott *et al.*, 2018; Khasawneh *et al.*, 2018).

Interstitial fluid (ISF) in the brain interstitium is a filtrate of the blood plasma by the blood capillaries walls. In the CNS, ISF fills the extracellular space between brain cells (Hladky and Barrand, 2014). Cellular metabolites secreted by the neurones or glial cells must first enter the ISF before being transported outside the brain. ISF provides an aqueous environment for nutrient transport, cell signalling and waste removal among brain cells (Abbott, 2004). According to the glymphatic model, CSF influx must first join the ISF by convective flow before the solutes are

carried to the drainage sink. The flow of ISF heavily impacts on the removal of toxic solutes in the ISF. It is therefore a key step in the brain clearance, and this shall be discussed in detail in Section 1.5.

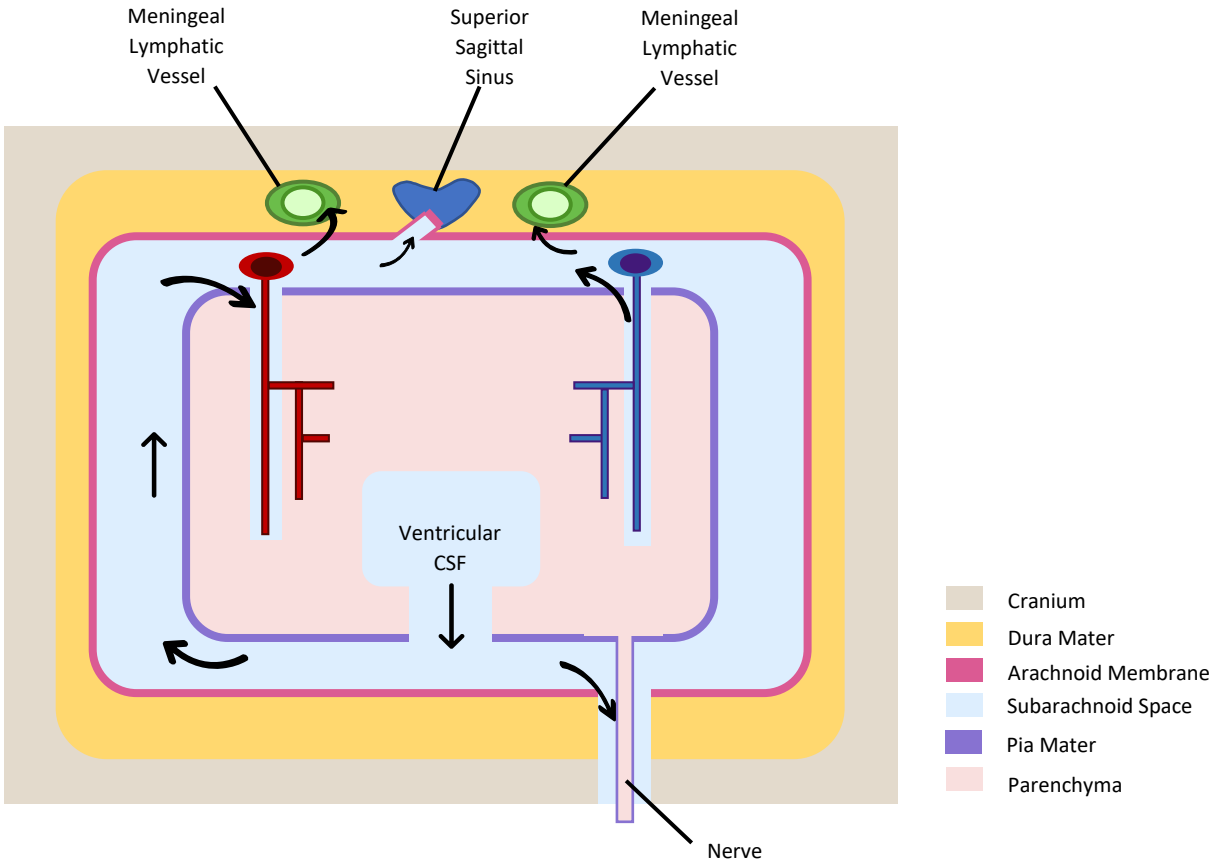

Figure 1-1 A schematic fluid circulation in the brain. Brain cranium and layers of the meninges are shown in different colours. Arrows shows the possible routes for CSF flow. Penetrating artery and arterioles are shown in red colour on the left-hand side. Veins and venioles are shown in blue on the right-hand side. Figure adapted from Kaur *et al.*, (2021).

1.2.2 Brain vasculature

The brain is supplied with a comprehensive vasculature system due to its high metabolic rate and energy demand. The blood supply for the brain is divided into anterior cerebral circulation and posterior cerebral circulation. The anterior cerebral circulation supplies blood to the cerebral cortex of the two hemispheres and the posterior cerebral circulation supplies to the cerebellum and the brain stem (Prince and Ahn, 2013). At the surface of the cortex, cerebral arteries develop into pial arteries and then further stem into numerous arterioles which penetrate into the parenchyma to provide blood supplies to the tissue. The organisation of artery and arteriole vasculatures at the cortical surface is illustrated in the schematic of Figure 1-2. These penetrating arterioles gradually narrow into blood capillaries which are lined by a single layer of endothelial cells interconnected with tight junctions (Kulik *et al*., 2008). Both the parenchyma and the capillary endothelial wall are supported with extracellular matrix known as the basal lamina. The basal lamina is also lined with a layer of leptomeningeal cells which together with capillary endothelial cells constitute to the formation of the brain-blood barrier (BBB) (Daneman and Prat, 2015). The space between the blood vessel and the boundary of parenchyma is termed as the perivascular space, also known as the Virchow-Robin space (Woollam and Millen, 1954; Zhang *et al.*, 1990). The perivascular space is filled with CSF. This histological location is a key component of the glymphatic system because CSF is supposed to exchange with the blood at the perivascular space (Jessen *et al.*, 2015).

The basal lamina is formed by fibrous proteins primarily laminin, fibronectin, and collagens to provide the physical structure of the BBB which limits immune cells entering the brain parenchyma (Muldoon *et al.*, 2013). There are also pericytes in the basal lamina which are supportive cells facilitating the survival of the endothelial cells and maintaining the permeability and vesicular trafficking across the BBB (Daneman *et al.*, 2010). These structural organisations of the BBB tightly limit its permeability. Along with the lack of conventional lymphatic system, the waste removal process in the brain faces substantial challenges.

The basal lamina is secreted by the astrocytes which are star-shaped glial cells that send protruding cell bodies to surround the basal lamina. Glial cells are non-neuronal brain cells

serving supportive functions to maintain optimal biochemical environments for the neurones to function effectively (Sofroniew and Vinters, 2010); in this case astrocytes send their vascular endfeet to form a tunnel-like structure that surrounds the basal lamina. Astrocyte endfeet are interconnected with gap junctions. This histological site of astrocytes endfeet surrounding around the blood capillaries is the primary location proposed in the glymphatic model where the convective exchange of blood with the toxin-containing ISF takes place. There are aquaporin-4 channel (AQP-4), a transmembrane; water-permeating channel protein (Saddoun and Papadopoulos, 2010), concentrated on these astrocyte endfeet which are supposed to play key roles in the glymphatic system (Iliff, *et al.,* 2012; Jessen *et al.*, 2015). Perivascular space surrounding veins and venioles is referred to as perivenous spaces. According to the glymphatic theory, CSF is continuously interchanged with ISF and exchanged ISF containing metabolic wastes drain out of brain at the perivenous space via the cervical lymphatic system (Iliff, *et al.,* 2012; Johnston *et al.*, 2004; Biceroglu *et al.*, 2012).

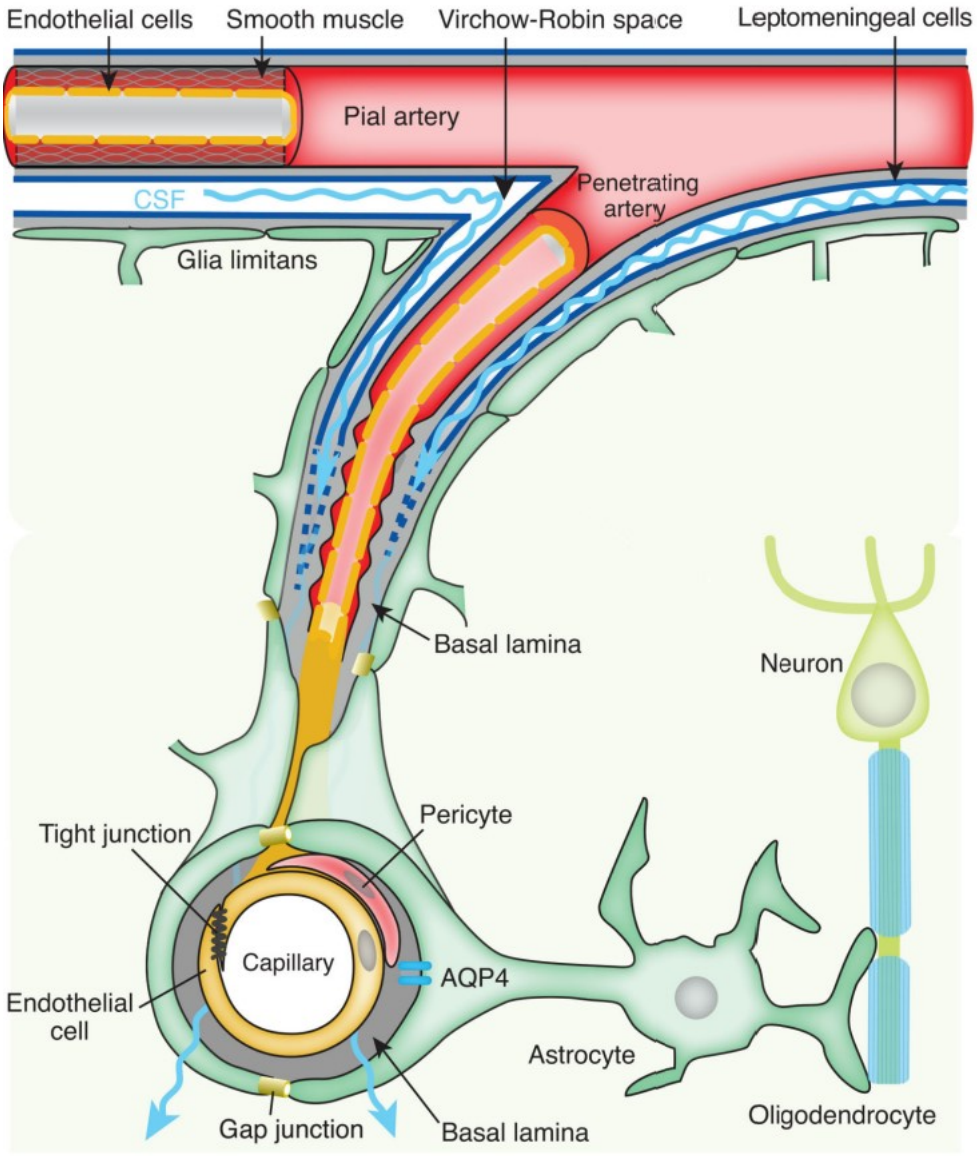

Figure 1-1 Schematic of the vasculature structure at the periarterial space. Details of the perivascular structure are described in the main text of 1.2.2. This diagram is acquired from Jessen *et al.* (2015).

1.3 The glymphatic hypothesis and its evidence

The glymphatic hypothesis was first proposed in 2012 which described a macroscopic pathway for the removal of toxic interstitial solutes. It states that: CSF at the periarterial space flows convectively into the extracellular space and exchanges with ISF and then re-joins the CSF at the perivenous space; during this process, harmful interstitial solutes are being actively cleared from the brain parenchyma; the convective movements of fluid are facilitated by AQP-4 water channels located on the astrocytic endfeet (Iliff, *et al.,* 2012; Jessen *et al.*, 2015). A schematic of the glymphatic pathway is illustrated in Figure 1-3.

1.3.1 Glymphatic function measured by CSF influx

Illiff *et al.* (2012) observed the movements of fluorescent tracer injected in the cisterna magna with two-photon microscopy in mouse brain. Cisterna magna is a relatively spacious cavity of the subarachnoid space at the back of the brain below the cerebellum. It is connected with the rest of the subarachnoid space, which is filled with CSF. Materials infused into the cisterna magna is able to quickly circulate around the brain and the ventricles (Norwood, *et al.*, 2019; Liu and Duff, 2008). Two-photon microscope is an advanced laser scanning microscope utilising the simultaneous excitation of the fluorophores by two photons for clearer image quality. Another advantage of two-photon microscopy is that it provides greater tissue penetration ability compared to traditional confocal microscopy (Cater and Shieh, 2015).

Investigations by Illif *et al.* (2012) measured the influx of fluorescent tracers at depth of 0-240 μm on the surface of the cortex by taking fluorescent images through an embedded transparent window in the cranium. Glymphatic function, measured as influx of fluorescent tracers from the CSF into the brain interstitium was imaged at time intervals after the infusion of the tracer at the cisterna magna. Tracers that are smaller in molecular weight (M.W. 3 kDa) were reported to enter the brain interstitium via the perivascular space more rapidly than lager tracers (M.W. 2000 kDa); as these lager tracers are observed to be retained in the perivascular space. Therefore, it was claimed that CSF influx convectively into the parenchyma via the perivascular space. The authors also reported this influx was significantly hindered in AQP-4 knockout mice, indicating the

functional role of AQP-4 channels in the glymphatic pathway. Meanwhile, fluorescence-labelled and radioactive-labelled soluble Aβ peptides ($A\beta_{1-40}$) were injected directly into the brain interstitium. It was observed to be presented in the perivascular space and reduction of total level of interstitial radioactivity was found at 1-2 hours post injection. AQP-4 knocked-out mice showed 55% less reduction of radioactivity compared to wild type.

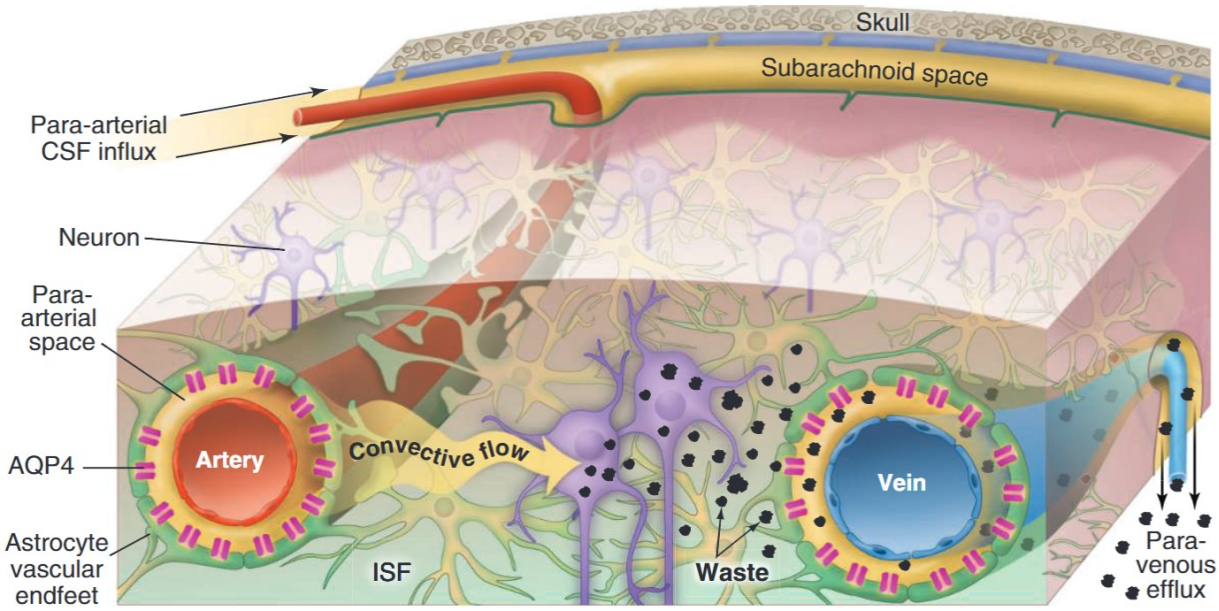

Figure 1-2 A schematic illustration of the glymphatic pathway. Details of the glymphatic pathway are described in the main text of Section 1.3. This diagram is acquired from Nedergaard (2013).

1.3.2 Glymphatic function enhanced during sleep and anaesthesia

Following the proposal of the glymphatic hypothesis, Nedergaard and group members moved on to investigate the proposed glymphatic function with sleep. Reported in Xie *et al.* (2013), similar two-photon imaging of the CSF influx of the intra-cisternally injected fluorescent tracer was observed to increase by a significant of 95% in so called "sleeping" mice compared with "awakened" mice. Similar increase of CSF influx was also observed in mice anesthetised with ketamine and xylazine.

The authors explained this increase of CSF influx by the increase of the volume of the interstitial space. This was measured by real-time iontophoretic (RTI) tetramethyl-ammonium (TMA) method. This method utilises an inert molecule that is released in pulses at one location of the parenchyma by a microelectrode and detected by another ion-selective microelectrode at a distal location. The changing of tracer concentration over time is recorded, and the volume fraction of the extracellular space as well as its tortuosity (λ) can be calculated from the recording (Odackal *et al.*, 2017; Xie *et al.* (2013) observed 13%-15% fractional volume of the interstitial space in so called "awakened" mice and 22-24% in so called "sleeping" and anesthetised mice. Interstitium tortuosity (λ) was reported to be approximately 1.5-1.6 and stay unchanged during "awakened", "sleeping" or anesthetised. (See section 1.4.2 for explanation of tortuosity).

In the study of Xie *et al.* (2013), habituated mice were physically constrained and had their heads fixed in position under the microscope throughout the experiments when CSF influx measurement and the RTI by TMA method were carried out. The authors carried out sleep/wake-related experiments only at specific time of the day to maximise the chances of animal falling asleep at 12 – 2 p.m., (presumably zeitgeber time 6-8 hours) or staying awake at 8 – 10 p.m. (presumably zeitgeber time 14-16 hours). Delta power band (0-4 Hz) of the recorded brain cortical electroencephalogram (EEG) was used to differentiate wake/sleep states. For maintaining "awakened" state of the animal, the authors manually woke mouse up by gentle handling their tails.

1.3.3 Glymphatic function reduced with aging

To further explore the implications of the glymphatic hypothesis, Nedergaard and group members moved on to testing the impact of aging on the glymphatic function by measuring CSF-ISF exchange at the perivascular space of aged mice (Kress *et al.*, 2014). Wild type mice were grouped at age 2-3 months, 8-10 months, and 18-20 months to represent young-age, middle-age, and old-age, respectively. CSF influx following intra-cisternal injection of fluorescent tracer measured by two-photon imaging and histology showed significant decrease in the old-age group. CSF efflux from the brain interstitium following parenchymal infusion of radioactive-labelled tracer measured by total interstitial radioactivity shows significant decrease in the old-age group. RTI by TMA method revealed the volume of interstitial space and the interstitial tortuosity stayed unchanged regardless of age.

1.4 Convection and diffusion

Solutes in the CSF and ISF including toxic metabolite such as Aβ circulate with these brain fluids. The glymphatic theory claims that convective flows of the CSF and ISF promote waste clearance predominantly during sleep. To understand how circulations and exchanges of ISF and CSF help to clear toxins, two physics concepts must be explained: convection and diffusion.

1.4.1 Advection

Heart pulses create blood pressure, which drives blood in the arteries or veins to flow directionally. As an analogy, when tree branches of different sizes fall into a flowing river, regardless to the sizes of the branches, they flow along with the river in the same pace. Motions of the molecules in the blood, analogous to the tree branches in the river are due to a pressure-driven bulk motion of the fluid, and this motion is known as “advection”. Therefore, the two main characteristic of advective flow are: (a) advective flow is directional; (b) the speed of substant movement is independent on its molecular size (Munson *et al.*, 2016).

1.4.2 Diffusion

On the other hand, diffusion becomes the predominant mode of substance movement when convection is not present. The kinetic theory states that molecules move randomly and constantly due to their kinetic energy. Diffusion occurs when molecules move randomly from a region of higher potential to a region of lower potential. The difference in potentials can be chemical potential, osmotic potential, pressure potential, energy potential, temperature potential and so on. Due to the nature of diffusive movement, the speed of a molecule that moves diffusively in a given environment is governed by its size, its kinetic energy (temperature) and the properties of the environment. Due to the randomness of the particle kinetics, in a homogenous environment, diffusion does not follow any preferred direction. Under physiological conditions, when a molecule diffuses in a substrate, the property of the environment considers the viscosity and tortuosity of the substrate. Viscosity describes how thick the substrate is, therefore the higher the viscosity, the more hydraulic resistance it poses against the spread of the diffusing molecule. The tortuosity describes the complexity and narrowness of the curvatures in the substrate for the diffusing molecule to spread into. A largely sized molecule will navigate more difficultly through a substrate with greater tortuosity, hence a lower diffusion rate. To summarise, under physiological conditions, diffusion of solute occurs when there is a concentration gradient and the rate of diffusion is governed by molecular weight of the molecule, temperature of the environment, viscosity, and tortuosity of the substrate.

1.4.3 Convection

When a hydraulic force drives the bulk flow of the substrate, advection and diffusion may happen simultaneously in tissues. At such instance, the much faster movements of solutes along with the bulk flow of the solvent dominates the diffusive component in terms of overall fluid motion. Under such circumstance, the mode of movement of the solute is considered as “convection”, in another word “convection = advection + diffusion”. Convection results from the bulk movement of the substrate (the solvent), therefore, convective flow is also referred to as “bulk flow”.

1.5 Controversies of the glymphatic hypothesis

Like any other newly introduced scientific hypothesis and model, the glymphatic hypothesis has stirred considerable controversies since its introduction. A large proportion of the experiments carried out by Nedergaard's original research evaluated glymphatic function by looking at the influx of CSF at the perivascular space. However, what happens next when following CSF had joining the parenchyma and mixing with the ISF remains largely unresolved.

1.5.1 CSF flows into the parenchyma

As described in Section 1.2.2, perivascular space (or the Virchow-Robin space) of the penetrating arteriole is a relative open space filled with CSF and is directly connected to the subarachnoid space. This relatively open space with less tortuosity offers less hydraulic resistance for molecules to flow convectively. There is little debate on the directional movement of CSF toward the parenchyma taking place at the periarterial space.

As early as in the 1980s, Rennels and colleagues (1985, 1990) had demonstrated the influx of horseradish peroxidase (a 44 kDa glycoprotein) from the CSF into the surface of the brain tissue just within a few minutes after the injection. Diffusion alone was not sufficient to explain such rapid penetration of tracer into the brain tissue. Such early experiments demonstrated the flow of CSF into the brain parenchyma along the perivascular space of the penetrating blood vessels for the first time. More recent experiments that demonstrate CSF influx towards the brain parenchyma were carried out mostly with magnetic resonance imaging (MRI). MRI uses artificial magnetic field and radio wave frequencies to interfere with the magnetic properties of protons inside the body. The reaction of protons to the magnetic field and radio wave frequencies is recorded and calculated with computational algorithms to reflex the organisation of soft tissues *in vivo* (Berger, 2002). A metal contrast agent can also be infused into the tissue in contrast-enhanced MRI. When infused in CSF, it acts as a tracer to report the circulation of CSF and to evaluate glymphatic functions indicated by CSF influx into the parenchyma. The glymphatic function has been observed with MRI using multiple computational models in animal models (Lee *et al.*, 2015; Davoodi-Bojd *et al.*, 2019; Elkin *et al.*, 2008 and 2020; Ratner *et al.*, 2015 and 2017;

Elkin *et al.*, 2018 and 2020) as well as in human CNS (Eide *et al.*, 2008 and 2018; Ringstad *et al.*, 2017; Watts *et al.*, 2019).

Using MRI to visualise glymphatic function has its main advantage of being non-invasive. MRI does not break the structural integrity of the brain nor interfere with the intracranial pressure, which may play roles in maintain glymphatic functions (Jiang, 2019). However, despite the using of contrast agents, MRI shows good results for the CSF influx with poor regional resolution when CSF exchanges with ISF within the brain tissue. Ratner *et al*. (2017) reported that CSF tracer influx showed well-defined streamline penetrating along the large arteries and wall of ventricles into the tissue, but the diffusive or convective mode of tracer movements at the streamline could not be successfully differentiated. Furthermore, due to the mechanistic nature of the MRI technology, the characterisation of tissue anatomy and tracer movement depends heavily on the computational models and algorithms applied. All these models and algorithms may interpret the resonance data differently, for example the Eulerian approach identifies and tracks the physical properties of fluid flow whereas the Lagrangian approach primarily focus on the tracking the movement of the tracer (Elkin *et al.*, 2020).

To summarise, in the original experiments proposing the glymphatic pathway (Illiff *et al.*, 2012), two-photon imaging through a sealed intercranial window was used to visualise CSF influx at the penetrating arteriole at a shadow level (240 μm) of the cortical surface. Various MRI observations confirmed this convective influx of tracer at the perivascular space. However, for the lymphatic pathway to function properly, CSF entered the parenchyma must continue to move convectively towards the perivenous spaces space for efflux. The obvious missing piece of the puzzle is that none of the abovementioned studies were able to demonstrate the convective flow of ISF from the periarterial space towards the perivenous space. In another word, using CSF influx as a sole indicator of glymphatic is less than satisfactory to test the glymphatic hypothesis conclusively.

1.5.2 A contradictive study

Smith and colleagues (2017) from the A.S. Verkman group conducted a series of *in vivo* experiment to test the glymphatic functions in rodents. Authors injected fluorescence-labelled tracers with different molecular weights intra-cisternally. CSF influx at the periarterial space was

visualised by *ex-vivo* slicing and imaging. Results showed the depths of penetration of tracers into the parenchyma was size-dependent, indicating a mode of movement predominantly not convective. Then, the authors injected the same tracers into the parenchyma and observed the spread of the trace *ex vivo* and found the same size-independent results. Next, the authors used a fluorescent recovery after photo-bleaching (FRAP) method (more details in Section 1.6.3) to conclude that the tracer movements in the cortical surface was not directional and the speed of tracer movement is highly comparable to diffusion. Next, the authors executed an acute cardiorespiratory arrest in the animal while measuring tracer movements in the cortical surface and found at the instant of losing cardiac and respiratory pulsatility, the movement of tracer in the cortical surface stayed unchanged. The authors finished the experiments by replicating the cisternal injection of fluorescent tracer and observed CSF influx in the perivascular space in AQP-4 knock-out mice and found no difference when compared with wild type mice. The authors concluded that their findings do not support the convective mode of solute transport in the brain parenchyma.

This study by Smith *et al.* (2017) provided multiple lines of evidence that directly investigated the predominant mode of solute transport in the parenchyma of rodent brains. Various studies attempted to explain the discrepancies between this and previous Nedergaard's studies. Mestre (2018) pointed out the slight change of instrumentation during the intra-cisternal inject could have resulted in dramatic difference of CSF infusion. Kaur *et al.*, (2021) pointed out that change in the sedatives used from ketamine/xylazine to avertin may induced less profound glymphatic functions as demonstrated by Hablitz *et al.* (2019). Despite these limitations, Smith *et al.* attempted to test the glymphatic hypothesis by evaluating ISF diffusion, which had great influence on the development of the current study.

1.5.3 Other objections against the glymphatic hypothesis

Apart from the missing evidence for ISF convection, the glymphatic hypothesis also faces challenges from various aspects. Hladky and Barrand (2014) have realised in Illiff *et al*. (2012) that with regarding to the histological distributions of ISF tracer, tracer preferentially stays in the periarterial space but not the perivenous space when the tracer was injected intra-cisternally.

However, when the tracer was injected into the parenchyma, the tracer efflux was found both in the periarterial and perivenous space. Hladky and Barrand speculated that mixing layers in the perivascular space may be responsible for such observations. They have also proposed an alternative explanation of the perivascular efflux of intra-cisternally injected tracer: between the arterial walls and the pial sheath, there are preferential routes for tracer movements, resulting in multi-directional movements of CSF in the perivascular space, which speed up the uptake of CSF by the surrounding parenchyma. This discrepancy has also been noticed by (Benveniste *et al.* 2018) who pointed out that in Illiff *et al*. (2012) influx and clearance of fluorescent labelled Aβ in AQP-4 knock-out mice took place at a different rate: at 30 min, influx of Aβ following cisternal infusion reduced by 40% in AQP-4 KO mice whereas efflux of Aβ following parenchymal injection only reduce by 20%. Hladky and Barrand (2014) also pointed out that in the study of Xie *et al.* (2013), the using of RTI by TMA quantification of the volume fraction extracellular space, flow between the micropipettes during sleep or wake could have potentially obscured the results.

1.5.4 The missing piece of the puzzle

The original work of Nedergaard and colleagues has successfully identified a potential route of CSF-ISF exchange responsible for brain clearance. However, the glymphatic model that relies on the convective flow of both CSF and ISF seems to be an overstatement. At least, with the evidence currently available, it is difficult to resolve the roles of ISF in the process of brain clearance. Further studies similar to Smith *et al.* (2017) where solute movement in the ISF is directly measured are needed. Since any metabolites secreted by the brain cell must enter the ISF before being removed from the brain. To clarify the flow pattern of ISF, as the missing piece of the puzzle, is crucial if the mechanisms of brain clearance are to be fully understood.

1.6 Flow in the brain interstitium

1.6.1 Measuring flow in the parenchyma

As a major component of solute transportation in the brain, ISF flow in the parenchyma has always been a focus for neurophysiological investigations. Traditionally, there has been heavy controversy over the mode of solute transport within the brain parenchyma, whether it is

diffusion or convection. With the introduction of the glymphatic hypothesis and its assumption that ISF convectively carries brain wastes from periarterial space to perivenous space, the debate between diffusion and convection has been again brought into attention.

As early as 1865, His (1865) injected colloidal materials into the brain tissue and observed perivascular spreading of material and he considered these perivascular ducts similar to the lymphatic pathways found in the peripheral tissue. This idea was surprisingly similar to the CSF influx proposed in the glymphatic hypothesis. Wood (1914) has perfused ferrocyanide in the Virchow-Robin space, later also known as the perivascular space and observed the tracer penetrated tissue with a pressure-dependent manner. Woollam and Millen (1992) used light microscope to describe the continuity of the subarachnoid space with the perivascular space but claimed that the perivascular space is largely sealed to the parenchyma. Brightman (1956) for the first time witnessed the CSF-ISF exchange at the perivascular space by infusing tracers into the CSF and observed under electron microscope. Later, Brightman and Reese (1969) claimed the convective movement of CSF towards the brain interstitium at the perivascular space. So far, early brain anatomists had observed and identified the importance of perivascular space as the primary histological location for CSF-ISF exchange and proposed a pattern of bulk flow between the two major brain fluids. However, movements within the ISF and subsequent ISF efflux has yet to be studied in detail.

In 1981 Cserr (1981) for the first time investigated the ISF flow motion by injecting radioactive tracers with greatly varying molecular weights into the brain parenchyma. He observed rates of tracer clearance from the brain during a 48-hour period after injection. This result suggested that the net clearance rate of the brain is size-independent. Assuming that the tracer had to leave the brain interstitium and join the CSF before being removed from the brain, these results indicated the dominant mode of solute transport in the brain parenchyma is size dependent, in another word, diffusive. However, this did not eliminate the possibility of local convection and preferential routes for ISF flow within the brain tissue. When reviewing many studied conducted in the late 20th century, Abbot (2004) concluded that ISF bulk flow exists along preferential pathways, in particular, along the perivascular spaces and the fibrous axons.

With the advancement in computation and MRI, recent studies continued to attempt for a clearer answer. Geer and Grossman (1997) injected tracers in brain tumours and mapped the tracer distribution over time. This was the first time when computational modelling in applied to characterise the flow pattern of injected tracer. Based on the diffusive models described previously (Nicholson, 1985), they concluded that tracer injected in the frontal lobes of rats diffuses locally, but at the same time preferentially spread along the axon tracks. More modelling studies confirmed that solute transport in the extracellular spaces of brain tissues is primarily diffusion instead of convection (Jin *et al.*, 2016; Hoter *et al.*, 2017). One of the main arguments that bulk flow is unlikely to exist in the extracellular space is its high hydraulic resistance. This means a tremendous amount of pressure is needed to present between the periarterial side and the perivenous side in order to drive the movement of ISF in between (Fenstermacher and Patlak, 1976; Thorne and Nicholson, 2006; Syková and Nicholson, 2008; Verkman, 2013; Wolak and Thorne, 2013; Pizzo *et al.*, 2018).

To summarise, the mode of transport for solutes within the ISF remains highly disputed. From the evidence brain anatomists collected from the past decades, it is more certain that CSF convectively moves within the perivascular space of the penetrating blood vessels, and this is consistent with the glymphatic hypothesis. To what extent CSF convectively exchanges with ISF in the perivascular space or with the tissues immediately adjacent to these spaces remains unclear. Given the huge hydraulic resistance of the interstitial environment, to what extent convection extends deeper in the tissue remain unresolved. There is convective flow in the ISF, preferentially along some anatomical structures such as the white matters, but what is the dominant mode of transport that affects the net ISF-CSF exchange requires further studies. Overall, the current debate on fluid flow in the parenchyma does not support the ISF convection aspect of the glymphatic hypothesis assumptions. Therefore, further studies to quantify diffusion in the brain parenchyma is necessary if the glymphatic hypothesis is to be critically tested.

1.6.2 Quantifying diffusion

Diffusion coefficient (D) describes the diffusivity of a diffusing molecule. According to the Fick's law (Fick, 1855), D is a proportionality constant between the molar flux of the diffusing molecule

and the concentration gradient. The molar flux of the diffusant describes the mass of the diffusing substance during a given time through an area normal to the direction of diffusion. Therefore, the dimension of diffusion coefficient is expressed as area per unit time, for example: $\mu m^2\ s^{-1}$.

The effective diffusion coefficient, or the apparent diffusion coefficient, is the diffusion coefficient of a given diffusant measured under specific conditions. When the motion of movement of the substance is diffusive, changes in the empirically measured effective diffusion coefficient therefore indicate changes in the diffusion conditions, for instance changes in temperature, changes in the viscosity or tortuosity of the substrate or a combination of these conditions. Changes in effective diffusion coefficient may also imply an introduction of advective factors to the system.

When measuring diffusion in the brain, an effective diffusion coefficient can my estimated with various empirical approaches. Significant changes in these measured D can be explained by changes in the mode of fluid movement due to functional changes of the brain physiology, for instance the proposed enhancement of glymphatic clearance during sleep.

1.6.3 Fluorescence recovery after photo-bleaching

Due to the physics of diffusion, it is very difficult to directly estimate the rate of diffusion at a precise accuracy, *i.e.*, to measure the diffusion coefficient in living tissues. It is more empirically challenging to do so in the small, delicate, and confined physiological environment of the brains of rodents. Measuring diffusion, is essentially measuring how quickly substances travel, assuming there is no convection. In previous attempts to identify ISF diffusion described above, tracers injected into the CSF or directly into the parenchyma were used and then the mapping of tracer movement was computationally analysed with pre-established diffusion models. Such attempts offer the capability to identify diffusion at some extent were able to differentiate diffusion from convection. Others used MRI to identify tracer movements in the brain, but again, due to the low regional resolution of the method, rate of tracer movements inside the tissue could not be accurately measured.

However, there is a traditional way to identify diffusion and calculate D: fluorescence recovery after photo-bleaching (FRAP). This method has been used under biophysical context to measure diffusion of molecule in biological materials. The basic principle of the FRAP method requires that a fluorescent tracer distributes evenly in a space, then a beam of strong light is used to bleach the fluorescence in a defined two-dimensional area; therefore, the fluorescence intensity in this bleached area reduces; following bleaching, unbleached dye from the surrounding area will influx to the bleached area by diffusion; the influx of unbleached dye leads to a recovery of fluorescence in this area; the rate of fluorescence recovery in the area is detected and recorded by a certain fluorescence detection method. When the concentration of the fluorescent tracer is proportional to the fluorescence intensity detected, the molar flux of the unbleached dye can be correlated in a function of time. In such way, an effective diffusion coefficient of the tracer molecule in this specific substrate is determined.

Two components are crucial to the successful application of the FRAP method: the fluorescent tracer (dye) and the detection method for fluorescent intensity. Firstly, the fluorescent tracer must be molecularly bleachable by intense light and must not recover its fluorescence chemically. This ensures that the fluorescence recovery recorded are solely from the influx of unbleached form of dye. The chemical properties of the dye must be inert, in another word do not react with any other molecules in the physiological environment. Secondly, the method to detect fluorescence must be quantitatively accurate so that the fluorescence level in the bleached volume can be reliably characterised in a function of time, referred to as the fluorescence recovery curve. Examples of methods which accurately measures fluorescent intensity include various forms of laser scanning microscopy (confocal or multi-photon) and photometry. Fluorescence microscopy can be used to take images of the bleached area and the fluorescence level can be determined from pixel intensities of the digitised images. The use of microscopy to quantify fluorescence works predominantly on tissue surface or within the shallow depth of the cortical surface of the brain. Alternatively, a photometry system can be used.

1.6.4 Photometry

Photometry is the measurement of light intensity, usually at specific wavelengths of light instead of measuring the total photonic radiation energy of the light (Bass *et al.*, 1995). When used in detecting fluorescence intensity in biological research, dichroic filters are usually applied. Dichroic mirrors are wavelength-selective, semi-transparent, band-pass light filters that filtrate specific wavelength bands of light. In such way, the light intensity at specific wavelength is selectively measured. This is particularly useful to measure fluorescence emitted by fluorescent tracers artificially introduced into physiological environments since the fluorophore molecules commonly used often have specific wavelength range for their excitation and emission.

Fluorescent proteins or pigments have functional groups in their chemical structure which react to light energy at specific wavelength, resulting in conformational change of its structure (excitation); then the energy may be released in the form of light radiation of another wavelength (emission). The photometry system utilises these chemical properties of the dye to excite the dye in a specific wavelength and record emission in another. Fluorescence intensity measured by the photometry system is usually in the form of radiant flux, in the unit of power, for example: Watts.

A Photometry system is consistent of several components: light sources, sets of dichroic mirrors, a pathway for light to be delivered and a photoreceiver that transduce light intensity into voltage. The photometry system can be designed to detect fluorescence in many forms, for examples solutions contained in cuvettes; whereas lights may also be presented to photometric detection via optical cables. The optical cable can be connected to fibre-optic cannulas embedded within live tissues. In such way, *in vivo* fluorescence levels can be measured and recorded by the photometry system which is referred to as a fibre-optic photometry system.

1.6.5 Examples of In *vivo* FRAP studies

In 2004, pioneer work by the A. S. Verkman group (Verkman, 2003; Binder *et al.,* 2004;) used FRAP method to measure the diffusion in extracellular space of the mouse cortex. Author opened a transparent intercranial window sealed to the cranium and filled the brain with a fluorescent tracer (FITC-dextran). A laser beam was used to bleach a small volume of the tracer in the brain

cortex and confocal microscopy was used to capture the fluorescence recovery. Relative diffusion speed was determined from the fluorescence recovery. Diffusion in the mouse cortex was found to be reduced under conditions affected by cytotoxic brain edema or brain seizure activities. This was the first time FRAP was used to determine solute movement speeds in the brain *in vivo*. The opening and resealing of the intracranial window lead to minimal invasiveness to the brain parenchyma itself. However, due to the limited penetrating capacity of the confocal microscope, diffusion measurements were limited to the cortical surface but not deep inside the brain parenchyma.

Later, Verkman and colleagues refined the FRAP method with a fibre-optic approach. An optical fibre was implanted inside the brain tissue and glass micropipettes were used to deliver the fluorescent tracer near the optical fibre. FRAP were carried out in tumour tissues and extracellular space of rodent brains (Thiagarajah *et al.*, 2006; Zador *et al.*, 2004). One limitation of traditional FRAP with fluorescent microscopy is that light only penetrates the tissue at shallow depths as brain parenchyma tissue creates significant scattering of the penetrating lights. Delivery of light by embedded optical fibre mitigates this issue. Based on FRAP data, Zador *et al*., (2006) reported that the movement of introduced macromolecule (FITC-dextran) in the extracellular space of the brain parenchyma is size-dependent; and the diffusion rates significantly increased in AQP-4 knock-out mutants. Another study by Sullivan *et al*. (2009) also used FRAP with microscopy to measure diffusion in tumour vessels and applied improved mathematical models to quantitatively estimate diffusion.

The FRAP experiment by Smith *et al.*, (2017) was discussed as an example contradictive to the glymphatic hypothesis (Section 1.5.2). Authors used two-photon microscope to capture fluorescence recovery on the cortical surface. In this two-dimensional modelling of fluorescence recovery, the potential directional flow due to advective influence was tested with an anisotropic method. Due to the miniature size of the bleached area, the authors were able to precisely target the perivascular space for FRAP recording and identified a much higher rate of flow in the perivascular space compared to the parenchymal tissue.

To summarise, FRAP method has been tested in various biological and physiological environment and proven to be a reliable method to detect mode of solute transport *in vivo.* However, previous studies utilised relative diffusion coefficient in contrast to diffusion coefficient in aqueous solution as a measurement of D, instead of deriving a D mathematically from the fluorescence recovery curve. Further *in vivo* experiments with FRAP method under different physiological conditions would be helpful if the glymphatic hypothesis is to be critically tested.

1.7 Glymphatic function with sleep and anaesthesia

1.7.1 Glymphatic function enhanced during sleep and anaesthesia

As described in Section 1.3.2, Xie *et al.* (2013) suggested a 95% increase of glymphatic influx when animal is supposed to be sleeping compared with manually awakened animals. Similar increase of glymphatic function was also observed with animals anesthetised with ketamine and xylazine (K/X) administration. In a separate study carried out by Hablitz (2019) and colleagues of the Nededrgaard's group, six different anaesthetic agents or agent combinations were administered in rodents to assess their impacts on the glymphatic function. The authors found that the glymphatic function measured by CSF influx was highest in K/X anesthetised animal followed by isoflurane (ISO) supplemented with dexmedetomidine (DEX) followed by pentobarbital; whereas animals anesthetised with α-chloralose, Avertin and ISO alone showed low CSF influx. DEX and xylazine function as anaesthetics due to its α_2 adrenergic agonistic properties (Gelegen *et al.*, 2014; Atalik *et al.*, 2000). Animals anaesthetised with α_2 adrenergic agonists exhibits low frequency delta wave in their EEG signatures similar to EEG during NREM sleep. On the other hand, ISO and pentobarbital are γ-aminobutyric acid type A ($GABA_A$) agonists which induce higher frequencies of EEG when administrated (Musizza *et al.*, 2007).

The similarities in EEG signatures and their proposed effects on glymphatic influx provide new way of dissecting the mechanism for brain clearance. More importantly, this may imply the beneficial effects of certain anaesthetic agents that stimulate sleep stages that help to enhance brain clearance. In order to confirm the glymphatic function as one of the purposes of sleep, more evidence is required.

1.7.2 Measuring sleep

In mammals, sleep is measured and quantified according to brain electrical activities. Signatures in these brain electrical oscillations characterise sleep into different stages. Brain electrical oscillations are measured by EEG. As described previously, brain EEG powers can be banded into different frequencies, and these frequency bands determine sleep stages, including REM sleep and NREM sleep. Combining with EMG measurements that monitor muscle movements, wakefulness is therefore differentiated from sleep. Therefore, the vigilance state of an organism can be classified into wake, NREM sleep and sleep.

EEG and EMG can be directly detected with electrodes placed adjacent to the brain cortex or the muscles. By analysing the EEG/EMG data recorded from these electrodes, it is possible to identify vigilance states in model organisms such as in mice. Similar approaches have been used in Xie *et al.* (2013) and Hablitz *et al.* (2019) studies where low frequency delta wave in the EEG indicating NREM-like sleep state which is reported to be associated with increased glymphatic function.

1.7.3 Circadian and zeitgeber time

In a recent study by Hablitz *et al.* (2020) from the Nedergarrd group, glymphatic function was reported to be not only affected by sleep but also by circadian control. This was found to be achieved by the circadian regulation of AQP-4 polarisation in the astrocytes. Circadian clock regulates many brain functions including sleep. Zeitgeber are external stimuli that entrain the circadian rhythms of an organism (Grandin *et al.*, 2006). Zeitgeber time is a unit of time describes the time scheme stimulus of a zeitgeber. By definition: the zeitgeber time zero is the start of the light period of a light: dark cycle (Conn, 2016). Under a light: dark cycle of 12: 12 hours, for animals that are nocturnal, for example mice, the time of activity starts at zeitgeber time 12 hours.

1.8 Rationale of the current study

The current study originated from the pursuit for the reasons for the inescapable necessity of sleep across all the mammals and birds. Ten years ago, the glymphatic hypothesis was proposed that sleep serves a purpose of metabolite clearance which could not be functioning during normal

brain activity. The glymphatic hypothesis proposed a convective pathway that actively sweeps metabolites including toxic waste molecules such as Aβ from the periarterial space towards the perivenous space for removal.

This hypothesis seems to be a possible explanation for sleep but some of its assumptions and concepts which contradict existing evidence are too hard to believe. One of the most debated concepts are the existence of bulk flow in the brain parenchyma. There are huge number of controversies over how ISF moves in the parenchyma. Supporter of the glymphatic system claimed they have observed almost doubled speed of ISF flow in the parenchyma when animal undergoes sleep or being sedated. However, the experiments they have carried out bear substantial drawbacks. At the meantime, no existing evidence has shown the flow of ISF in the parenchyma when the vigilance states of freely behaving animal are being simultaneously monitored.

Technically, previous establishment of FRAP method of measuring diffusion provided a novel approach to measure diffusivity of solutes in live animals. Adapting this technology with a fibre-optic photometry system would allow diffusion in the parenchyma of freely behaving mice to be measured. With a proper mathematical modelling of the FRAP data, diffusion coefficients in the brain parenchyma can be accurately estimated. Combining with the diffusion coefficients with real-time EEG/EMG recordings, ISF movement speed can be correlated with vigilance states.

Based on these rationales, the current study set the scope to identify the mode of fluid movement in the brain parenchyma during sleep and sedation. This will help to critically test the glymphatic hypothesis.

Aims and objectives of the current study

1. To design and construct a system and protocols to measure ISF flow rate in the brain parenchyma of freely behaving mice
2. To test the viability of the system and protocols
3. To compare the ISF flow rates in the brain parenchyma when mice are awake, sleeping and sedated

Chapter 2 Experimental Design

Having established the aims and objectives of the current study, series of mathematical theories, equipment set-ups and experimental approaches were developed. These include the 3D mathematical basis of the FRAP method, the equipment selection and construction of the fibre-optic photometry system, the protocol for photo-bleaching and recovery curve recording. Once the method has been established, it was initially validated *in vitro* with agarose gel where convective flow was prevented. Then, *in vivo* protocols were developed to assess the diffusion in the brain parenchyma when the vigilance states of the mice are monitored simultaneously. In this chapter, logics and reasonings of the experimental design, for the mathematical basis, the *in vitro* and *in vivo* experiments are explained and elaborated in detail.

In addition, the technical details and specifications of the materials, methods, and protocols used in the current study are attached to the end of this chapter.

2.1 Mathematical basis of the method

Professor Nicholas P. Franks helped to develop the mathematical basis of the method.

Fluorescence recovery after photo-bleaching (FRAP) has been traditionally used for estimating diffusion in tissues or other biological materials. Conventionally, this has been achieved in two dimensions where a circular region containing a bleachable dye is bleached and the diffusion coefficient were determined by calculating the rate in which unbleached dye from the surround area flows into the bleached area.

To adapt the well-established method using a fibre-optic photometry system in a three-dimensional environment, assumptions were made that following a bright illumination, the bleached fluorescent dye is distributed over a hemispherical volume which can be characterised by a Gaussian distribution. With an empirical method, this hemispherical Gaussian distribution has been visualised and confirmed, see result Section 3.3.2. Therefore, the concentration of bleached dye in this volume, $Q(s)$, can be expressed mathematically as:

$$\boldsymbol{Q(s) = Q(0) exp\left(-\frac{s^2}{2\sigma^2}\right) \quad (s \geq 0)}$$

Equation [1]

where $Q(0)$ is the maximum concentration of the bleached dye at the origin of the hemispherical distribution, *s* is the radial distance from the centre of the hemispherical distribution and σ is the standard deviation of the Gaussian distribution.

After the 30-second period of photo-bleaching, the bleached form of the FITC-dextran dye at the centre of the distribution starts to diffuse out while unbleached dye from the surrounding environment starts to diffuse in. The concentration of bleached dye, $C(r, t)$, as a function of time t, and the distance r from the centre of the hemisphere can be shown to be:

$$\boldsymbol{C(r,t) = C(0,0)\left\{\left[1 + \frac{2Dt}{\sigma^2}\right]^{-\frac{3}{2}}\left[exp\left(\frac{-r^2}{4Dt + 2\sigma^2}\right)\right]\right\}}$$

(Crank, 1979) **Equation [2]**

where D is the diffusion coefficient of the diffusing molecule.

When the concentration of FITC-dextran is proportional to the fluorescence intensity detected by the photometry system (see results Section 3.1.2 for confirmation), Equation [2] characterises the concentration of bleached FITC-dextran molecules at a certain distance r, and at certain time t after the photo-bleaching has occurred. Concentration of the bleached dye decreases as the bleached dye diffuses out to the surrounding tissue until an equilibrium is achieved. Under such scenario, the rate of concentration decrease is depended on the diffusion coefficient of the diffusing molecule, D. This whole derivation comes from a Gaussian distribution, and the -3/2 exponent is a consequence of the diffusion being three-dimensional.

With the help of the fibre-optic photometry system, the fluorescence intensity of FITC-dextran at the tip of the implanted optical fibre can be recorded immediately after the 30-second photo-bleaching period. Assuming the bleached area is small, and the surrounding area is infinite in volume and contains no bleached dye, after a time period long enough for equilibrium to be re-established, the bleached dye should completely diffuse out. At this infinite time point, the

volume at the tip of the optical fibre is cleared of bleach dye and therefore the fluorescence intensity should have recovered to the level prior to photobleaching. Figure 2-1 shows a schematic of the fluorescence intensity recorded by the photometry system before and after photo-bleaching. The fluorescence level prior to bleaching and after equilibrium has been re-established is denoted as $I(\infty)$; the fluorescence intensity immediately after photo-bleaching at its lowest point is denoted as $I(0)$; and the at a given time point t, the fluorescence intensity can be expressed as $I(t)$.

Therefore, at the time point t, the number of moles of bleached dye at tip of the optical fibre $M(t)$ can be related to the moles of bleached dye immediately after photo-bleaching $M(0)$ in the following expression:

$$\boldsymbol{M(t) = M(0)\left[\frac{I(\infty) - I(t)}{I(\infty) - I(0)}\right]}$$

Equation [3]

If we assume the fluorescence intensity is recorded in a hemispherical volume with a radius of R at the tip of the optical fibre, and $C(r,t)$ in Equation [2] describes the concentration of bleached dye at a distance (r) to the bleaching centre at time (t), $M(t)$ can therefore also be expressed as the integral of Equation [2] from $0 \rightarrow R$:

$$\boldsymbol{M(t) = \int_0^R 2\pi r^2\, C(r,t)\, dr.}$$

This leads to:

$$\boldsymbol{M(t) = \frac{2\pi C(0,0)\sigma^3}{\sqrt{(2Dt + \sigma^2)}}\left\{\sqrt{\frac{\pi(2Dt + \sigma^2)}{2}}\, erf\left(\frac{R}{\sqrt{(4Dt + 2\sigma^2)}}\right) - R\, exp\left[-\frac{R^2}{(4Dt + 2\sigma^2)}\right]\right\}.}$$

Equation [4]

Because $M(t)$ can be determined experimentally from Equation [3] with photometry, if R and σ are known, then, D can be derived from Equation [4]. Here it is considered that the volume which light penetrates into the brain tissue for photo-bleaching is comparable to the volume which light penetrates the brain tissue for fluorescence recording; therefore, it is reasonable to set $R = \sigma$. In fact, mathematically, according to Equation [4], the time course of $M(t)$ is highly sensitive to the value of D and σ. But it is insensitive to the value of R. So, this assumption has little impact on the derived value of D, which is the central focus of this study.

In terms of σ, the standard deviation of the Gaussian distribution in which bleached dye is distributed at the tip of the optical fibre is directly estimated by the distribution of light in a brain phantom gel. This was achieved by directly observing the light distribution at the fibre tip with a fluorescence microscope and fitting the captured light distribution with a Gaussian distribution (see Section 2.4).

From the mathematical derivation above, the mathematical basis of the method using FRAP with the help of a fibre-optic photometry system has been established. If σ is known, an effective diffusion coefficient, D, can be determined from the time course of $M(t)$ using Equation [4]. And the time course of $M(t)$, is essentially the fluorescence recovery curve followed by photo-bleaching and normalised to the fluorescence intensity prior to photo-bleaching. For each photo-bleaching and fluorescence recovery curve similar to the example shown in Figure 2-1, a diffusion coefficient can be calculated. In this way, D is estimated directly with the photometry recording.

To conclude, the mathematical basis of the method is established and used throughout the current study: when validating the method with fluorescence recovery curves in the brain phantom gel and when estimating diffusion coefficients *in vivo.*

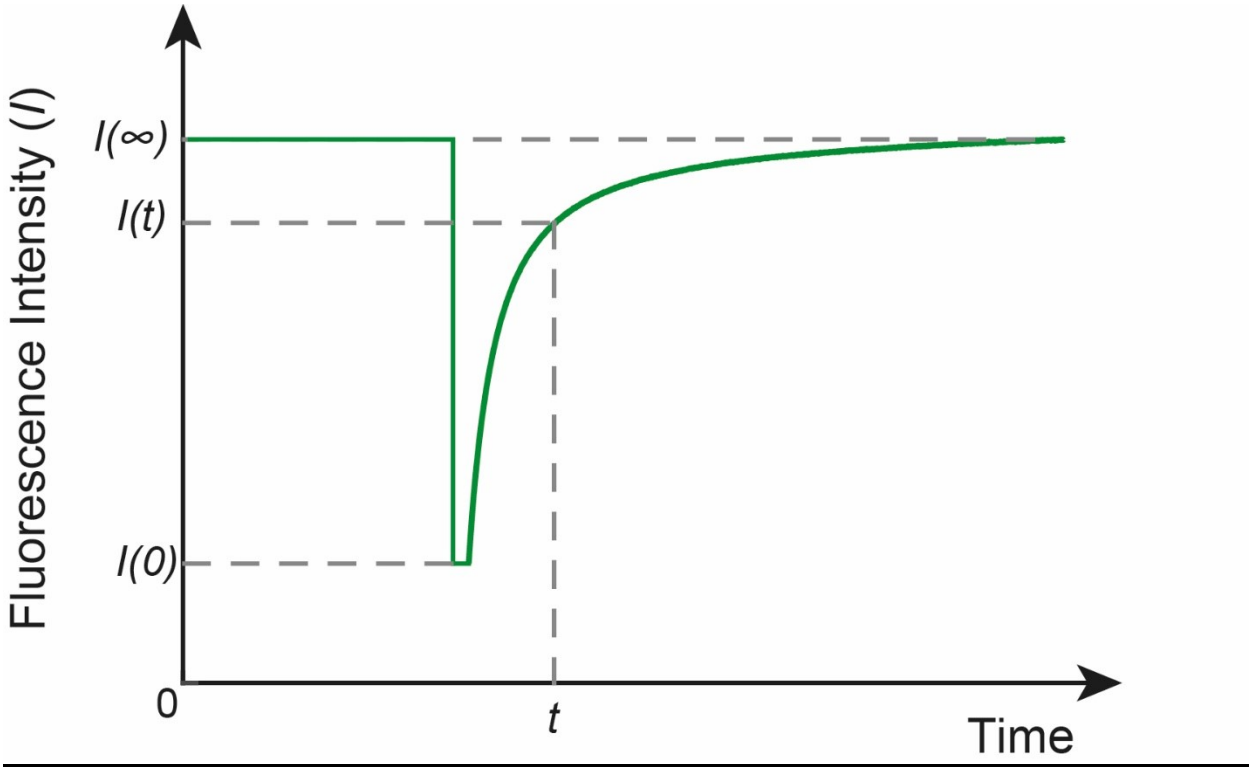

Figure 2-1 A schematic of the fluorescence intensity recorded by the photometry system prior and post photo-bleaching. Before bleaching, unbleached dye at the tip of the optical fibre stays in equilibrium with an intensity of *I (∞)*. Intensity decreases during the 30-seconds of photo-bleaching. Following photo-bleaching, fluorescence intensity starts to recovery from the total-bleached level, *I (0)*. At any given time, *t* on the fluorescence recovery curve, the fluorescence intensity is denoted by *I (t)*. Note that the fluorescence intensity during photo-bleaching is not recorded.

2.2 Using FITC-dextran as the fluorescent tracer

Fluorescein isothiocyanate-dextran (FITC-dextran) was used as the fluorescent tracer in this study. It is consist of the fluorophore molecules (fluorescein) and a branched saccharide (dextran) in a polymerised organisation. One base unit of the FITC-dextran polymer is shown in Figure 2-2. Many characteristics make FITC-dextran ideal for this study. Firstly, depending on the number of branches that dextran may have, one molecule of FITC-dextran can have different molecular weights. The molecular weights of FITC-dextran commonly used in molecular biology range from 4 kDa to 250 kDa. Secondly, due to the hydrophilic nature of FITC-dextran, it is highly soluble and stable when dissolved in polar solvents and does not permeate phospholipid bilayers therefore remains extracellular when introduced in live tissues. Thirdly, it induces very low neurotoxicity when introduced in the brain (Zhang and McClellan, 1999). Fourthly, unlike other tracers used in brain research such as IgG or Evans Blue, FITC-dextran is neither endogenous nor readily binding to endogenous molecules such as plasma proteins (Hawkins and Egleton, 2006; Wolman *et al.*, 1981). Due to these characteristics, FITC-dextran is commonly used as a long-term tracing agent in biophysical experiments investigating molecule diffusion and membrane permeabilities. Example of using FITC-dextran can be found in the studies of diffusion in extracellular matrix (Kihara *et al*., 2013), blood vessel permeability (Thomas *et al*., 2017), and cell permeability in the central nervous system (Heinzmann, 1980).

Fluorescein is a well-established fluorophore with an excitation peak around 490 nm and an emission peak 520 nm, which makes it an ideal fluorescent tracer detectable by the fibre-optic photometry system. It has been widely used as fluorescent tracer under many circumstances such as studying diffusion in microbial matrix (Silva *et al.* 2013), in cell culture (Arrio-Dupont *et al.*, 1996) and in live animal tissue (Hoogstraate *et al.*, 1994). Like most fluorophore, the ability of fluorescing of fluorescein can be permanently removed by photobleaching (Demchenko, 2020). This is achieved by supplying the molecule with sufficient photon intensity resulting in an oxygen-independent, proximity-induced triplet-triplet or triplet-ground state dye reaction (Song *et al.*, 1995). As a result of this, fluorescein was used in fluorescence recovery after photobleaching (FRAP) studies as early as in the 1980s (Tsuji and Ohnishi, 1986). However, instead of being used

in combination with a fibre-optic photometry system, fluorescent microscopy was traditionally utilised to quantitatively analyse fluorescence recovery. Examples of FITC-dextran used in FRAP are Braga *et al.* (2004) (in cell culture), Seksek *et al*. (1997) (in living animal tissue) and Waharte *et al.* (2010) (in synthesised biofilms). It has also been suggested that the fluorescence profile of fluorescein is pH-sensitive, with increased fluorescent intensity towards alkalinity up to pH 10 (Chen *et al.*, 2008).

To summarise, due to the cellular impermeability, variable molecular weights and photo-bleachable nature of FITC-dextran, it is ideal to be used as the fluorescent tracer in this study. Molecular weights of 4 kDa, 10 kDa and 70 kDa were used in different experiments throughout the study.

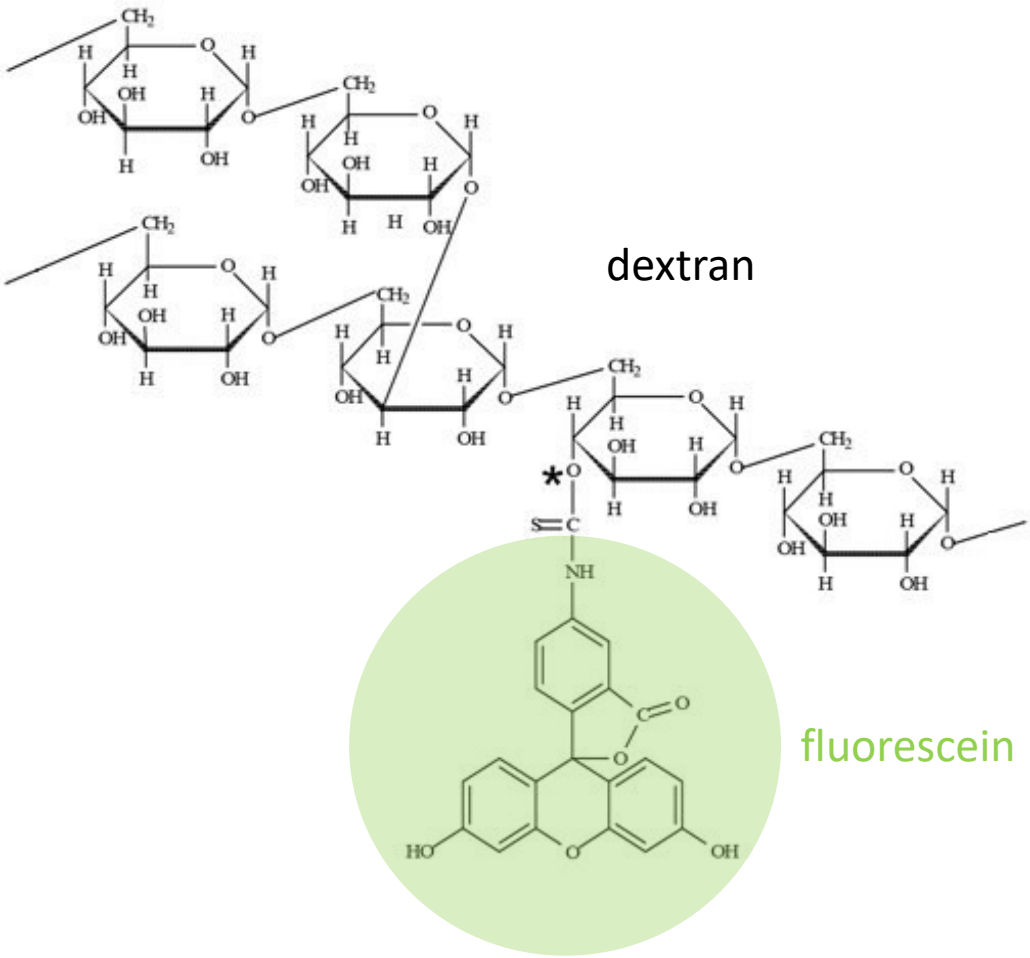

Figure 2-2 Base unit of the fluorescein Isothiocyanate-dextran (FITC-Dextran) molecule. FITC-dextran consists of a fluorescent pigment fluorescein conjugated with a long-chain polysaccharide. FITC-dextran can be made into different molecular sizes due to the level of polymerisation of the dextran sugar. This diagram was Modified from Merk, https://www.sigmaaldrich.com. (Merk, Darmstadt Germany)

2.3 Establishment of the fibre-optic photometry system

To estimate the effective diffusion coefficients from photo-bleaching and recovery, a photometry system that measures fluorescent intensity via an optical fibre is required. This system would allow real-time recording of FITC-dextran fluorescence from the implanted optical fibre in the mouse brain when the mouse is either free-moving or under sedation. The system would also be able to deliver a light powerful enough to bleach the FITC-dextran dye effectively but not too strong to change tissue properties. To achieve this, a new fibre-optic photometry system was designed and constructed specifically for this study. The equipment setup for the fibre-optic photometry system is shown in Figure 2-3.

The implanted optical fibre is connected with an optical cable with a rotary joint (Figure 2-3, Component L.). The rotatory joint prevents the optical cable from tangle during long-term recording when animal is freely moving. The light path then enters a customised mini-cube which contains a series of dichroic filters with four individual ports (K.). The SAMPLE port allows excitation lights to be delivered to the animal and emission lights coming out of the brain to be received. The OUT port is connected to a dichroic mirror which filters out the emission lights at the wavelength range of 500-540 nm, which was designed for fluorescein peak emission wavelength of 520 nm. There are two IN ports: 465-480 nm port allows excitation light from the 465 nm LED light source to path through and the 488 nm port allows lights from the 488 nm laser diode to be delivered to the implantation during photo-bleaching. The 30-second bleaching during each hour of recording is achieved by a programmable mechanical shutter (H.), which operates at a 30-second ON followed by a 3570-second OFF cycle during photometry recording. The 488 nm laser diode (F.) used for photo-bleaching is set at an output level resulting in a power of 1.3 mW measured at the tip of the optical fibre. This level of bleaching power suffices for the purpose of photo-bleaching but not enough to cause significant long-term heat accumulation or tissue damage at the tip of the optical fibre implantation (Stujenske *et al.*, 2015 Owen *et al.*, 2019). The 465 nm LED light source (G.) is configured to provide a power of 1.6 µW of light which excites FITC fluorescence for photometry recordings but not too intense to photo-bleach the dye. Fluorescence emission lights coming out of the OUT port is received by the photo-receiver (J.)

where light intensity is converted into analogue voltage signals and fed into the lock-in signal amplifier. The lock-in amplifier (C.) is required in the photometry setup for amplifying photometry signal from background fluorescence noise of the brain. The lock-in amplifier is set to generate a sine-wave carrier wave at a frequency of 120 Hz and an amplitude of 4 V, which is a common configuration for photometry systems with a lock-in amplifier. The generated carrier waveform governs the 465 nm LED light source via the LED driver (E.) to provide the excitation light for fluorescein in a pulsive manner. The emission light is also received by the lock-in amplifier where a demodulation function is performed to extract the photometry signal from the modulated carrier waveform received by the photo-receiver. The demodulated signal is received and converted into digital forms by the photometry controlling console (B.) and send to the PC for data recording. The software Doric Neuroscience Studio is used to configure hardware settings and to write and save the photometry data (A.).

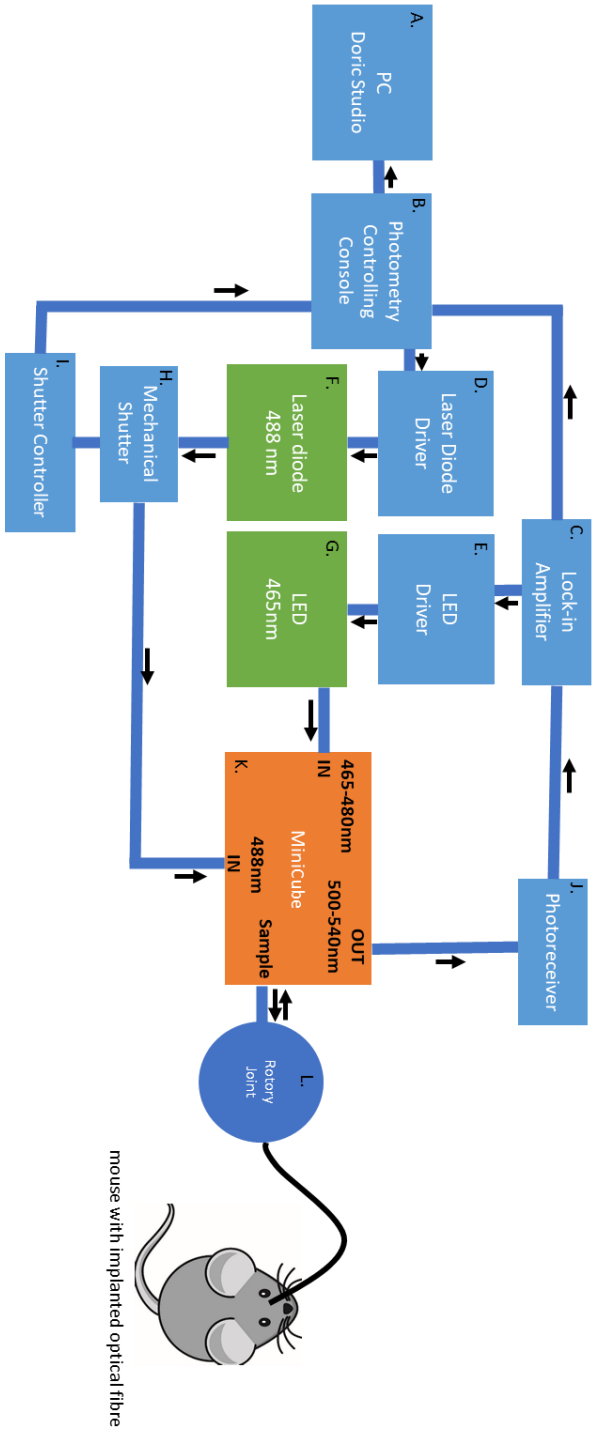

Figure 2-3 Photometry system setup for *in vivo* photo-bleaching and recovery experiments. Description of each component and their functions are detailed in Section 2.3. Specifications and technical details of the components can be found at the end of the chapter.

2.4 Profiling light distribution of the fibre-optic photometry system

In order to determine the standard deviation (σ) values used to calculate diffusion coefficients *in vitro*, an agarose gel was used. The agarose matrix of the gel creates a porous aqueous environment free from convective flow. The gel was also modified to approximate the light scattering and optical-absorption properties of real brain tissue. As described and tested by Zhang and Verkman (2010), milk solid and liquid Indian ink were added to the mixture when preparing the agarose gel with PBS, where milk solid creates scattering effects, and the ink mimics the light absorption properties of real brain tissue. This modified gel is referred to as the "brain phantom".

In order to estimate the likely geometric spread of photobleaching and calculate σ, a 200 µm optical fibre was inserted in a thin slice of the phantom brain gel containing FITC-dextran (Figure 2-4A). Then the light distribution from the optical fibre was directly visualised with fluorescence microscopy (Figure 2-4B). Due to the small thickness of the gel slice, the illuminated areas captured by microscopy were approximated to be two-dimensional.

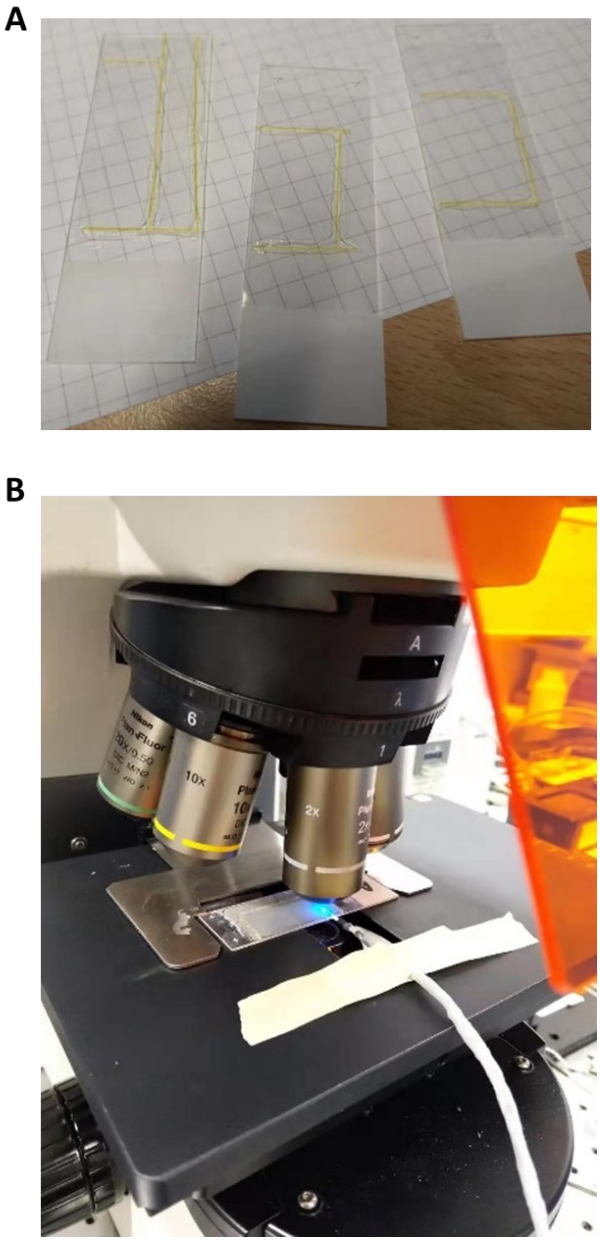

Figure 2-3 Setup for the direct visualisation of light distribution from the optical-fibre in brain phantom gels. A: Customised glass chambers made with 200-µm thick spacers. The cambers were filled with brain phantom agarose gel to make thin sheets of gel slice. **B**: a 200 µm diameter optical fibre was inserted in the brain phantom gel and placed under fluorescence microscope. The microscope is fitted with a dichroic mirror filter against an excitation wavelength at 465-495 nm and an emission wavelength at 515-555 nm. The optical fibre is connected to a 488 nm laser light source at a power of 1.6 µW.

However, it was soon realised that the abovementioned method provided an overestimation of the light distribution due to the internal reflection at the air-to-gel interface. This internal reflection can artificially increase the light distribution imaged, especially along the axial direction of the optical fibre. To overcome this issue, two clear agarose gel blocks (approximately 500-μm thick) were positioned on the bottom and top sides of the phantom brain gel slice (Figure 2-5). By providing a less dense substrate at the air-to-gel interface, the internally reflected light is diverged and not captured by imaging from the upright position. Any air bubbles between the gels were carefully removed before imaging.

The microscopy images were converted into 16-bit and then converted into an intensity matrix according to each pixel's location and its represented 16-bit intensity. This intensity matrix was fitted with a hemispherical gaussian distribution and the standard deviations of the gaussian distributions (σ) were successfully obtained.

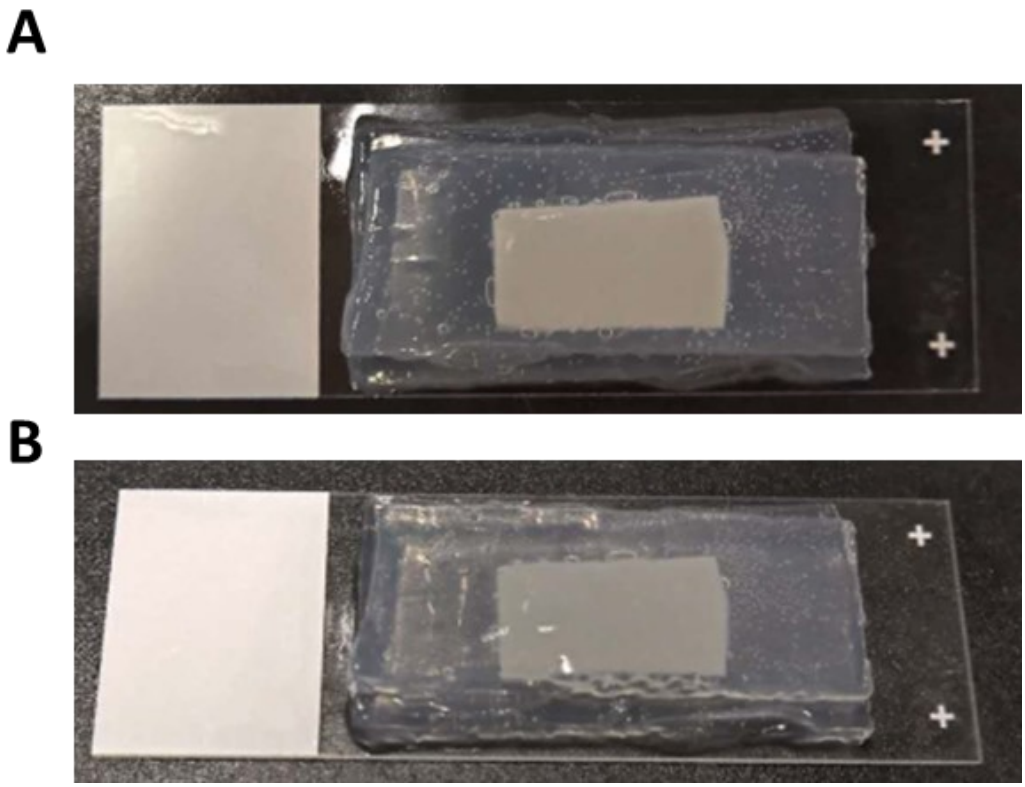

Figure 2-4 Setup to visualise light distribution from the optical fibre with a stack of gels. A thin sheet (800 μm) of brain phantom gel containing 1% agarose in PBS (w/v), 0.3 mg ml^{-1} FITC-dextran (M.W.: 4 kDa), 8% dried skimmed milk powder and 0.1% liquid Indian ink (v/v) was sandwiched by two 0.5% (w/v) agarose PBS gel blocks, placed on a glass microscopy slide. **A**: top view of the gel stack. **B**: Side view of the gel stack.

To determine the σ values for *in vivo* analysis, freshly sliced mouse brain section was used instead of brain phantom gel. Brain was sliced with a vibratome (Figure 2-6A) and kept in artificial cerebrospinal fluid (ACSF) supplied with carbogen gas in a manner similar to section preparation for patch clamping in electrophysiology (Figure 2-6B). Optical fibre was inserted into the brain slices and the light distribution from the optical fibre was captured under microscope (Figure 2-6C).

According to the mathematical basis of the method, the concentration of the bleached dye in the hemispherical volume at the tip of the optical fibre can be represented by the light distribution at the fibre tip. From the images obtained from the abovementioned method, images that profiling the light distribution in freshly sliced mouse frontal cortex were fitted with gaussian curves, based on Equation [1]. A hemispherical Gaussian curve is fitted along the axial axis of the fibre and a spherical Gaussian curve is fitted along the radial axis. Then a mean sigma is calculated from the two fittings.

When photo-bleaching and recovery were being carried out in the brain, bleached dye in the illuminated tissue would start to diffuse out during the 30-second of photo-bleaching period. This simultaneous diffusion would result in a smaller σ values compared to when directly observing light distribution, thus must be mathematically corrected. To correct the diffusion during the 30-second bleaching time, a Gaussian distribution of bleached dye was averaged from $t = 0$ to $t = 30\ s$ on Equation [1] and fitted with a Gaussian distribution for an averaged distribution. The σ corrected with the averaged distribution was used for fluorescence recovery curve fittings in gels and in the mouse brain.

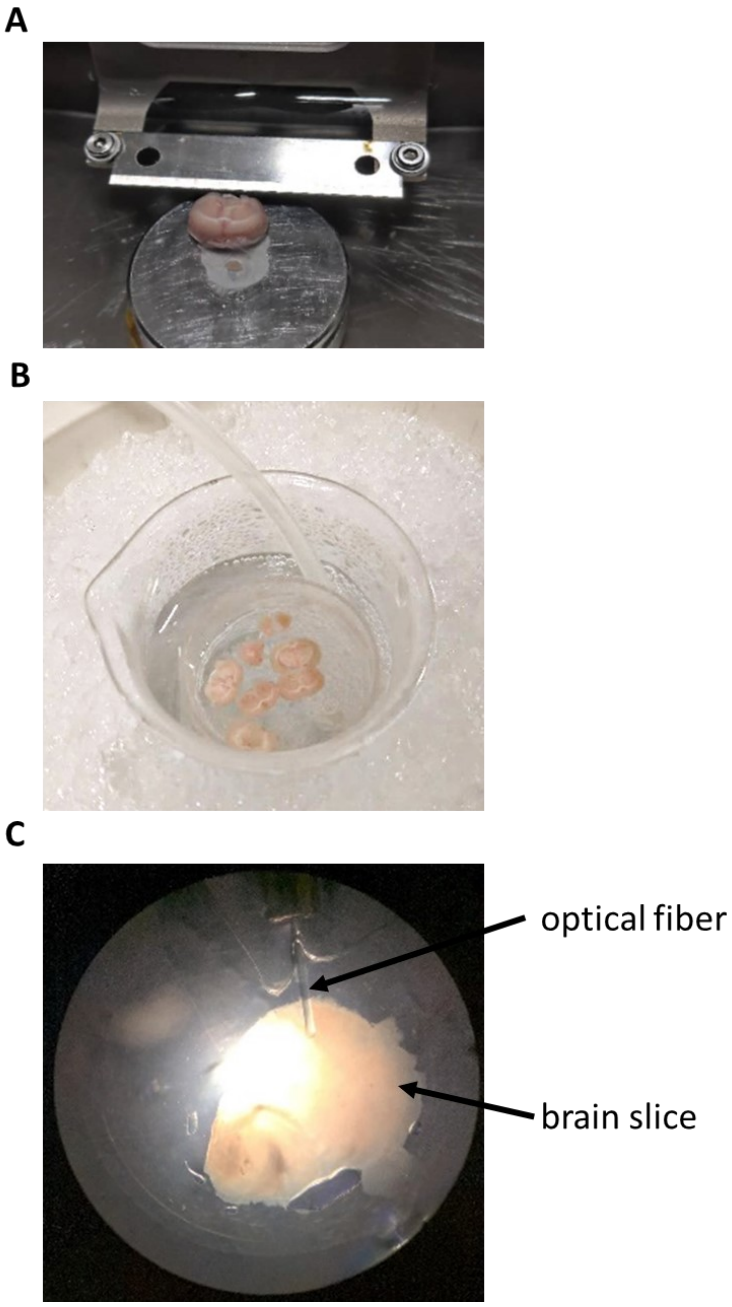

Figure 2-6 The visualisation of light distribution with freshly sectioned brain slices. A: Mouse brain was obtained immediately after sacrifice and placed in icy cold ASCF. Brain was sliced with a vibratome for 800 µm thickness at an advancing speed of 0.3 mm s^{-1}. **B**: Freshly sectioned brain sections were kept afloat in icy ACSF and supplied with carbogen gas. **C**: An optical fire was inserted in the frontal cortex of the brain slice and observed using a microscope.

2.5 Direct measurement of the diffusion coefficients of FITC-dextran

The diffusion coefficient of a given substance describes how fast the substance moves diffusively in a specific substrate environment when this environment is static, i.e., without the influence of a convective flow. Given the tracer molecules used in the current study are uncharged, therefore, when the diffusive conditions are met, the diffusion coefficient of a given substance depends on the size and shape of the diffusing molecule, the tortuosity and viscosity of the environment and temperature. Therefore, to measure the diffusion coefficients of FITC-dextran in aqueous solution requires a static environment free from convective flow and a technical method which accurately observes and records the velocity at which the FITC-dextran molecules travel. Assuming the fluorescence intensity detected from FITC-dextran is proportional to its concentration, the velocity in which the molecules move can be determined by the changes of fluorescence levels at certain distance after the molecules have diffused for a known time period. Based on this principle, several experimental approaches have been attempted to directly measure the diffusive velocity of FITC-dextran (4 kDa, 10 kDa, 70 kDa) in a non-convective environment.

Firstly, a static environment was achieved by creating an agarose gel, which contains 1% agarose in PBS (w/v). The porous environment of the gel can stop convective flow. Due to the extremely low percentage of the agarose content and highly porous and permissive nature of the 1% gel, it is approximated to be an aqueous environment. The whole system was also kept in a constant temperature of 20 °C.

The first attempt was trying to observe and record diffusion by sectioning a gel. A plastic clinical syringe was cut across its cross-section and filled with 1% agarose gel containing no FITC-dextran. The gel was immersed in a large volume of stirred PBS solution containing a known high concentration of FITC-dextran. The FITC-dextran in the surrounding environment was therefore allowed to diffuse into the gel in the syringe from only the cross-section. After a certain duration of time, the gel is pushed out carefully with a depth micrometre and sliced into 1 mm thick

sections. The diffused FITC-dextran within each section was extracted by adding known volume of PBS solution and allowing to reach equilibrium. The concentration of FITC-dextran in each section was then measured by a colorimeter. In this way, the concentration of FITC-dextran of a given distance to the diffusive interface after a given time can be measured. Assuming the concentration of FITC-dextran outside the gel stays constant, the velocity in which the molecules have moved can be estimated. Shantz and Lauffer (1962) has conducted a similar experiment to measure diffusion coefficient of molecules by slicing a gel pushed out of a cylindrical apparatus. However, due to the small volume of the gel, a clear cut of 1 mm could not be obtained consistently, and the first few sections which contains the highest concentration of the dye were often unevenly cut. This resulted in unacceptable errors in the first few sections and had greatly increased the overall error for the estimated D. This eventually led to failures in reproducing results for each molecular weights of the dye. This method design was therefore an unsuccessful attempt.

The second attempt utilised a similar system. Instead of using the colorimeter to measure the dye concentration in each 1 mm gel section, a fluorescence microscope was used to detect the concentration by calculating mean pixel intensity. A similar approach using fluorescence microscope is (Silva *et al.*, 2013). Again, the errors in sectioning as well as variability in image capturing heavily affected the reproducibility of the results, and no consistent D values yielded from this method. This method design was therefore an unsuccessful attempt.

To ensure an accurate measurement of the fluorescence level, the third attempt involved the using of the fibre-optic photometry system. The design principle was to allow FITC-dextran to diffuse through a gel. At a certain position of the gel, the optical fibre is inserted to measure the change of fluorescence at that position. Diffusion coefficients were then calculated from the time-coursed change of fluorescence intensity at that optical-fibre position.

Professor Nicholas P. Franks helped to develop the mathematical model to calculate D from this method.

A concentration of fluorescent molecule (FITC-dextran) is evenly distributed in a thin sheet of agarose gel of known thickness of L. When the surround environment contains no fluorescent

molecule, FITC-dextran will start to move out the gel by diffusion, given that agarose gel prevents convective movements. The efflux of the fluorescence of the molecule can be measured by the photometry system with the optical fibre placed within this thin sheet of gel. When the membrane is bounded with an impermeable barrier (a glass substrate) on one side of the membrane, the diffusing-out of the fluorescence molecule can only take place across one boundary of the sheet ($x = L$). The concentration of the fluorescence molecule at a distance to the crossing boundary (x), as a function of time (t), is given by:

$$\boldsymbol{C(x,t) = \frac{4\,C_0}{\pi}\sum_{n=0}^{\infty}\frac{(-1)^n}{2n+1}exp\left(-\frac{D(2n+1)^2\pi^2 t}{4L^2}\right)cos\frac{(2n+1)\pi x}{2L}}$$

(Crank, 1979) **Equation [5]**

Because of the cosine term related to in Equation 5, for x values of that are small compared to L (20% or less), the value of x has little effect on the time course of $C(x,t)$. As a result, when C can be measured very closely to the impermeable barrier ($x = 0$), D values can be accurately derived from Equation 5, provided that L is known. In this method, an optical fibre (200 µm in diameter) is bounded to the impermeable barrier, resulting in $x/L = 0.1$. Therefore, assumptions are met, and Equation 5 is valid to accurately estimate D of a diffusing fluorescence molecule directly.

Based on the mathematical theory, an experimental approach has been designed and constructed to measure D directly:

A thin sheet (1 mm thick) of brain phantom gel was made containing 25 mg ml^{-1} FITC-dextran of a molecular weight. The gel solidified and was sealed in glass substrates where only one side was exposed. Edges of the gel was further sealed with silica gel so the only site that the dye was enabled to diffuse out is on one side. A 200 µm diameter optical fibre was inserted at the bottom of the 1 mm gel sheet and fixed in position with super glue. A schematic of this setup is shown in Figure 2-7. The gel was then immersed in a stirred bath containing 0.1% Indian Ink and 8% milk solid in PBS. This was the same composition of the gel except having no agarose and the dye. This would ensure FITC-dextran within the gel to move out by diffusion and no other osmotic or concentration gradients to be interfered with the diffusion. The whole system was kept in a

constant temperature of 20 °C. The bath was kept at no less than 1000 times of the volume of the gel and constantly stirred vigorously. Therefore, the assumptions were met that the dye was allowed to freely diffuse out into a space that the concentration is approximated to be zero. The intensity of FITC-dextran fluorescence at the tip of the optical fibre was recorded with the photometry system over a period of time. Therefore, a D value can be calculated from Equation 5, knowing the fluorescence level at the position after a specific time period of diffusion. This method was able to produce consistent results and therefore was used to directly measure D of the three sizes of the dye.

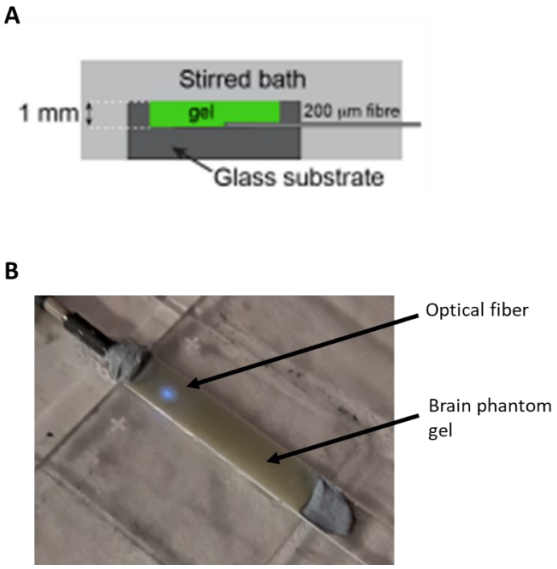

Figure 2-7 Direct measurement of the diffusion coefficient of FITC-dextran. A direct measurement of the diffusion coefficients of FITC-dextran has been developed. This method measures the fluorescence reduction when the dye is diffusing out of the gel into an infinite solution bath surrounding the gel brain phantom gel was contained in a glass chamber with only one side exposed to a stirred bath. The system is kept at a constant temperature of 20 °C. Details of the method is described in Experimental design Section and Material and Methods Section. **A**: A schematic of the glass chamber created to allow FITC-dextran to diffuse out in the indefinite stirred bath solution while fluorescence reduction close to the glass substrate is recorded via the fibre-optic photometry system. **B**: A photograph of the glass chamber connected with the optical fibre and filled with 1 mm-thick brain phantom gel. The gel shown here under preparation prior to be submerged into the bathing solution.

2.6 Validation of the method in brain phantom gels

When a photometry system designed to measure FRAP with fibre-optic implantation had been established, it was tested in the brain phantom gel to be validated. There are two main parts of the method to be tested: the experimental setup and the ability to estimate an accurate effective diffusion coefficient using the mathematical model.

An identical photometry system described previously was used. Instead of implanting the optical fibre inside the brain, the fibre was inserted into a brain phantom gel. Extra care was taken for a

perpendicular insertion of the fibre and avoiding any cracks resulting in gaps and cracks between the fibre and the gel. The gels were kept in plastic vials at a constant temperature of 20 °C and in a saturated humidity environment to avoid drying and shrinking of the gel throughout the course of the experiments. The brain phantom gel was prepared with 1% agarose gel in PBS with 0.3 mg ml^{-1} FITC-dextran.

Under constant temperature, the rate of diffusion of a molecule without convectional influence should be dependent on the molecular weight, assuming 1% agarose gel is an aqueous environment. Therefore, FITC-dextran of different molecular weights were used to validate the method: 4 kDa, 10 kDa and 70 kDa. When the optical fibre was connected to the fibre-optic photometry system, the same laser diode was used to bleach and the rest of the system including the 465 nm LED was used to record the fluorescence recovery. This helps to test the effectiveness of the bleaching and the capability of the setup to effectively measure fluorescence recovery after the photo-bleaching.

After the fluorescence recovery curves are recorded for each molecular weights, the diffusion coefficients for each molecular weights of FITC-dextran were calculated using the σ values obtained from the light distribution profile in the brain phantom. This allowed these calculated D to be compared with the diffusion coefficients calculated from an independent direct method of measurement for the three molecular weights of the dye (Section 3.4.2). If the D values calculated from the FRAP method remain in accordance with the D calculated from the independent direct method of measurement, the current method of measuring effective diffusion coefficients with FRAP using fibre-optic photometry is valid. The method therefore can effectively be used for the following *in vivo* environment when the fibre-optic photometry would be implanted in the frontal cortex of mice.

2.7 Test the method in controlled convections

If the previous experiments can confirm that effective diffusion coefficient can be accurately estimated by fitting the fluorescence recovery curves measured in the brain phantom; a controlled convective environment was established in order to test the method if convection can

be sensitively detected. This required FITC-dextran solution to flow at defined speeds while using the fibre-optic photometry system to bleach and record the fluorescence recovery curves. This was achieved by letting the FITC-dextran solution to be pushed by a syringe pusher through a sealed column containing Sepharose gel, a cross-linked, beaded-form of agarose gel (Figure 2-8). Usually, Sepharose gels are commercially available at different sizes and is used to immobilise peptides and proteins for purification. The Sepharose gel used in this experiment was cross-linked Sepharose CL-2B. CL-2B contains 2% beaded-form of agarose gel, and separate globular proteins from 70 kDa to 40000 kDa molecular weights. When linear liquid flow rate is below 28 $\mu m\ s^{-1}$, Sepharose gel 2B remains its structural integrity. The information above was acquired from GE Healthcare instruction:71-7097-00.

Molecular weights of FITC-dextran at 4 kDa, 10 kDa and 70 kDa were prepared in PBS solution at a concentration of 0.3 mg ml^{-1}, and pushed through the Sepharose column at convection speeds of 0, 0.5, 1, 2, 3, 4, 5, 10 or 20 $\mu m\ s^{-1}$. An optical fibre was inserted perpendicular to the direction of the flow on the wall of the syringe. The system was airtight with all air bubbles removed. The system was kept at a constant temperature of 20°C. The fibre-optic photometry system was connected to the optical fibre and the same photo-bleaching and recording protocol used in all *in vivo* experiments were applied. Three experimental repeats of the recordings were made for each molecular weight and each convective rate.

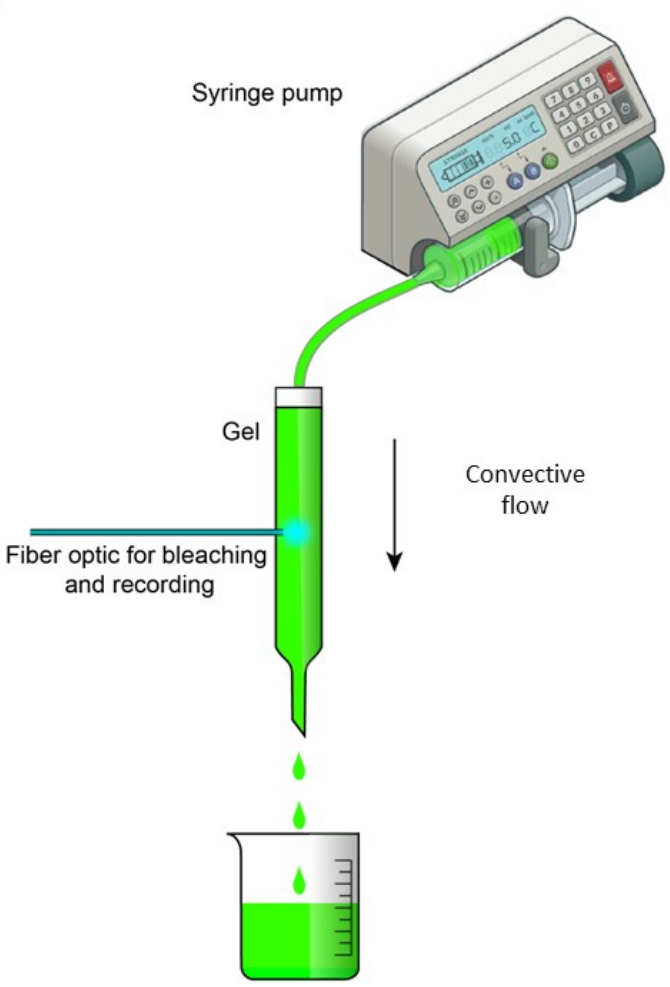

Figure 2-8 Recording photo-bleaching recovery curves in controlled convection. Controlled convection environments were established by pushing a FITC-dextran solution through a syringe pump into a protein separation column. The column contains non-reactive Sepharose gel (beaded agarose gel) to stabilise the convection flow. A 200 µm thick optical fibre identical to the animal implant was mounted perpendicular on the wall of the column and connected to the fibre-optic photometry system. Photo-bleaching was carried out and the fluorescence recovery curves were recorded for each FITC-dextran molecular weights under different convection speeds.

2.8 Applying FRAP in mouse brain parenchyma

After the FRAP method using the fibre-optic photometry system has been validated *in vitro*, *in vivo* experiments were carried out to apply this technique in the mouse to estimate diffusion coefficients in the brain parenchyma. For FRAP to work, the brain is to be filled with the fluorescent tracer which distributes evenly and remains relatively stable over a period of time. FITC-dextran is readily soluble in water-based solvent and remain stable in the body for days if not excreted (Thorball, 1981). Fluorescent tracer was to be delivered into the brain and allowed to be evenly distributed across the brain. Intracranial cannula is needed to be surgically implanted in the brain so intracranial injection of the fluorescent tracer can be carried out multiple times and at any time when the animal is conscious and active. At another brain region distal to the site of tracer injection, an optical fibre was surgically implanted to perform photo-bleaching and photometry recording.

The infusion of FITC-dextran through the cannula may be initiated randomly at different time of the day. Thus photo-bleaching and recovery were carried out throughout different time periods of the day. This allows the diffusion rate in brain parenchyma to be assessed across the zeitgeber clock, so any potential circadian influence on brain diffusion can be detected.

2.8.1 Dye injection and photometry recording in mice

After several surgical trials, the intracranial cannula was decided to be implanted in the caudate putamen of the left hemisphere with coordinates relative to the Bregma at M.L. -2.55 mm, A.P. -0.58 mm, D.V. -3.00 mm and the optical fibre to be implanted in the frontal cortex at M.L. -1.00 mm, A.P. 2.22 mm and D.V. -2.00 mm of the left hemisphere (Figure 2-9).

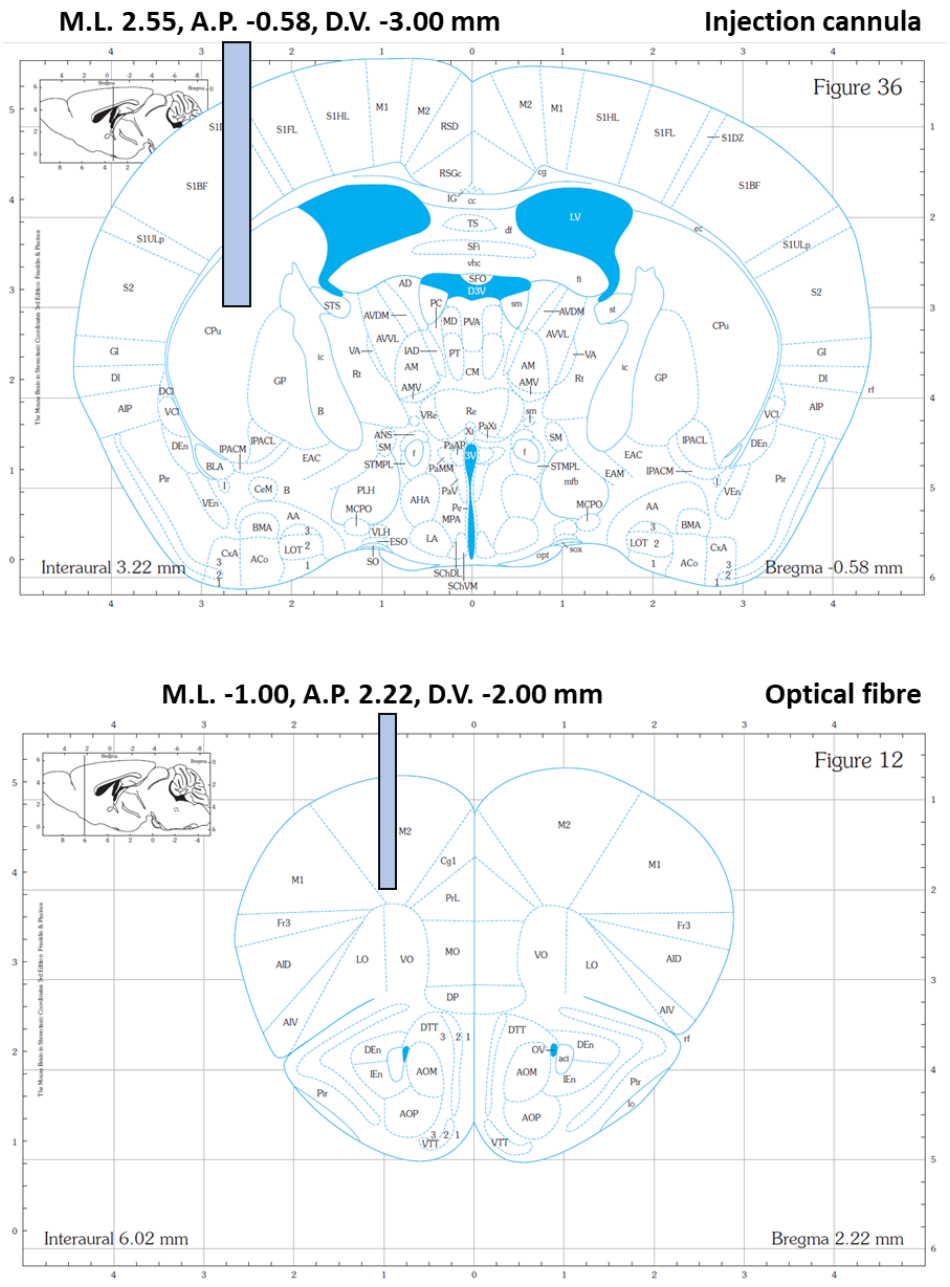

Figure 2-9 Histological locations of cannula and optical fibre implantations. Injection cannula and optical fibre have been implanted in the mouse brain. Cannula has been implanted in the caudate putamen of the left hemisphere at M.L. -2.55 mm, A.P. -0.58 mm, D.V. -3.00 mm. Optical fibre was implanted in the frontal cortex of the left hemisphere at M.L. -1.00 mm, A.P. 2.22 mm, D.V. -2.00 mm. All the cordinates are all relative to the Bregma.

Mouse caudate putamen is a robust brain region regulates the animal's motor actives by coordinating inputs from the cortex (Schröder and Huggenberger, 2020). It is an easily identified structure characterised by it striated structure and well supplied with blood by the distal medial striate artery and the lenticulostriate arteries (Augustine *et al.*, 2015). It is a robust structure which contains highly fibrous white matter of the internal capsule (Ara and Islam, 2010). Any intracranial implantation would inevitably cause damage to the local tissue where the implant is located. Mild damage to the caudate putamen in mice does not cause significant complication to the basic function of the brain and seems not directly affecting the control of sleep and wakefulness of the animal, although basal ganglia which the caudate putamen being a part of may have some level of motivational and behavioural influence on the changes of vigilance states (Lazarus *et al.*, 2013). In fact, animals in this study, when implanted with cannulas in the caudate putamen location were allowed to recover for at least one week before any experiments were carried out. After the recovery period, mice showed no behavioural abnormality compared with normal, non-implanted animals, and their sleeping patterns also showed as normal compared with animals of the same genetic background (data not shown).

The optical fibre in this study is implanted in the frontal cortex of the brain. Mice were allowed to heal for at least one week prior to experiment in order to minimise the influence of local tissue damage. Mouse frontal cortex is involved in complex executive functions which can be cognitive and organised behavioural responses to sensory information (Merre *et al.*, 2021). It is a highly plastic brain region involved in no critical functions of the brain and is not directly involved in the neuronal circuitry of vigilance state regulation. On the other hand, brain frontal cortex contains highly active neurones which produces higher level of metabolic wastes. Accumulation of β-amyloid (Aβ) peptides in the frontal cortex and prefrontal cortex has been studied intensively in elderly human and other model organisms and has been suggested to play important roles in the impairment of cognitive ability during the development of Alzheimer's disease and dementia (Jack *et al.*, 2008; Mori *et al.*, 2014; Zhuo *et al.*, 2008; Lo *et al.*, 2013). Therefore, determining the local CSF movement speed in the parenchyma of the frontal cortex opens new research perspectives for future understanding on the development of dementia and Alzheimer's disease.

Besides ensuring the survivability and health condition of the animal post-surgery, the most determining reason for locating the cannula and optical fibre positions was the constrains due to the relatively large physical sizes of the cannula and optical fibre thus the large room they occupy that was required on top of the skull. The injection cannula and optical fibre both have a bulky external part allowing them to be fixed in position on the top of the skull by super glue and dental cement.

All animals were allowed at least one week of healing and recovery before any experiment was carried out. FITC-dextran 4 kDa solution was prepared in sterilised 0.85% saline solution at a concentration of 25 mg ml^{-1}. During experiment, animals were infused with FITC-dextran solution at a rate of 0.1 µl min^{-1} via the cannula by a syringe pusher for a total of 100 min to inject 10 µl of dye solution. This infusion speed is a typical speed for intracranial injection in mouse, ensuring a minimal impact on the local tissue and the intercranial pressure. After a delay of 20 min, the injection tubing was replaced by the dummy cap. Then the implanted optical fibre was connected to the photometry system and photo-bleaching and recovery recordings begin. The animal was kept in his own home cage with lid open to allow access of the optical cable and water/food was provided as normal. All experiments were carried out under normal lights-ON and lights-OFF cycle as the same with the animal's normal zeitgeber scheme.

The same protocol of photo-bleaching and recovery used in the gel was applied to the animal. The photometry system provides bleaching intensity for 30 seconds for every one hour for the total duration of more than 24 hours. Photometry recordings for the fluorescent recovery curves were carried out between each bleaching. Although fluorescence recovery curves were recorded for the full duration of the experiment period, data was only used for analysis when the baseline fluorescence intensity has reached its peak and slowly declining, typically after 5 hours to 6 hours after the beginning of the infusion.

2.8.2 Using mice and the animal model

All the mice in this study were wild type C57/BL6J male mice aged between 3-7 months old. Wild type was chosen as the model organism for the current study for its close resemblance of its healthy neurophysiology as a closer representation of the normal physiology of fluid flow in the

brain. These mice also have a normal sleep-wake cycle free from known disruption of their circadian cycle. Female mice were not used to avoid hormonal and other effects resulted from menstrual cycle, although in future works, brain clearance in female mice can also be investigated separately. Only adult mice were used in this study, since it has been argued that aging can have a profound impact on the glymphatic system (Li *et al.*, 2022; Fyfe, 2020; Benveniste *et al.*,2019). The impact of aging on fluid flow in the brain parenchyma can be investigated in a separate study.

2.8.3 Electroencephalograph and electromyograph recording

For assessing the vigilance states of the animal, electroencephalograph (EEG) and Electromyograph (EMG) was recorded for the mice during the whole duration of photometry recordings. This was achieved by implanting conductive screw as electrodes on top of the brain cortex and conductive wires underneath the neck muscles. Miniature tether-less data logger (the Neurologger) were used to connect with these electrodes and wires and attached to the skull for EEG and EMG recordings. The Neurologger was developed by Bryan Hsieh who was another PhD student of our group. A detailed description of this device was previously published at Hsieh *et al.*, 2019. To summarise, two 2 mm long electrode screws were implanted for each mouse on its skull at the coordinates of (M.L. +1.5, A.P. +1.5 mm) and (M.L. +1.5, A.P. -1.5 mm) relative to the Bregma. The screws are on contact with the top of the cortex and detects electric voltage generated by brain activities. The former screw was the recording electrode, and the latter was the reference electrode. The EMG wires were inserted between the neck musculatures. EEG and EMG data were recorded at a frequency of 200 Hz.

To prepare the EEG and EMG data for the identification of vigilance states, the EEG signal was then high-pass filtered (0.5 Hz, -3dB) using a digital filter and the EMG signal was band-pass filtered between 1-50 Hz (-3dB). Power in the delta (1-4 Hz), theta (5-10 Hz) power bands and theta to delta band ratio were calculated, along with the root mean square (RMS) value of the EMG signal (averaged over a bin size of 5 s). All of these processed EEG and EMG data were then analysed by a customise analytical script for the identification of vigilance states (see the next section).

2.8.4 A custom script for data analysis

Bryan Hsieh helped and together with me developed this custom analytical script.

The central aim of the current study is to estimate the speed of flow in the brain parenchyma during different vigilance states of the mouse. As described above, a FRAP method can be developed to estimate effective diffusion coefficients from fluorescence recovery curves after photo-bleaching, at the same time vigilance state of the mouse is monitored and recorded by the Neurologger connected to the electrodes surgically attached onto the cortex of the mouse brain.

One diffusion coefficient is derived from each fluorescence recovery curve recorded by the photometry machine using Equation [3] and Equation [4] (Section 2.1) with an empirically determined sigma value (Section 2.4). Bryan helped to develop a probability-based algorithm that uses Gaussian Mixture Model and z-score normalization for unsupervised scoring of sleep vigilance states. The core method used in this sleep scoring algorithm was obtained from Libourel *et al.* (2015). These two analytical components were combined into one MATLAB script that automatically reads photometry recording data and EEG/EMG data obtained from the Neurologger and matches each recovery curve with the duration of mouse vigilance state. A copy of this MATLAB script can be found in the Appendix.

Examples of photometry and EEG/EMG data and a demonstration of how this customise script works can be found in the result Section 4-3.

2.8.5 Sedation with dexmedetomidine

As mentioned in the Introduction, certain sedatives, the α2 adrenergic agonist such as xylazine and dexmedetomidine can induce a brain state resembling deep NREM sleep in mice (Akeju *et al.*, 2018; Scheinin *et al.*, 2018 and Gelegen *et al.*, 2014). It has also been suggested the brain clearing effects of the glymphatic system is greatly enhanced due to increased convection existing in the parenchyma (Xie *et al.*, 2013; Lilus *et al.*, 2019).

Some mice in this study were given dexmedetomidine by intraperitoneal injection 6 hours after the start of FITC-dextran infusion at the time when the fluorescence baseline enters the steady decrease phase. Several dose-response trials were carried out to determine a suitable dosage of

dexmedetomidine for injection. It was found that a dose of 200 μg kg^{-1} was able to keep the animal in sedation for 4-6 hours where at least 3 bleach-recovery curve was recorded. The level of sedation was assessed behaviourally where a mouse is considered to be under the sedative effects of the drug when it loses the loss of righting reflex and is unable to keep the head up and stand on its feet. Apart from reduced locomotor activity, dexmedetomidine is also known to induce reduction in heart rate, respiratory rate and core body temperature in mice (Sallinen *et al.*, 1997 & 2003). To control the effect of hypothermia on diffusion, sedated mouse was placed on a heat pad with a thermostat regulating its core body temperature to 36.5 °C.

2.9 Conclusion

In this chapter, the mathematical basis for a 3D FRAP method was introduced. It calculates diffusion coefficient from the fluorescence recovery curves measured by the photometry system. A fibre-optic photometry system was designed and constructed specifically for the photo-bleaching and recovery curve recoding of FITC-dextran, a fluorescent tracer to be injected into the brain. A series of *in vitro* experiments utilising the physical model of the "brain phantom" were established for estimating sigma values used for fitting the fluorescence recovery curves. Then, *in vivo* photo-bleaching and photometry recording protocols were successfully developed, where an injection cannula and an optical fibre are to be implanted into the mouse brain of chosen brain regions. Meanwhile, the Neurologger device were used to record EEG/EMG data simultaneously with photometry recordings. A sedative drug Dexmedetomidine was selected to mimic a sleeping state of the brain. A customise analytical script was developed for automated data analysis. In such way, the brain diffusion can be assessed between different vigilance states, and during sedation. Potential changes in brain diffusion related to the circadian cycle of the animal can also be tested.

2.10 Materials and Methods

The technical details and specifications of the materials, methods, and protocols used in the current study are listed below.

2.10.1 Spectrometry

Absorption spectra measured for the tracer used in the study were carried out with a scanning spectrometer (Varian Cary 50 Probe, Agilent Technologies, CA, USA). Scanning rate was set at 60 nm/min with 0.5 nm data intervals. All samples were loaded on UV quartz cuvettes (Z276723, Sigma-Aldrich, MO, USA) with a path length of 10 mm. All measurement were made at a temperature of 20 °C.

2.10.2 Complete bleaching of the fluorescent tracers

A xenon light source (ARC lamp Oriel Instruments, CT, USA) was used to photo-bleach the FITC-dextran solutions contained by a cuvette constantly stirred with a magnetic stirrer. Temperature of solutions under photobleaching was between 20 and 40 °C.

2.10.3 Thin layer chromatography

Chromatography tests were performed with a solvent consistent of hexane and ethylene acetate at 1:3 ratio. Samples were dissolved in 0.85% saline (Oxoid, Thermo Fisher Scientific, MA, USA) at respected concentrations. A thin sheet of silica gel was loaded with 2 µl of each sample. Mobilisation was stopped when samples were completely separated.

2.10.4 “Brain phantom” agarose gel

“Brain phantom” agarose gel was made to approximate the optical scattering and absorptive properties of real brain tissue (Zhang and Verkman, 2010). 1% (w/v) agarose gel (A9539, Sigma-Aldrich, MO, USA) was dissolved in PBS (P4417, Sigma-Aldrich, MO, USA) at boiling temperature and allowed to be cooled down to a temperature approximately 50˚C. Only when the temperature was cooled below 50˚C, the rest of the ingredients were added. This was to prevent the denaturation of protein and dye in the final mixture. While maintaining at 50˚C with a heat source, 8% dried skimmed milk powder (70166, Sigma-Aldrich, MO, USA) and 0.3 mg ml^{-1} FITC-Dextran at different molecular rates (4 kDa, 10 kDa 70 kDa: 46944, FD10S and 46945, Sigma-Aldrich, MO, USA) were mixed separately with the gel.

2.10.5 Establishment of the fibre-optic photometry system

Components of the photometry system from Doric Lenses (Quebec, Canada) include the followings: rotary joint (FRJ_1x1_PT_200-0.37_1m_FCM_0.15m_FCM), 488 nm laser diode with laser driver (CLDM_488/050, LDMD), 465 nm LED with LED driver (CLED_465, LEDD), fibre photometry console (FPC), Doric Neuroscience Studio software (version 5.4.1.23) and all optical cables connecting the components except the cable connecting the mini cube and the photoreceiver were mono fibre-optic patch cords with an glass internal core of 200 µm (diameter), polymer cladding and a numerical aperture of 0.48. The optical cable connecting the mini cube and the photoreceiver was an attenuating mono fibre-optic patch cord with an optical transmission of 10 per cent.

Photoreceiver used in the system was a femtowatt photoreceiver, sensitive for wavelength 320-1050 nm (#2151 New Focus, CA, USA). The lock-in amplifier was #SR830 DSP 102 kHz from Stanford Research Systems (CA, USA) and the mechanical shutter with its programable controller was from Stanford Research Systems #SR470 (CA, USA).

2.10.6 Profiling light distribution in gel and in brain sections

A slice of brain phantom agarose gel (800 µm) containing 0.3 mg ml^{-1} FITC-dextran (molecular weight 4 kDa (46944 Sigma-Aldrich, MO, USA) was prepared with the method mentioned above. The same optical fibre (diameter: 200 µm) used in the photometry system was inserted in the middle of the gel slice. The slices were sandwiched by two blocks of 0.5% (w/v) agarose gel (A9539 Sigma-Aldrich, MO, USA) dissolved in PBS (P4417, Sigma-Aldrich, MO, USA) with all bubbles removed. A laser light source at 488 nm (CLDM_488/050 Doric Lenses, Quebec, Canada) was connected to the optical fibre with an optical cable (core diameter: 200 µm). The light output was measure at 488 nm at a power of 1.6 µW by a fibre optic power meter (PM20A, Thorlabs, Ely, UK.). The light distribution from the optical fibre was observed by a fluorescence microscope (Eclipse 80i, Nikon Instruments, NY, USA) illuminated by a mercury lamp (USH-102D, Ushio Europe, Oude Meer, Netherlands) with a dichroic light filter cube (excitation wavelength: 465-495 nm; emission wavelength: 515-555 nm) (Nikon Instruments, NY, USA). A camera (RTV-5.0 CCD, Qimaging, Surrey, Canada) connected to the microscope was used to capture the light

illumination at an exposure time of 80 ms. This short exposure time ensures minimal photo-bleaching during imaging.

For the profiling of light distribution in real brain sections, male C57/BL6J mice at a similar age (3-7 months) to the mice used in *in vivo* experiments was euthanised by neck dislocation, and had their brains taken out by dissection immediately after euthanise. Brains were kept on ice and sliced at 800 µm thick with a vibratome (7000smz-2, Campden Instruments, Loughborough, UK). Sections were then kept afloat in icy cold artificial cerebrospinal fluid, Cold Spring Harbor Protocols: 119 mM NaCl (S9888, Sigma-Aldrich, MO, USA), 26.2 mM $NaHCO_3$ (S5761, Sigma-Aldrich, MO, USA), 2.5 mM KCl (58221 Sigma-Aldrich, MO, USA), 1 mM NaH_2PO_4 (S3139, Sigma-Aldrich, MO, USA), 1.3 mM $MgCl_2$ (M1028, Sigma-Aldrich, MO, USA), 10 mM glucose (NIST917C, Sigma-Aldrich, MO, USA), filter sterilised with a 0.22-µm filter (GSWP04700, MilliporeSigma, MA, USA) and supplied with 95% oxygen and 5% carbon dioxide gas (Carbogen gas, BOC, Woking, UK) prior to imaging. Optical fibre was then inserted in the middle of the section manually and the section was sandwiched by clear gel blocks in the same manner as the phantom brain gel sections and imaged under the same condition as described above.

2.10.7 Direct measurements of diffusion coefficients

A glass chamber was constructed to hold a thin layer of brain phantom gel of 1 mm thick. Only one side of the gel was exposed, the rest of the gel was sealed to the glass with silicon grease (85410-1EA, Sigma-Aldrich, MO, USA). The gel individually contains FITC-dextran of different molecular weights (4 kDa, 10 kDa and 70 kDa) at a concentration of 0.3 mg ml^{-1}. The gels were immersed in glass beaker containing a bathing solution constantly stirred with a magnetic stirrer. The system was kept at 20°C constantly. The bathing solution was a PBS solution added with 8% (w/v) milk solid and 0.1% (v/v) Indian Ink identical to the brain phantom excepting not containing agarose and the FITC-dextran dye. The bathing solution has a volume greater than 1000 ml and is covered with cling film to avoid water evaporation during recording.

2.10.8 Measuring diffusion coefficients in the gel

Brain phantom gels were loaded in 24-well plates. The gels individually contain FITC-dextran of different molecular weights (4 kDa, 10 kDa and 70 kDa). A 200 µm optical fibre identical to the animal implantation was inserted perpendicularly into the centre of gel and held in position with a metal clamp. The optical fibre was then connected to the same fibre-optic system which would be used for in *vivo* experiments. The system was kept at constant temperature of 20°C. The system was kept in a saturated humidity to prevent the drying of the gel which would lead to shrinking and cracking of the gel.

2.10.9 Test the method in controlled convections

A plastic protein separation column was mounted vertically with a whole drilled on one side. A 200 µm (diameter) optical fibre identical to the *in vivo* implantation was mounted perpendicularly through the plastic wall of the column and sealed with super glue and dental cement for an air-tight fit. The optical fibre was connected to the photometry system for photo-bleaching and fluorescent recovery curve recording. The top of the column was seal connected to a syringe pump (Syringe Infusion Pump 22, Harvard Apparatus, MA, USA) via silicon tubing (20 cm in length, 4/6 mm I/O diameters) (RS Components, Northants, UK). The bottom of the column was left open and flowing out liquid was collected with a glass beaker. The column was filled with Sepharose gel CL-2B (CL-2B, Sigma-Aldrich, MO, USA). The column was pre-washed with PBS and then left for stabilisation and equilibration for at least 20 minutes. Prior to recording, the column was flushed with the corresponding FITC-dextran PBS solution (0.3 mg ml^{-1}) for 10 minutes and left still for another 20 minutes to allow stabilisation and equilibration.

The column has an internal diameter of 7.5 mm, which can be converted to a linear flow rate of 1 µm s^{-1} per 6.75 µl min^{-1} volume flow rate. The syringe (BS-50C, Terumo Europe) used to push the liquid through the column had an internal diameter of 29.1 mm. Therefore, the syringe pump was calibrated to the syringe and set at liquid flow speeds of 0, 5.3, 10.6, 21.2, 31.8, 42.4, 53, 106, and 212 µL min^{-1} to achieve 0, 0.5, 1, 2, 3, 4, 5, 10 or 20 µm s^{-1} linear convective speed at the optical fibre tip.

2.10.10 Animal model and ethics

All animals used for *in vivo* experiments of this study were C57/BL6J mice, purchased from Charles River Research Models (Margate, UK). Mice were all male aged from 3 to 7 months old. Mice were maintained on a 12 hr: 12 hr, light: dark cycle at a constant temperature (23 °C) and humidity (RH 50%) with *ad libitum* food and water.

All experiments were performed in accordance with the UK Home Office Animal Procedures Act (1986) and all procedures were approved by the Imperial College Ethical Review Committee.

2.10.11 Stereotactic surgery and intracranial implantation

All mice have their hair on the skull shaved prior to surgeries. Analgesic drugs buprenorphine (Vetergesic Multidose, Ceva Animal Health, Amersham, UK) and carprofen (Rimadyl, Zoetis Animal Health, NJ, USA) were inject subcutaneously at dosages of 0.1 mg kg^{-1} and 5 mg kg^{-1}, respectively. Drugs were diluted with 0.85% saline (Oxoid, Thermo Fisher Scientific, MA, USA) to allow an extra of approximately 350 µl of saline to be injected together with the analgesics subcutaneously to avoid dehydration of the animal during the course of the surgery. Each surgery lasted approximately 1.5 hours on average. Then, mice were anesthetised with 2% isoflurane (Piramal Critical Care, Longford, UK) in oxygen (Nuvo Lite Mk 5, Gas Control Equipment Group, Malmö, Sweden) and have their head fixed on a stereotactic surgery frame (Angle Two, Leica Microsystems, Milton Keynes, UK) with two ear bars (51648, Stoelting, IL, USA) next to both of the tympanic membranes without rupturing the memberanes. Mice were kept on a homeothermic blanket connected to a thermostat (69020, RWD, Shenzhen, China) to maintain the body temperature at 36.5 °C.

A 24G guide cannula (GC24-28, World Precision Instruments, Hertfordshire, UK) which is 2.8 mm in length was inserted into the skull at M.L. -2.55 mm, A.P. -0.58 mm (relative to Bregma) in the left hemisphere. A mono fibreoptic cannula (the optical fibre) which is 200 µm in diameter and 2 mm in length (Doric Lenses, MFC_200/230-0.48_2mm_ZF1.25(G)_FLT) was inserted into the skull at M.L. -1.0 mm, A.P. +2.22 mm (relative to Bregma) in the left hemisphere. A 26G dummy cannula with a length of 3 mm (DUMC 26-30, World Precision Instruments, Hertfordshire, UK)

was screwed into the guide cannula to seal the cannula when an intracranial injection is not performed.

Two miniature metal screws (00-96 x 1/16, Plastic One, VA, USA) were used as EEG electrodes and fixed on the brain cortex through the skull at: A.P. +1.5 mm, M.L. 1.5 mm and A.P. -1.5 mm, M.L. 1.5 mm, both relative to Bregma. Two EMG wires (AS634, Cooner Wire, CA, USA) were inserted between the neck musculatures. A multipin plug was solder connected to the two EEG screws (via wires) and EMG wires. This multipin plug together with the cannula and optical fibre were then permanently fixed to the skull with cyanoacrylate super glue (853188, Henkel, NE, USA) and then strengthened with orthodontic resin powder and Orthodontic resin liquid (TOC Dental, Bristol, UK).

Mice were given Carprofen Rimadyl, Zoetis Animal Health, NJ, USA) in drinking water (concentration: 32.5 mg L^{-1}) continuously for three days post-surgery. Mice were allowed to rest and recover for at least one week before any experiment was performed.

2.10.12 Intracranial injection with an implanted cannula

FITC-dextran 4 kDa (68059, Sigma-Aldrich, MO, USA) were dissolved in 0.85% sterilised saline (Oxoid, Thermo Fisher Scientific, MA, USA) at 25 mg ml^{-1}. A 10 µl Hamilton syringe (HPLC/GC/TLC, 701 N, Hamilton Europe, Bonaduz, Switzerland) with a blunt tubular needle was used for intracranial injection. The needle was connected to a 24G internal cannula with a length of 3 mm (INC26-30, World Precision Instruments, Hertfordshire, UK) via approximately 30 cm of PE tubing (O.D 1.1 mm, I.D. 0.6 mm) (504280, World Precision Instruments, Hertfordshire, UK). The system was washed and pre-filled with mineral oil (M5904 Sigma-Aldrich, MO, USA). Then, it was back filled with at least 14 µl of FITC-dextran solution and loaded on a syringe injector (Legato130, KD Scientific, MA, USA). The system was locked in place to the guide cannula by a fixing screw (504281, World Precision Instruments, Hertfordshire, UK) throughout the duration of the inject. Injection speed was set at 0.1 µl min^{-1} and a total volume of 10 µl was injected for each repeat of measurement. Animals were allowed for 20 minutes of rest before the internal cannula was removed and replaced by the dummy cannula.

2.10.13 *In vivo* photo-bleaching and recording

In vivo photo-bleaching and the recording of the fluorescence recovery curve were carried out in in the same way with the identical equipment set-up as the *in vitro* photo-bleaching and recovery in the gels. FITC-dextran was photo-bleached with the 488 nm laser diode with a power of 1.3 mW for 30 second. Photometry recording was carried out using the 465 nm LED diode with a power of 1.6 µW. The mechanical shutter was programmed for a repeating cycle of 30-second ON followed by a 3570-second OFF during the period of *in vivo* recording of animals.

2.10.14 EEG and EMG recordings with the Neurologger

Electroencephalogram (EEG) and Electromyogram (EMG) data were recorded using a miniature data logger connected to the EEG and EMG electrodes on cortex and muscle via the pin connector. A description of the data logger (Neurologger) can be found in Hsieh (2019). The Neurologger measures the voltage difference between the two electrodes positioned on top of the mouse brain cortex and between the conductive wires imbedded underneath the neck muscle. Theses voltage differences are recorded on onboard memory storage and can be later retrieved to a PC via a customise downloader. The Neurologger operates with two zinc air batteries without the need of a tether. It typically records EEG and EMG data at a sampling rate of 200 Hz for at least 24 hours continuously. EEG and EMG data were downloaded with the customise downloader and used as a direct input for the customise analytical script using MATLAB.

2.10.15 Intraperitoneal injection of dexmedetomidine

Dexmedetomidine (Dexdomitor, Orion Parma, Espoo, Finland), was diluted in 0.85% saline (Oxoid, Thermo Fisher Scientific, MA, USA) and injected intraperitoneally in mice at a dose of 200 µg kg^{-1}. The injection was carried out at 6 hours after the infusion of FITC-dextran. Animals were kept on a homeothermic blanket connected to a thermostat (69020, RWD, Guangdong, China) to maintain the body temperature at 36.5 °C throughout the whole period of sedation and recording.

2.10.16 Brain sectioning

At different time points, mouse was sacrificed by euthanasia with intraperitoneal injection of at least 200 mg kg^{-1} sodium pentobarbital (Pentoject XVD133, Animalcare, York, UK). After confirming death, brains were taken out directly by dissecting. Fresh brain was snap frozen in dry ice cooled pentane (236705, Sigma-Aldrich, MO, USA) for 5 minutes and then stored at -80 °C before sectioning.

Brains were sectioned with Leica cryostat (CM3050 S, Leica Microsystems, Milton Keynes, UK) at -15 °C in thickness of 30 µm. Brain sections were defrosted and dried on adhesion slices (SuperFrost Plus, Thermo Fisher Scientific, MA, USA) and mounted with DPX mounting medium (BCCD8334, Sigma-Aldrich, MO, USA) before imaging.

2.10.17 Widefield microscopy

Brain sections were imaged using widefield microscopy (Axion Observer, Zeiss Microscopy, Cambridge. UK) with a Lumencor Sapectra X (NW, USA) dichroic filter with an excitation wavelength at 470/40 nm and emission wavelength at 250/50 nm. All images were taken with 200 ms exposure time under 10X magnification. Images were processed with software Zeiss Zen and ImageJ.

2.10.18 MATLAB script for data analysis

The script for data analysis was written with the help of another Ph.D. student Bryan Hsieh. A copy of the script can be found in the Appendix.

This script was written and tested in MATLAB (The MathWorks Inc, Natick, MA, USA, version 9.8.0.1417392) with Windows 10 64-bit operation system. The script requires the following toolboxes to function: Curve Fitting toolbox, Signal Processing toolbox, and Statistics and Machine Learning toolbox.

The function of this script is to simultaneously identify vigilance states (WAKE, REM, NREM) based on the EEG/EMG data, at the same time calculating effective diffusion coefficients by fitting

curves of the photometry data using the mathematical model described in Section 2.1. Here is an instruction of how to organise data and operate the script using MATLAB:

Data must be stored in three separate folders, labelled "Photometry", "EEG", "Time". The folders must contain Photometry data as .csv files, EEG and Time (starting time, one line per data) data as .txt files. Photometry and EEG data need to be labelled with a two-digit integer suffix and data from the same experiment must have the same suffix e.g. {EEG01, Photo01}, {EEG02, Photo02}. User will be asked at the start of the script to point to the folder containing the three separate sub folders. The script will allow the user to either select a particular data to analyse or to analyse all data automatically.

The sample data provided is contained in a single folder with sub-folders organised as described above. The photometry data has two columns, first one being real time and second one being fluorescent intensity. The EEG/EMG data has four columns, with column one being EEG signal, column 3 and 4 being EMG signals. The script is able to identify the organisation of data automatically. The EMG/EEG data has been sampled at a frequency of 200 Hz. The EEG/EMG data has been temporally aligned with the photometry data prior to this analysis.

The script has been annotated with detailed instructions and comments, but the general steps of processing data are as the followings. (1) This script should be saved in the same directory of the main data folder. (2) Open and run the script in MATLAB. (3) Select the working folder containing the three sub-folders (Photometry, EEG, Time). (4) Enter 1 and click OK, since all the data in this experiment was processed automatically. (5) Enter starting file number, in this case “1” and click OK. (6) The script should start processing data without any further manual input. (This can take up to a few minutes per experimental data. Scoring and fitting data should be presented subsequentially on screen as the processing proceeds. (7) After analysis finishes, all figures are saved for inspection in the respected folders by experiment and a combined data sheet is generated automatically. All these data will be saved in the same fold of the main folder.

“Data_Combined.csv” is the final output of the script. The following data is extracted from the “Data_Combined.csv” file for further analysis and plotting: (1) Column Number 7: “Wake_Total” which indicates the total percentage time of wakefulness the animal has spent in that particular

hour of photo-recovery period. (2) Column Number 16: “D_Full”: the effective diffusion coefficient calculated for that particular hour when fitting the full length of the recovery curve is fitter to estimate a diffusion coefficient. (3) Column Number 20: “Time_of_Day”: represents the natural time of the day when this particular photo-recovery curve occurs.

5.10.19 Statistical analysis

Statistical analysis in the current project was carried out under the Estimation Statistics framework (Ho *et al*., 2019) where an effect size and 95% confidence interval are shown to demonstrate the precision of the estimate. The bootstrap method for obtaining a 95% confidence interval is a bias-corrected and accelerated bootstrap method (Efron, 1992) which works on non-parametric data. In the current project, the method resamples the observed dataset 5000 times and determine the middle 95% of the distributions. This method was performed with the website Estimation Statistics www.estimationstats.com.

One-way ANOVA was also used to make comparisons in the current project. The estimation plot (Figure 3-13 and Figure 4-6) is multi two-group estimation plot (Cumming plot) (Cumming, 2013). Top panel shows the distribution of individual data points, with middle of the vertical bars showing mean of the data and the vertical bars showing the standard deviation for each group. Bottom panel shows the mean difference relative to the average of all the data, with bootstrap 95% confidence interval shown in the vertical bar next to the scatter plot.

Chapter 3 *In vitro* Experiment Results

Based on the experimental design and development described in the previous chapter, A series of experiments were performed. In this chapter, the data for all experiments carried out outside the animal are presented and explained. Firstly, the chemical properties of FITC-dextran were demonstrated and then the light distribution in brain phantom gels and in freshly sliced tissues were profiled to estimate the standard deviations used to fit the fluorescent recovery curves. After that, a direct method of measuring diffusion coefficients of FITC-dextran was used to validate the method. Finally, the method was further tested in a controlled convection environment.

3.1 Using FITC-dextran as the fluorescent tracer

3.1.1 FITC-dextran has an absorption peak wavelength at 495 nm

To characterise the fluorescent profile of FITC-dextran, a scanning spectrometer was used. Samples of FITC-dextran (4 kDa, 0.35 mg ml^{-1}) before and after complete photobleaching was scanned with the scanning spectrometer for the wavelength between 200 nm and 800 nm. The result is shown in Figure 3-1. The results suggest that FITC-dextran has an absorption peak at around 495 nm. It also shows that FITC-dextran can be photobleached completely by light at the 495 nm. Conclusively, the light absorption peak of FITC-dextran at 495 nm suggests that FITC-dextran should be excited by light around 495 nm for maximal fluorescent emission.

Absorption peaks at wavelength shorter than 400 nm are caused by autofluorescence of material from the solvent solution, and absorbance in the range was not recorded nor relevant to the current study.

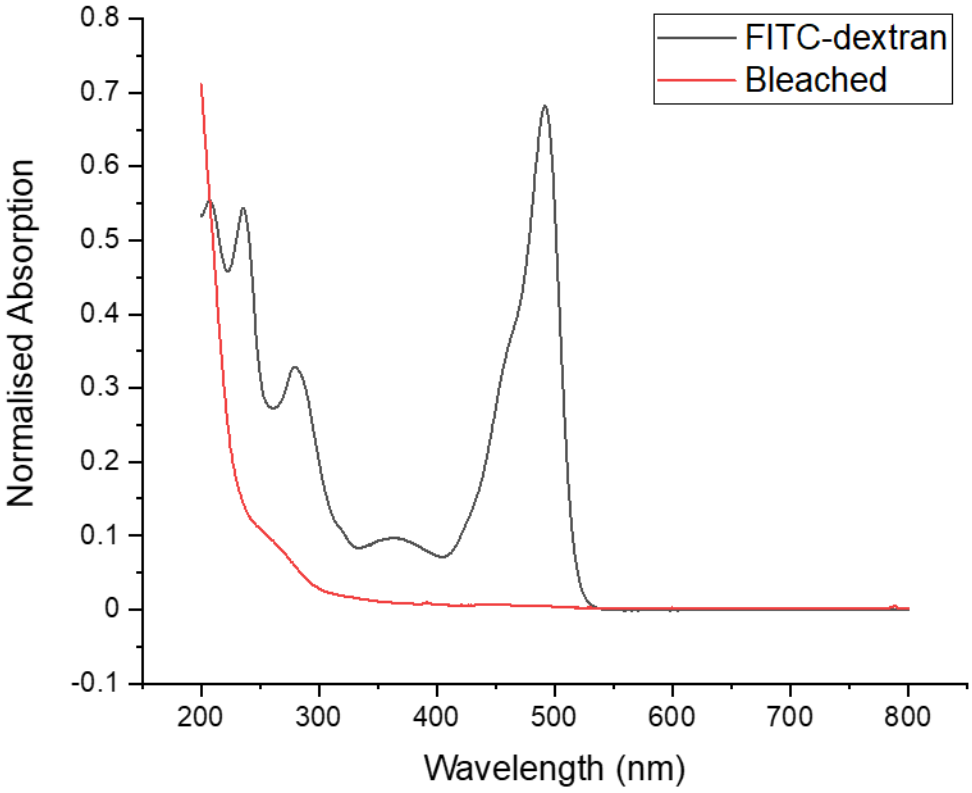

Figure 3-1 Light absorption of FITC-dextran and bleached FITC-dextran. Material is dissolved at a rate of 0.35 mg ml^{-1} is PBS (pH 7.4). Absorption was normalised with blanking solution (PBS) and measured with a UV quartz cuvette. To photo-bleach the solution, a condensed xenon light was used. The solution under constant stirring was photobleached for 10 hours for complete bleach.

3.1.2 FITC-dextran fluorescence is proportional to its concentration

Commercially available FITC-dextran materials contain fluorescein molecules conjugated with dextran sugar in a fixed ratio. The FITC-dextran used in this experiment from Sigma-Aldrich had a FITC: Glucose of 1: 250. The concentration of FITC-dextran solution can be measure by its optical absorbance at its absorption peak wavelength at 495 nm. This has been tested with a spectrocolorimeter, and the results are shown in Figure 3-2. Various concentration levels of FITC-dextran (molecular weight 4 kDa) were made with PBS and absorbance at 495 nm was measured. A Pearson's linear correlation test confirms that the FITC-dextran's peak excitation hence fluorescence level is a true indication of its actual concentration level (r=1.00).

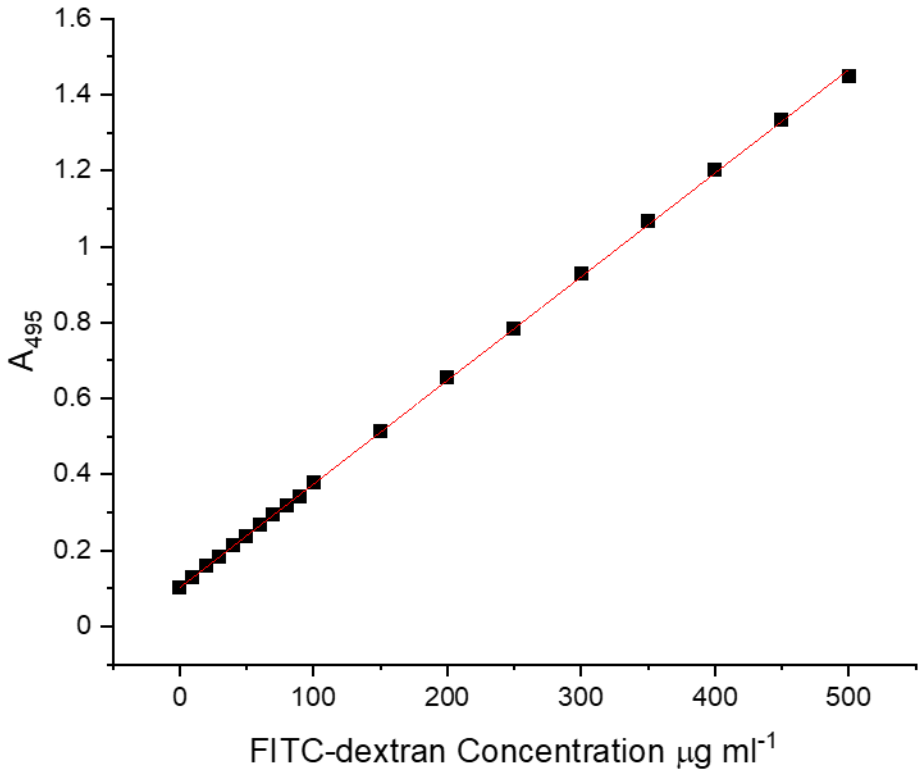

Figure 3-2 Absorbance of different concentration levels of FITC-dextran at 495 nm. FITC-dextran (molecular weight 4kDa) was dissolved in different levels of concentration in PBS. Light absorbance at 495 nm was measured with a spectrocolorimeter. Red line: a Pearson's linear correlation has been fitted with the data (r=1.0).

3.1.3 FITC-dextran can be photo-bleached without chemical recovery

Using FRAP to determine diffusion coefficient assumes that the fluorescence recovery observed results solely from the influx of unbleached dye from the area surrounding the bleached volume. This requires the dye is bleached permanently without any chemical conversion of bleached FITC-dextran back to unbleached form. To validate this, a solution of FITC-dextran solution was completely photo-bleached, and absorption at 495 nm was measured.

0.1 mg ml^{-1} FITC-dextran (4 kDa) PBS solution was photo-bleached for 10 min with a focused xenon light source. Light absorption at 495 nm (A_{495}) were measured before, immediately after and sometime after the photo-bleaching treatment. The results are shown in Figure 3-3. The result suggests that FITC-dextran was completely bleached at its absorption peak of 495 nm after exposing to the light source for 10 min. Bleached FITC-dextran remained bleached and no chemical recovery was detected within 100 min after the bleaching. This reassures the assumption that FITC-dextran can be photo-bleached completely and is unable to recover its fluorescence.

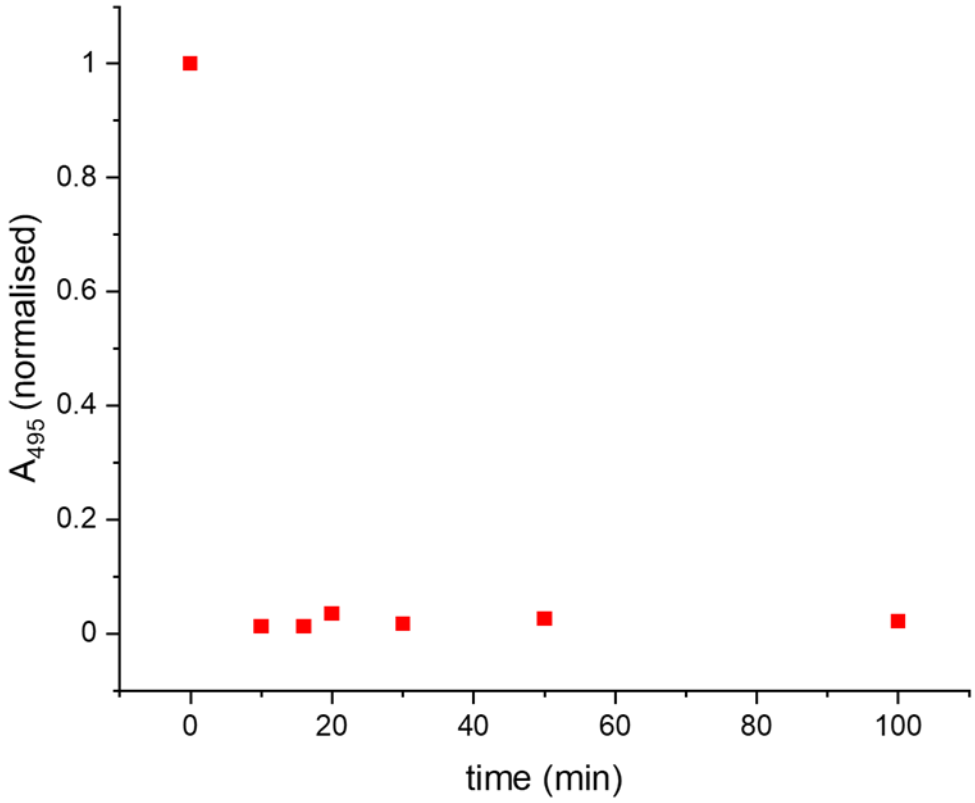

Figure 3-3 Absorption at 495 nm of FITC-dextran PBS solution before and after xenon photo-bleaching. Relative A_{495} is normalised with a maximum value before photo-bleaching (*t=0*) and blanking solution (PBS). One single measurement was carried out in this experiment to confirm what was already indicated on the material's product specification and literature information.

3.1.4 FITC-dextran used in the study contains no unconjugated isomer forms

In order to accurately compare diffusion coefficients measured with FRAP method for different molecular weights of FITC-dextran, the materials of FITC-dextran used in the study must contain no unconjugated form of the FITC isomers. This was confirmed with a thin layer chromatography test.

FITC-dextran 4 kDa, 10 kDa and FITC isomer at the concentration of 25 mg ml^{-1}, 10 mg ml^{-1}, 0.13 mg ml^{-1} respectively were used. Chromatography tests were performed to separate the molecules by size. The result of the chromatography is shown in Figure 3-4. Column A contains only FITC isomers; column B contains a mixture of FITC isomers and 4 kDa FITC-dextran; column C contains only 4 kDa FITC-dextran; and column D contains only 10 kDa FITC-dextran. The results suggest that there is no unconjugated FITC isomers detectable in both 4 kDa and 10 kDa FITC-dextran samples. Mixing FITC isomers with FITC-dextran does not results in deconjugation of the polymers.

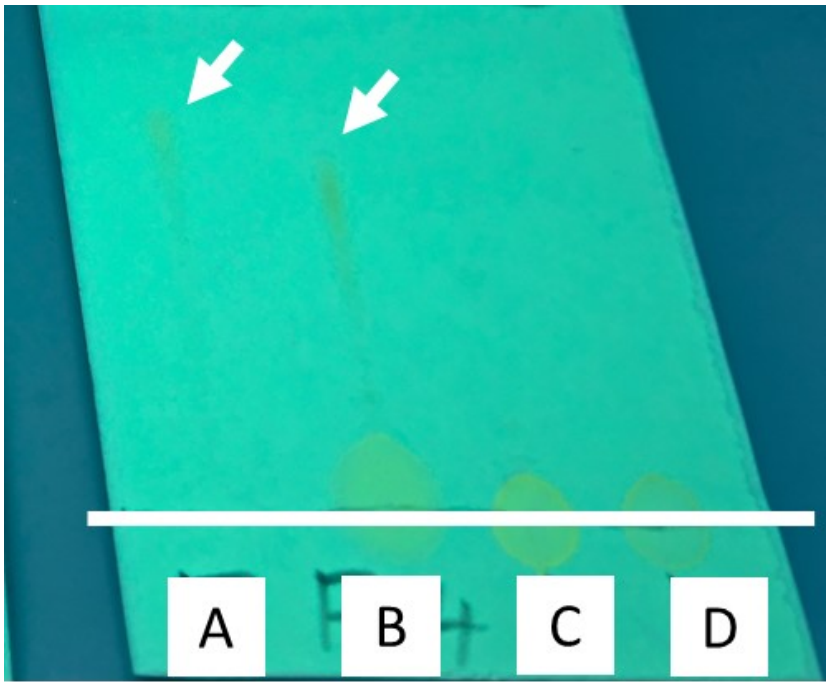

Figure 3-4 Chromatography test for unconjugated FITC isomer. A: FITC isomer; **B**: FITC isomer and 4 kDa FITC-dextran; **C**: 4 kDa FITC-dextran; **D**: 10 kDa FITC-dextran. Image was taken under UV illumination. White arrow indicates FITC isomer separated by mobilisation.

3.1.5 A_{495} of FITC-dextran is pH sensitive

Absorption of FITC-dextran at 495 nm (A_{495}) was measured when the material is dissolved in PBS adjusted at different pH levels. FITC-dextran 4 kDa was dissolved at 0.1 mg ml^{-1} and light absorption was measured with a scanning spectrometer from 200 nm to 800 nm. The results are shown in Figure 3-5. The results suggest that FITC-dextran has a peak absorption at around 495 nm under the condition between pH 6.5 to pH 10. Within this pH range, fluorescent intensity at 495 nm is pH sensitive. The brain phantom solution (8% milk and 0.1% Indian ink dissolved in PBS) has a pH of 6.5. There is also a sufficient fluorescence at the physiological pH in the range around pH 7.4. Therefore, when FITC-dextran is dissolved in the brain phantom solution, light with 495 nm should be used to excite for fluorescence.

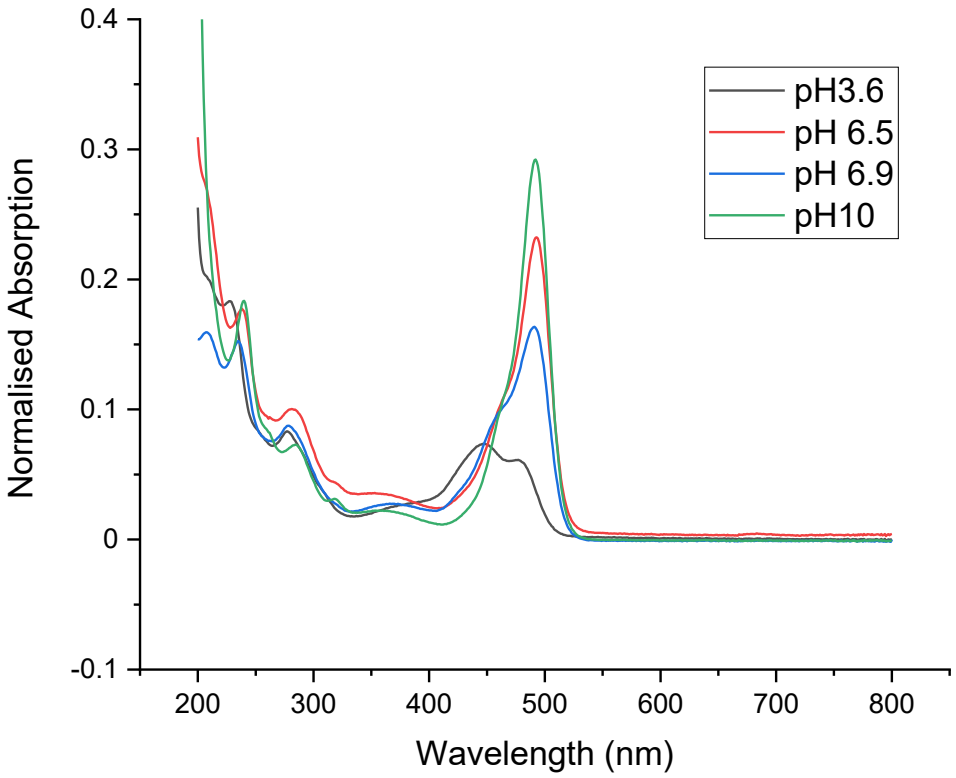

Figure 3-5 Light absorption of FITC-dextran dissolved in various pH solutions. Absorption was blanked with PBS solution and normalised. FITC-dextran 4 kDa was dissolved at 0.1 mg ml^{-1} respectively.

3.2 Profiling light distribution of the fibre-optic photometry system

3.2.1 FITC-dextran is photobleached by high-intensity light

An optical fibre with a 200 µm diameter identical to the one being implanted in the brain was inserted in an 800 µm-thick brain phantom gel (containing 0.3 mg ml^{-1} FITC-dextran) which was sandwiched by two blocks of agarose gel (see Experiment Design Figure 2-5). The same laser at an emission wavelength of 488 nm was connected to the optical fibre. An intense light at approximately 1.3 mW was delivered through the fibre to photo-bleach FITC-dextran dye in the gel at the fibre tip. The intensity of bleaching was imaged after different duration of photo-bleaching. The results are shown in Figure 3-6A. The images indicate that intensive light at 488 nm results in loss of fluorescence at the tip of the optical fibre; the longer the bleaching time, the more fluorescence is lost. The shape of the bleached area is close to spherical, with the centre being the most intense bleaching, shown in the surface plot. This bleaching was repeated with new gel blocks (n=7) and the fluorescence lost, which was represented by lowered average pixel intensity of the images was correlated with the relative distance to the centre of the bleaching (the tip of the fibre), shown in Figure 3-6B. The results confirmed the loss of fluorescence of the dye due to the exposure of high intensity light, the longer the exposure, the higher level of bleaching intensity.

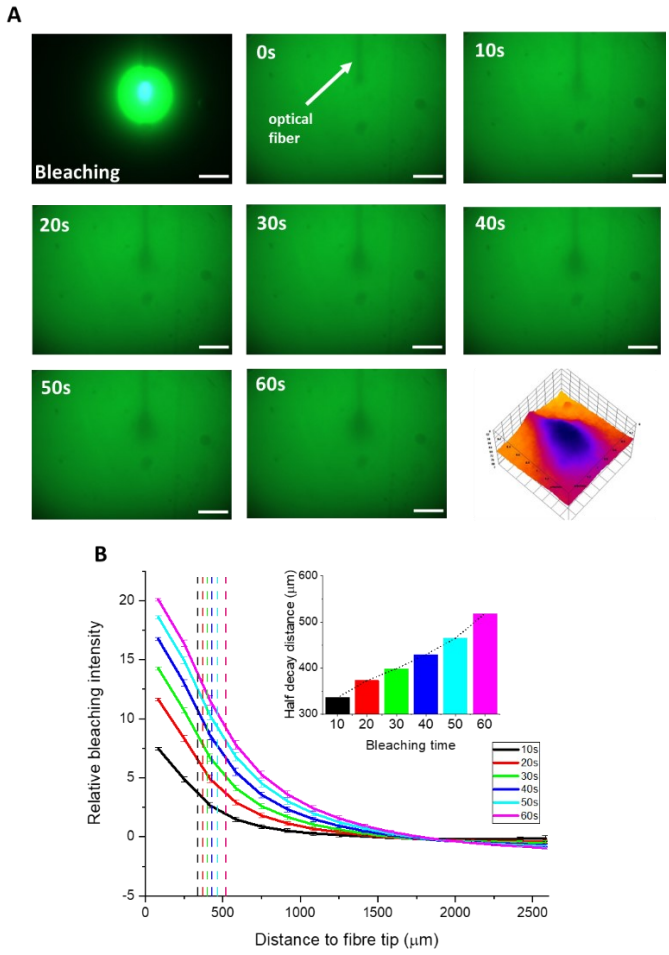

Figure 3-6 Brain phantom gels containing FITC-dextran is photobleached by high-intensity light. An 800 µm thick brain phantom gel section is sandwiched by two clear agarose gel and inserted with a 200-µm diameter optical fibre. High intensity light at approximately 1.3 mW is applied at the fibre tip. Levels of photo-bleaching were captured for different durations. **A:** Accumulative level of photo-bleaching was indicated by the darkening shade at the fibre tip after 0 s, 10 s, 20 s, 30 s, 40 s, 50 s, and 60 s of photo-bleaching. Scale bar: 1000 µm. The shape and intensity of the bleached volume is shown in the surface plot. Scale bar: 1000 µm. **B:** Lower line graph shows relative photo-bleaching intensity estimated from normalised pixel intensity in relationship to the distance to the tip of the optical fibre. Dotted line: distance to the fibre tip where bleaching intensity has decayed by 50%. Error bar: standard error of the mean over 7 individual optical fibre insertions and photo-bleaching. Upper bar graph shows distances to the fibre tip where bleaching intensity has decayed by 50%.

3.2.2 Light distribution in brain phantom gel

Light distribution from the optical fibre was measured in the brain phantom gel sandwiched by two clear gel blocks as described in Experimental Design (Figure 2-5). The light was captured and imaged under a fluorescence microscope (Figure 3-7A). When image was digitised, the light distribution was characterised by fitting to a hemispherical Gaussian distribution on the axial axis and full Gaussian distribution on the radial axis; one example showing in Figure 3-7B. It results show that the light distribution is well characterised by Gaussian fittings. The sigma value used for estimating diffusion coefficients in brain phantom gels was calculated from the mean standard deviation of the two axis. The mean σ value calculated from light distribution in brain phantom gel is determined to be 149.5 µm with a confidence interval from 140.7 to 162.6 µm, averaged from n=8 individual gel-illumination replications.

The calculated σ was then corrected to account for the small amount of diffusion occurring during the 30 seconds of bleaching when verifying the method in gel as described in the Experimental Design (Section 2.4). After correction, the σ values used to calculate effective diffusion coefficients for FITC-dextran at 4 kDa, 10 kDa and 70 kDa are 152.1 µm, 156.2 µm, and 161.0 µm with confidence intervals of 143.3-165.0 µm, 147.7-169.0 µm, and 152.6-173.2 µm, respectively.

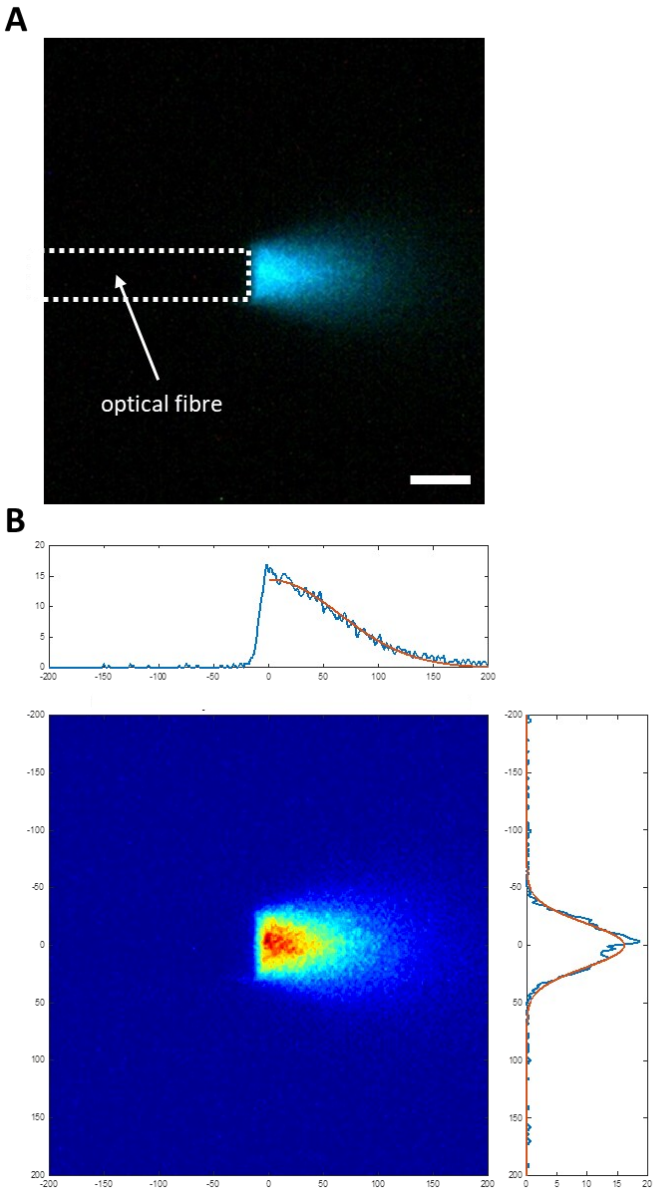

Figure 3-7 Light distribution from the optical fibre in brain phantom gel. An 800-µm thick brain phantom gel containing 0.3 mg ml^{-1} FITC-dextran (M.W.: 4kDa) is sandwiched by two clear gel blocks and inserted with the 200 µm (diameter) optical fibre. A LED light source at a wavelength of 465 nm is connected to the optical fibre and illuminate the gel with light at a power of 1.6 µW. Image is captured with a fluorescence microscope with an exposure time of 200 ms. **A**: Light distribution at the fibre tip. **B**: The imaged is digitised with pixel intensity. Light distribution is fitted to a hemispherical Gaussian distribution on the axial axis and full Gaussian distribution on the radial axis.

3.2.3 Sigma was determined from light distribution in freshly sliced brain sections

Mice were killed and had brains taken out by dissection. A vibratome was used to section the brain at 800-µm thickness. Optical fibres were inserted into the freshly sliced brain sections at different tissue locations. The light distribution from the optical fibre is imaged by a fluorescence microscope. Demonstrated in Figure 3-8, optical fibres were inserted into the frontal cortex (A), motor cortex (B), striatum (C), thalamus (D) and amygdala (E). The captured images were converted into 8-bit images and matrixes based on the pixel location at their 8-bit pixel intensity Images were created. In this way, the images were digitised into such matrix for the curve following curve fitting processes. A hemispherical Gaussian curve was fitted along the axial axis (X) and a full Gaussian curve was fitted along the radial axis (Y). As seen Figure 3-8, the geometrical distribution of light from the fibre varies significantly across different histological locations of the brain. A mean σ value was calculated by averaging the two axis for each brain area. The experiment was repeated three times on three individual brains. The images were taken under different exposure time when extra care was taken to avoid over-exposure. The mean σ values for each brain region under 5 s - 50 s exposure time are shown in Figure 3-9A. As seen in the figure, exposure times did not cause significant differences in the fitted sigma values. Rather, mean sigma value varies greatly between brain areas with the highest in thalamus (318 µm) and lowest in the frontal cortex (191 µm). The mean sigma value for the amygdala, striatum and motor cortex are 276 µm, 265 µm, and 238 µm respectively (Figure 3-9C). The ratio between the sigma value on the radial axis (Y) against the sigma value on the axial axis (X) is also calculated for each brain region (Figure 3-9B). Y/X closer to 1 indicates more circularity of the light distribution resulting from more scattering effect of the brain tissue. There are great variation of the Y/X ratio, hence circularity across different brain regions, shown and compared in Figure 3-9D. The highest circularity of the light distribution pattern is found in the thalamus and the lowest in the frontal cortex.

In the *in vivo* experiments estimating effective diffusion coefficients, optical fibres are implanted in the frontal cortex of the brain. σ values from the fontal cortex were estimated from the light distribution captured by imaging. One example determining σ values from images by Gaussian fittings are shown in figure 3-10A. Mean σ value from the Gaussian curves fitted from the

digitised images from the frontal cortex was determined to be 128.9 µm, with a confidence interval of 116.5 to 141.3 µm (n=7) (Figure 3-10B). To calculate diffusion coefficients from *in vivo* photo-bleaching and recovery curves, the mean σ value estimated from these images was mathematically corrected for the 30-s diffusion of 4 kDa FITC-dextran. The final σ value used in *in vivo* curve fittings is 134.3 µm. This σ value was applied to the automatic sleep scoring and curve fitting script used for all *in vivo* experiment analysis.

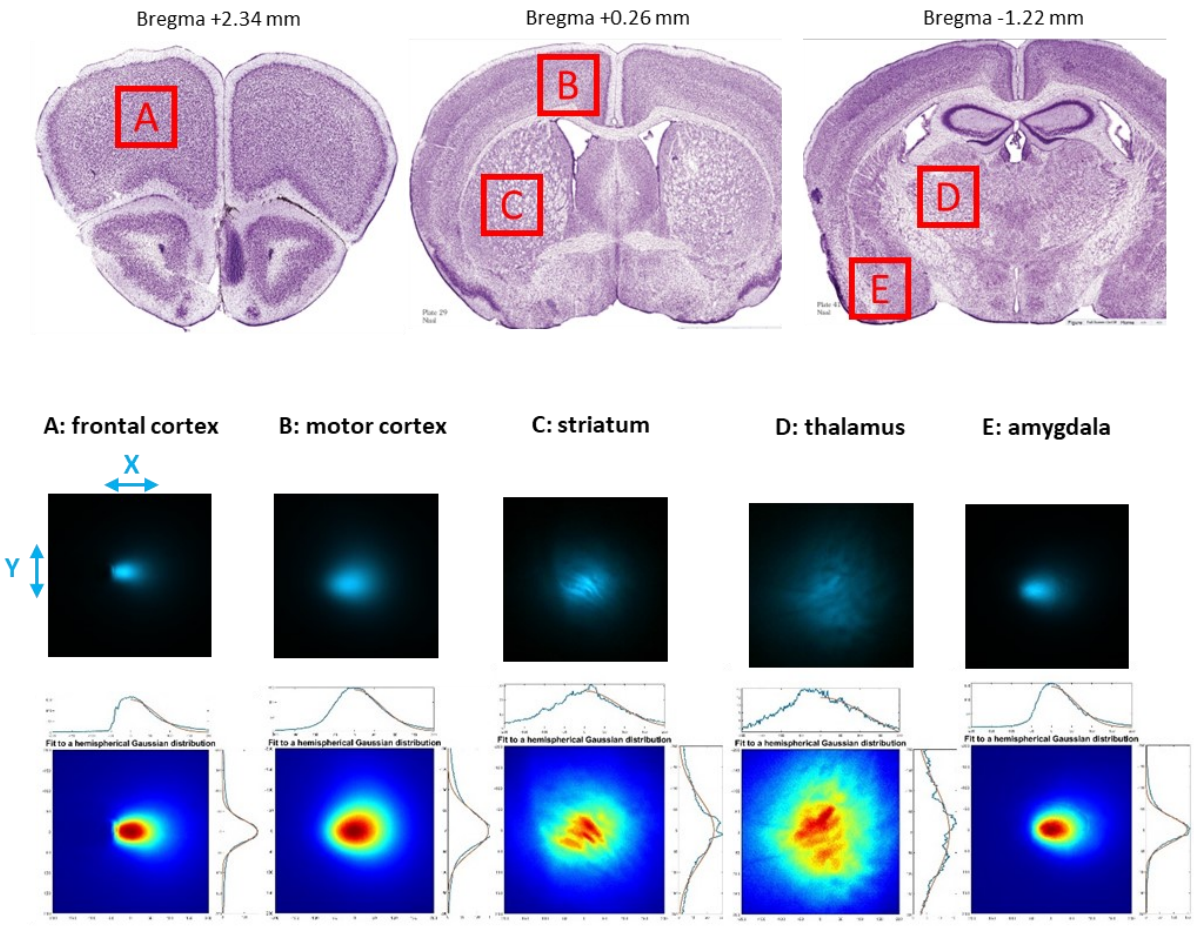

Figure 3-8 Light distribution from the optical fibre in freshly sliced brain sections. A 200 µm thick optical fibre is inserted in various brain regions of freshly sliced brain sections. The brain section is sandwiched by two clear gel blocks and imaged by a fluorescence microscope. A LED light source at a wavelength of 465 nm is connected to the optical fibre and illuminate the gel with light at a power of 1.6 µW. Top panel shows locations where the optical fibres were positioned, image adapted from The Mouse Brain in Stereotaxic Coordinates, (Paxinos and Fraklin, 2019). Bottom panel: digitised images were fitted with a hemispherical Gaussian curve along the axial axis (Y) and a full Gaussian curve along the radial axis (Y).

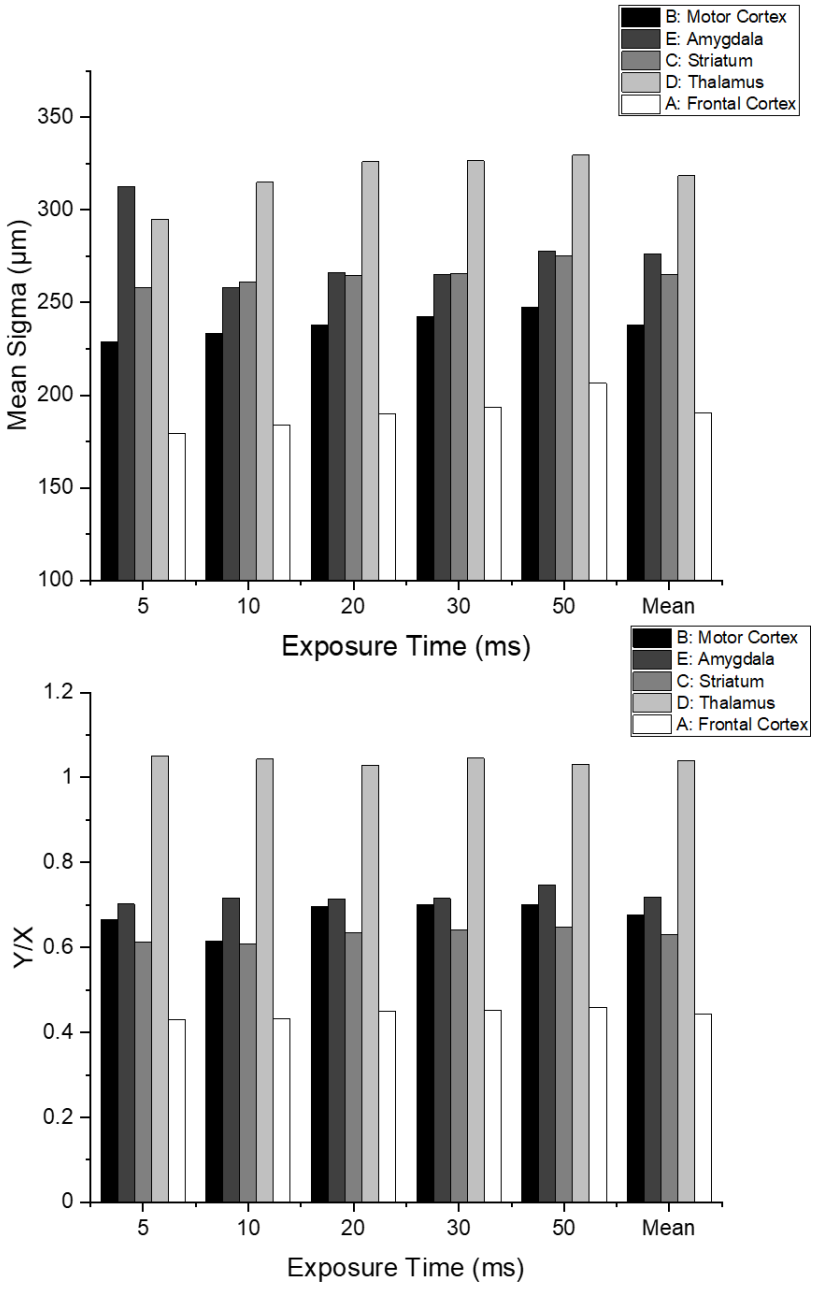
B: Motor Cortex
E: Amygdala
C: Striatum
D: Thalamus
A: Frontal Cortex
Mean Sigma (µm)
350
300
250
200
150
100
5
10
20
30
50
Mean
Exposure Time (ms)
B: Motor Cortex
E: Amygdala
C: Striatum
D: Thalamus
A: Frontal Cortex
Y/X
1.2
1
0.8
0.6
0.4
0.2
0
5
10
20
30
50
Mean
Exposure Time (ms)

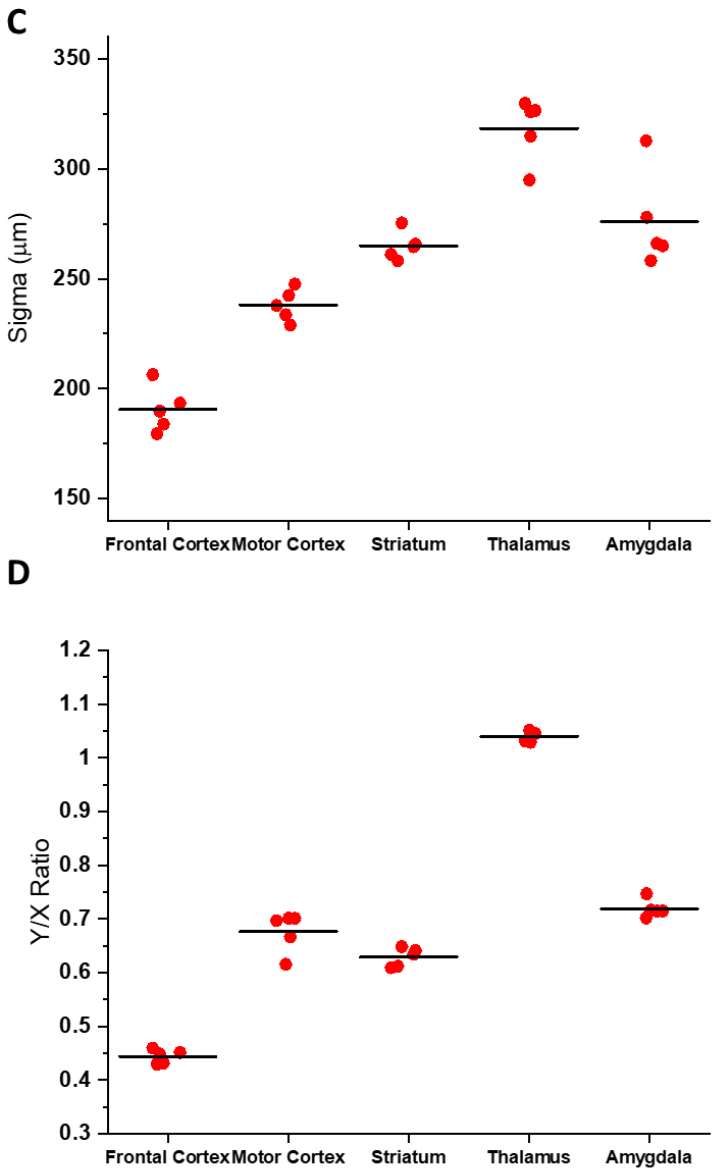

Figure 3-9 Mean sigma values and Y-X ratio in different brain regions. The optical fibres were inserted in different brain regions. Images of light distribution at the fibre tip within these brain tissues were captured by fluorescence microscopy. Images were converted to 8-bit and a matrix of each pixel's intensity was created to digitise the light distribution at the fibre tip. Two axis were created along the axial (X) and radial (Y) directions of the optical fibre. Gaussian distributions were fitted along X and Y axis of the light distribution and the standard deviation (σ) of the Gaussian fitting were calculated. **A:** Sigma values for each of the five fibre-inserted brain regions

at different exposure time during image capture. Mean σ values is calculated by averaging the sigma values from the axial axis and from the radial axis. **B:** The ratio of sigma values between the Y axis and the X axis for each of the five fibre-inserted brain regions at different exposure time during image capture. The mean column on the graphs shows the average mean sigma values or Y/X values across the five different exposure times. **C:** Sigma values at different brain regions. Black solid lines show the mean sigma value for each brain region. **D:** Y/X ratio for each brain regions, Black solid lines show the mean Y/X ratio for each brain region.

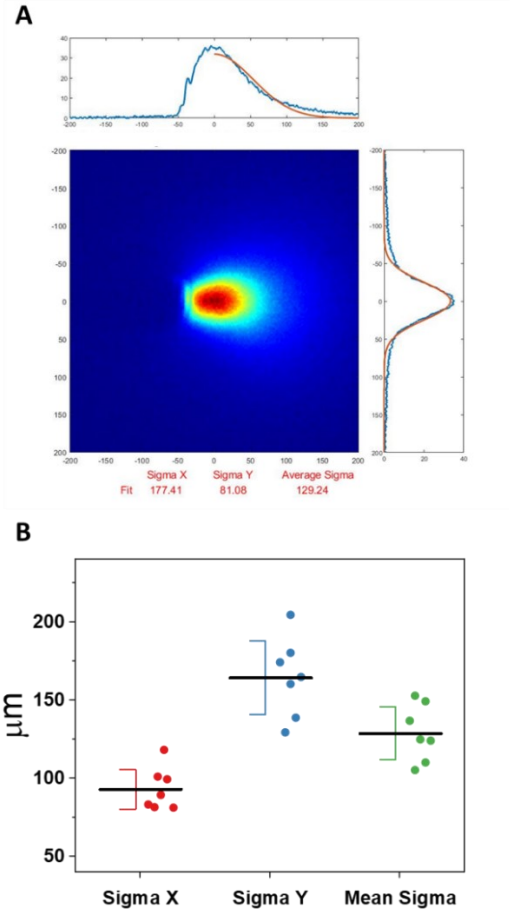

Figure 3-10 Gaussian fitting of light distribution in freshly sliced brain section. Light distribution was measured by inserting an optical fibre into the frontal cortex of freshly sliced mouse brain sections. Images were taken with a fluorescent microspore and converted into a matrix according to pixel intensity as described previously. A hemispherical Gaussian curve was fitted along the axial axis and a full Gaussian curve was fitted along the radial axis. The sigma values were calculated as the standard deviation of the two Gaussian curves, respectively. An average sigma value between the two axis was used to determine the final mean sigma value. **A:** An example of Gaussian curve fitting of light distribution captured in freshly sliced brain section, where the sigma values for X and Y axis are 177.4 and 81.1 µm, resepectively, resulting in a mean sigma of 129.2 µm. **B:** Fitted sigma values for seven individual experimental repeats (n=7). Each time a fresh brain slice was sectioned with an optical fibre inserted. Data show sigma values for along X and Y axis of the fitting as well as the mean sigma value for each measurement.

3.3 Direct measurement of the diffusion coefficients of FITC-dextran

A technical approach to measure the diffusion coefficients of FITC-dextran (4 kDa, 10 kDa and 70 kDa) was designed and constructed. As described in Section 2.5, FITC-dextran contained in a thin sheet of gel was only allowed to diffuse out via one side. The dye was allowed to diffuse out into a stirred bathing solution. A 200 µm thick fibre was placed at the bottom of the sheet where the fibre-optic photometry system was connected to record the change of fluorescence intensity at the tip of the fibre. As described by Equation [5], as the dye inside the gel diffuses out, the fluorescence signal decreases. When fluorescent intensity is proportional to the concentration of the FITC-dextran molecules, the concentration of the dye decreases during the time course of the recording.

Ten individual experimental replications were made to measure D for each molecular weight when a fresh gel was made for each photometry recording. Fluorescence intensities recorded by the photometry system were normalised to be shown as the fraction of the initial intensity for each recording. Mean fraction of the initial intensity for each molecular weight is shown in Figure 3-11A. As seen in the results, 4 kDa FITC-dextran has a much faster reduction of fluorescence whereas 70 kDa decreases the slowest. The D values for each individual experimental repeat are also shown. These data show high consistency with great degree of confidence (95% confidence intervals shown in the coloured ribbon and the whisker brackets). One example of the reduction of fluorescence intensity during diffusion is shown in Figure 3-11B. It confirms that Equation [5] was able to accurately characterise this course of concentration reduction.

The mean diffusion coefficients measured are 133.93, 73.46 and 26.49 $\mu m^2 s^{-1}$ (4 kDa, 10 kDa and 70 kDa respectively) with 95% confidence intervals of [124.23, 141.88], [67.57, 79.48] and [23.99, 29.73], respectively.

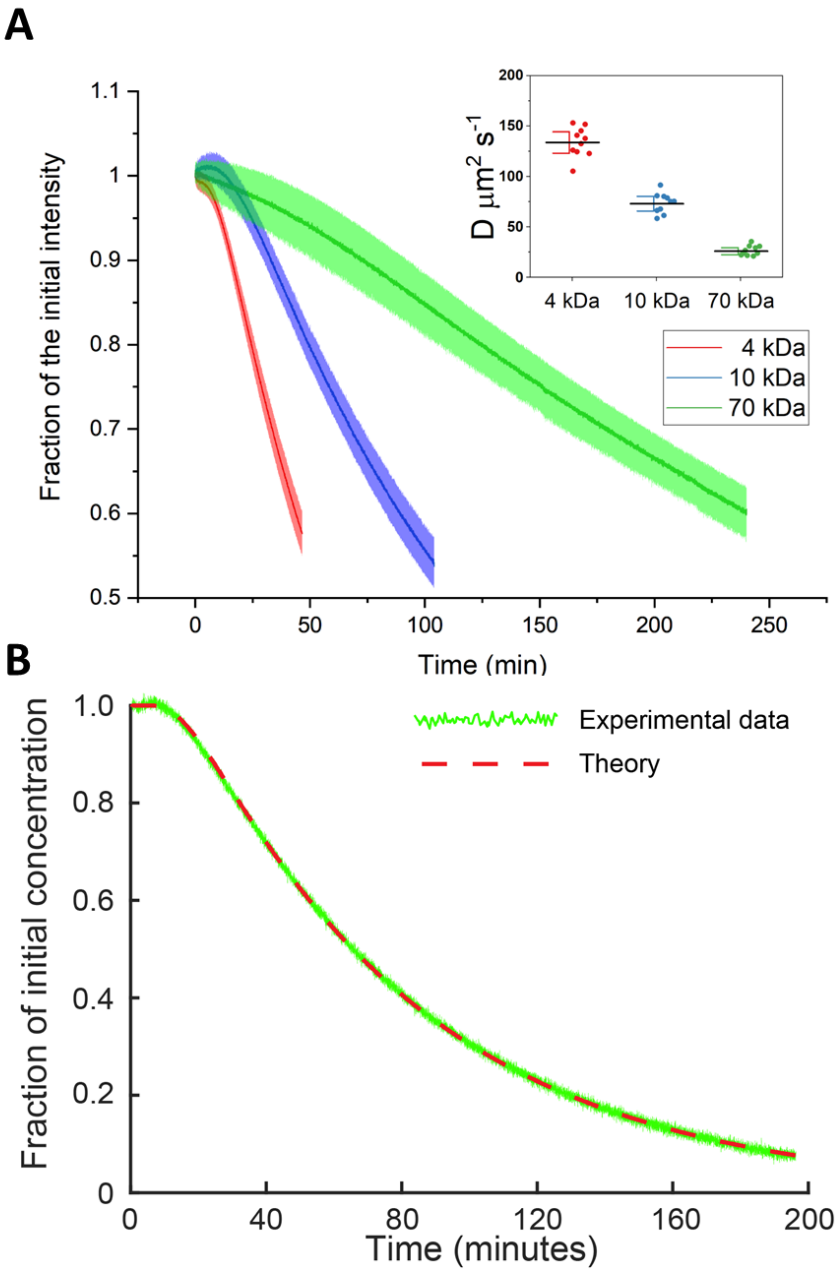

Figure 3-11 Direct measurement of diffusion coefficient with the fibre-optic photometry system. A. Three molecular weights of FITC-dextran were individually dissolved in the thin sheet of brain phantom gels. The fibre-optic photometry system was used to measure the fluorescence reduction as the molecule is diffusing out of the gel. Ten experimental repeats with new gels were made for each molecular weight (n=10). The line plot shows the mean fraction of the initial intensity of the ten experimental repeats for each molecular weight. The coloured ribbon indicates 95% confidence interval. Each individual photometry recording was fitted with Equation

5 to calculate the corresponding D values. Individual calculated D from the curves are in the grouped scatter plot (top-right) where the black lines show mean D values, and the whiskers show the 95% confidence interval. **B.** Example of the reduction of fluorescent intensity/FITC-dextran concentration when directly measuring diffusion coefficient with a thin sheet of brain phantom. The fibre-optic photometry system was used to measure the diffusing-out of the FITC-dextran dye from a brain phantom gel. **Green trace**: concentration of FITC-dextran indicated by FITC-dextran fluorescence exited at 465 nm and normalised as a fraction of the initial concentration. **Red dotted line**: Theoretical prediction (Equation 5) of the reduction of concentration due to the diffusion of FITC-dextran dye from the dye to the surrounding bath.

3.4 Validation of the method in brain phantom gels

The FRAP with optical fibre method was validated with brain phantom gels. Brain phantom gels individually containing the three molecular weights of FITC-dextran dye were prepared and an identical fibre to the animal implantation was inserted. The same photometry system set up was used to photo-bleach the dye in the gel and the recovery of the fluorescence intensity was recorded for each gel sample. The system was kept at a constant temperature of 20°C. Mean fraction of the initial intensity in a function of time for each molecular weight, and the calculated mean diffusion coefficients from these fluorescence curves are shown in Figure 3-12A. One example of the fluorescence recovery after the 30-second photobleaching is shown in Figure 3-12B. $M(t)/M(0)$ was normalised to the bassline fluorescence intensity prior to bleaching and plotted against time for the first 25 minutes. The result indicates that in the phantom gel where convection was blocked, fluorescence was able to recover to the baseline level in around 25 minutes. The theory (Equation [5]) which characterises the number of moles of bleached dye in the bleached volume (M) as a function of time (t), given that σ was successfully estimated empirically was able to accurately fit the fluorescence recovery curve and a diffusion coefficient can be calculated from the fluorescence recovery curve.

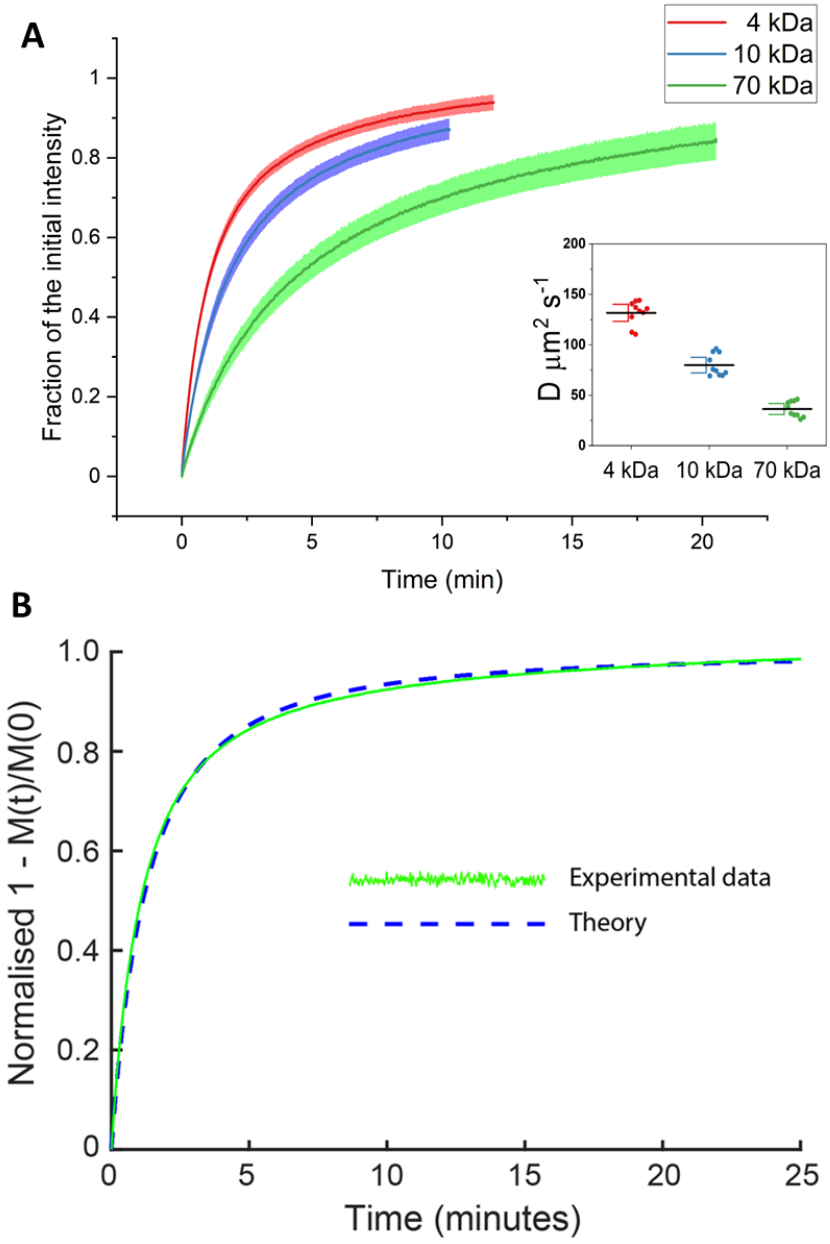

Figure 3-12 Photo-bleaching and recovery in brain phantom gels. A: Photometry recording of the fluorescence recovery of photo-bleaching for each molecular weight of FITC-dextran. Ten experimental replications were made for each molecular weight and the fluorescence intensity was normalised by the initial intensity prior to photo-bleaching. Line graph shows the mean fluorescence recovery with the coloured ribbons representing 95% confidence interval of the repeats. Grouped scatter plot shows the diffusion coefficient calculated from each individual fluorescence recovery curve. Black bar shows the mean and whiskers represent 95% confidence

interval of the data. **B.** One example of the mathematically fittings of the fluorescence recovery following photo-bleaching in brain phantom gel**. Green tracer:** one example of the experimental data showing fluorescence recovery after photobleaching. **Dotted line:** theoretical fitting of the curve with Equation 4.

3.4.1 Diffusion coefficients calculated from recovery curves in the gel

Three molecular weights of FITC-dextran were added to the brain phantom gel for photo-bleaching and the recovery curves of fluorescence were recorded with the photometry system. Ten individual gels were made and recorded for each molecular weight, (n=10). The fluorescence recovery curves were fitted with Equation [5] with respected σ values from section 3.2.2.

With this method, the mean diffusion coefficients were calculated for each molecular weight: 131.70, 79.87 and 36.31 $\mu m^2\ s^{-1}$ (4 kDa, 10 kDa and 70 kDa respectively) with 95% confidence intervals of [123.07, 137.35], [74.12, 87.00] and [31.87, 40.78] respectively.

3.4.2 Comparing diffusion coefficients calculated from the two methods

Two different methods were used to calculate the diffusion coefficients of FITC-dextran with molecular weights 4 kDa, 10 kDa and 70 kDa: the direct measurement of fluorescence reduction in a thin sheet of gel; and calculated by fitting the fluorescence recovery curves in a brain phantom gel. The diffusion coefficients calculated from the two methods are compared in Figure 3-13. Top panel shows the distribution of each individual data point for both methods, Direct: direct measurement of diffusion coefficients with a thin sheet of brain phantom gel and dye diffused out (Section 3.3), PB: calculating diffusion coefficients from fitting the photo-bleaching and recovery curves (Section 3.4.1). Each data point represents a preparation of a fresh gel and a repeat of the measurement for both methods. Lower panel shows the difference between the two methods and the 95% confidence interval represented by the vertical bar. Resampling distributions from bias-corrected and accelerated bootstrapping for each comparison is shown in the coloured tail, see Materials and Methods. A two-tailed t-test was performed for each molecular weight between Direct and PB, p=0.71, p=0.19 and p=0.003 for 4 kDa, 10 kDa and 70 kDa respectively. While there is no statistical significance between the two methods for 4 kDa and 10 kDa, the statistics reported that the D values obtained with the two separate methods for 70 kDa varies statistically. However, based on the data from 4 kDa and 10 kDa FITC-dextran and the even distribution of the individual data points, it is still confirmed that both methods were able to estimate D values for FITC-dextran 4 kDa, 10 kDa and 70 kDa.

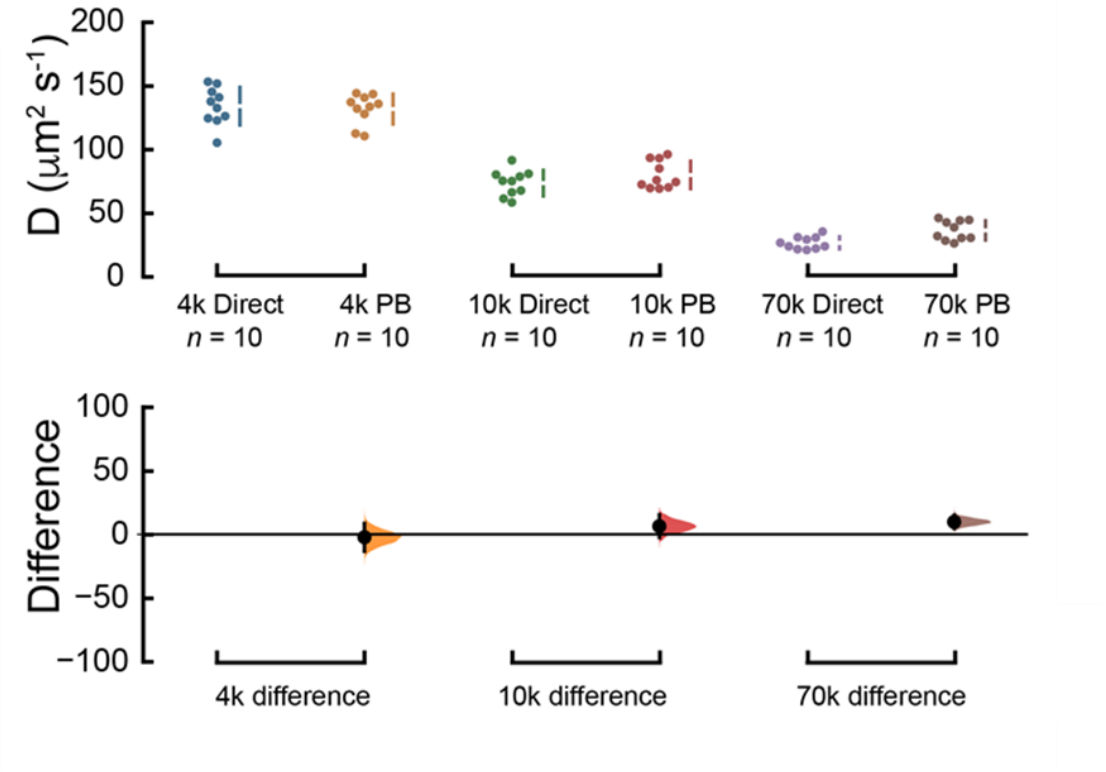

Figure 3-13 Comparison between diffusion coefficients determined by the direct measurement and the photobleaching and recovery method. Top panel shows individual data points for the three molecular weights (4 kDa, 10 kDa, 70 kDa) of both methods. Direct: direct method using a thing sheet of gel; PB: photobleaching and curve fitting method. The vertical bar next to the data set shows the 95% confidence interval of the data with the gap between the bars indicating the means of the data set. Lower panel shows the difference between the two methods with the 95% confidence interval (the vertical bar) and the resampling distributions of the data using a bias-corrected and accelerated bootstrapping method (Ho *et al.*, 2019). Figure generated with estimationstats.com.

3.4.3 *In vitro* bleaching experiments validated the method

Applying the established fibre-optic photometry system in a controlled gel environment and using the theoretical model to calculate the diffusion coefficients from the fluorescence recovery in the brain phantom gel can help to validate the FRAP by fibre-optic photometry method. At the same time, an independent and direct measurement of the diffusion coefficients of FITC-dextran was also achieved. The diffusion coefficients measured by the two independent methods shows great similarities across all the three molecular weights. This agreement confirms that the FRAP by fibre-optic photometry method was able to produce accurate and precise estimates of the diffusion coefficients. Therefore, the FRAP method used for *in vivo* D measurements was successfully validated.

3.5 Test the method in controlled convective flows

The photo-bleaching and recovery method was tested in a controlled convective environment. It is worth noting that, due to the chemical properties, Sepharose gel cannot chemically interact with FITC-dextran nor affect its fluorescent properties. Sepharose gel does not show fluorescence when excited with 465 nm light and cannot be photo-bleached by the 488 nm light.

Three different molecular weights of FITC-dextran (4 kDa, 10 kDa and 70 kDa) were bleached and recorded for the recovery curves under various convection speeds :0, 0.5, 1, 2, 3, 4, 5, 10 and 20 $\mu m\ s^{-1}$. The convection speed is referred to as the linear velocity of the liquid flow calculated from the volume speed divided by the area of the cross-section of the column. Each recording was repeated three times (n=3). The fluorescence recovery curves for each molecular weight under different convection speeds are shown in Figure 3-14. The fluorescent intensity was normalised as the fraction of the initial intensity and plotted for the first 20 minutes of the recovery period. The data shown are the mean values from the three individual experimental replications and the ribbons around the lines show the 95% confidence intervals.

When there is no convection (0 $\mu m\ s^{-1}$ Figure 3-14), FRAP in FITC-dextran 70 kDa resulted in the slowest fluorescence recovery and 4 kDa dextran recovered for the fastest. As the convection speed increased, the difference in fluorescence recovery times reduces between the three

molecular weights and the overall recovery speed increases drastically. 4 kDa and 10 kDa FITC-dextran showed more similar results as they are relatively smaller molecules compared to 70 kDa samples which always showed a slower recovery of the former two at every convective condition. When the convection speed reached 20 µm s^{-1}, fluorescence loss due to photo-bleaching recovered almost instantly for all the three molecular weights.

To further characterise the increase of fluorescence recovery when a controlled convective flow was introduced, the half time of the fluorescence recovery for each molecular weight under each convective conditions were calculated, showing in Figure 3-15. FITC-dextran 70 kDa has the longest half recovery time when there is little convection flow, followed by 10 kDa. As convection flow increases, the half time of the fluorescence recovery reduces drastically. When the convection is greater than 10 µm s^{-1}, the half recovery times for the three molecular weights converge together.

In this controlled convective system, the speed of fluorescence recovery shows dependency on both the molecular weight and the convection speed. Therefore, it is further proved that the fibre-optic photometry system is functioning according to the physics theories. From the recovery curves and the fluorescence half recovery time, it is shown that the photometry system was able to detect changes in fluid flow as little as 0.5-1 µm s^{-1}. Since a controlled convection was introduced in these conditions, the influx of the unbleached dye to the bleached volume is no longer diffusive. Therefore, the assumptions for Equation [2] are not being met. Therefore, these curves shall not be fitted with the diffusion model to estimate a diffusion coefficient as it would be done in a static brain phantom gel or *in vivo*. It is possibly true that an effective diffusion coefficient can be estimated from these curves, but due to the complexity of its mathematical modelling, it was not successfully determined in the current study. Nonetheless, the attempt to test the system in a controlled convection was a success, therefore, *in vivo* experiment would be carried out to estimate the diffusion coefficients in the brain parenchyma.

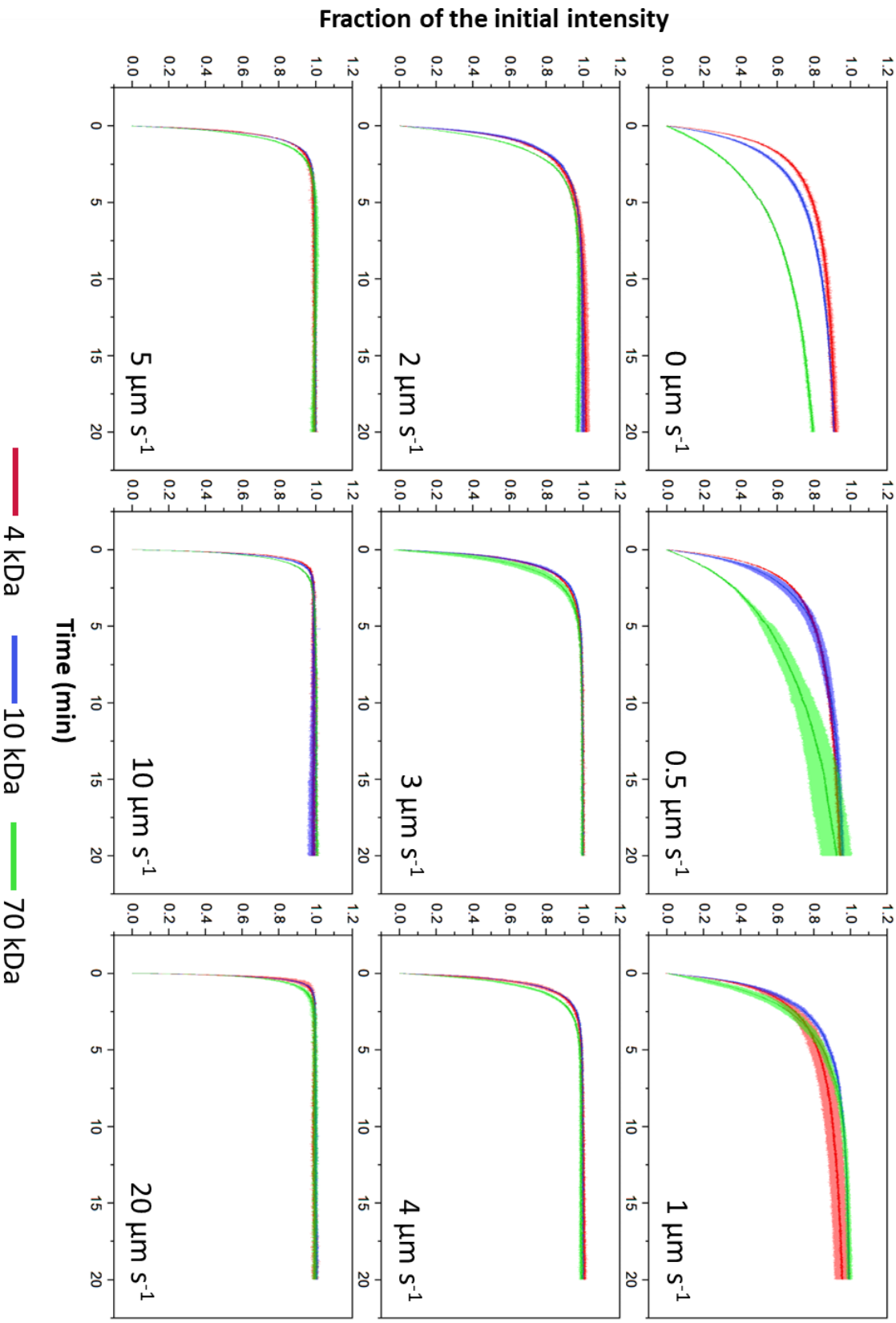
Fraction of the initial intensity
0 µm s-1
0.5 µm s-1
1 µm s-1
2 µm s-1
3 µm s-1
4 µm s-1
5 µm s-1
10 µm s-1
20 µm s-1
Time (min)
4 kDa
10 kDa
70 kDa

Figure 3-14 Photo-bleaching and fluorescence recovery curves recorded in controlled convective environments. FITC-dextran solutions of different molecular weights were pushed at different convective speeds through a Sepharose gel column where photo-bleaching and recovery was carried out. The figure shows recovery curves recorded by the fibre-optic photometry system. Fluorescence intensity was normalised as the fraction of the initial intensity prior to photo-bleaching. Y axis for each individual graph shows fraction of the initial intensity and X axis shows the time of the fluorescence recovery in minutes. Three experimental repeats were carried out for each molecular weight and convective speed (n=3). The lines showing are the means of the three experimental repeats and the coloured ribbons around the lines are 95% confidence interval of the data.

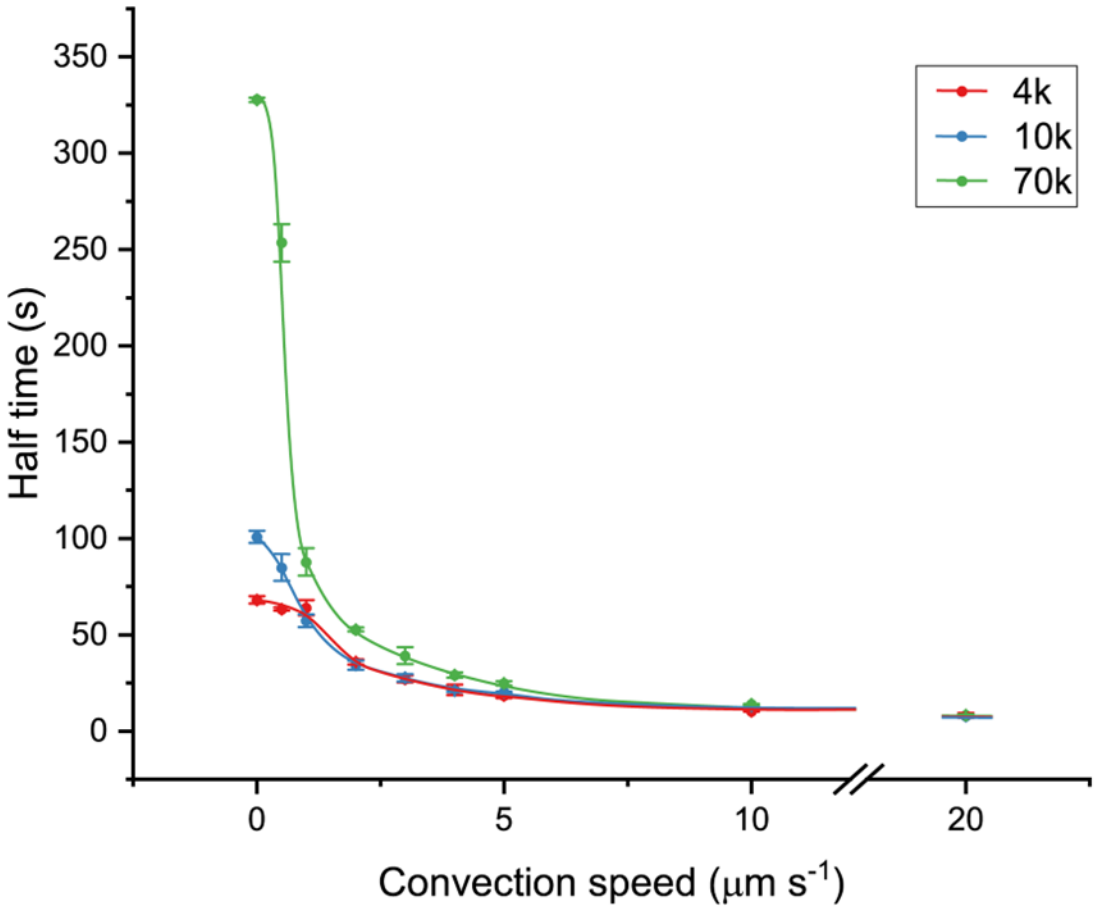

Figure 3-15 The half recovery times for each FITC-dextran molecular weight under different convection speed of the solution. The time taken for the fluorescence to be recovered to 50% of the intensity level prior to bleaching was calculated for each molecular weight of FITC-dextran under different convection flow rates. The graph shows a mean of three experimental repeats (n=3) with error bars indicating standard error of the mean. The coloured lines are showing the trend in changes in the mean half recovery times and are not mathematical curve fittings of the data.

3.6 Conclusion

In this chapter, the results of *in vitro* experiments validated the mathematical models, justified the experimental designs, and helped to optimise the photo-bleaching and recovery protocols. FITC-dextran was proved to be a suitable tracer to be injected into the brain. Under physiological pH conditions, FITC-dextran shows fluorescence when excited by 495 nm lights and was photo-bleachable without chemical recovery. Its fluorescence is proportional to its concentration. Using freshly sliced brain sections, the σ value was determined to be 134.3 μm, which will be used for all in *vivo* diffusion measurements. Compared and contrasted with a direct measurement of D, it is confirmed that the current methods, equipment set-up, and protocols were able to accurately measure diffusion coefficients. A controlled convection experiment also demonstrated the validity of the method. Having confirmed the method, *in vivo* experiments were to be carried out to estimate diffusion in the mouse brain.

Chapter 4 *In vivo* Experiment Results

In the previous chapter, the FRAP method with a fibre-optic photometry system was validated with *in vitro* experiment. In this chapter, the results from *in vivo* experiments are presented. Photometry and histology results suggest that fluorescence can be detected in the brain after the infusion of FITC-dextran. Diffusion coefficients measured in the brain parenchyma shows the final results of the current study which answers the question: does brain diffusion in the frontal cortex change during sleep?

4.1 Fluorescence was detected in the frontal cortex after injection

When the injection cannula was implanted in the caudate putamen and the optical fibre was implanted in the frontal cortex of mouse brain, fluorescence started to be detectable in the frontal cortex at some time after the start of the injection.

4.1.1 Fluorescence peaked around 6 hours post-injection

The blue tracer in Figure 4-1 shows an example of the fluorescence intensity detected by the photometry system through the optical fibre implanted in the frontal cortex of the left hemisphere. FITC-dextran (4 kDa) was infused via the injection cannula in the caudate putamen of the left hemisphere. Infusion started at $t = 0$ and lasted for 100 minutes. As it is shown, no fluorescence excited at 465 nm and emitted at 500-540 nm was detected at $t = 0$, indicating that there is a little autofluorescence in the frontal cortex within this specific excitation/emission range. Therefore, any subsequent detection of fluorescent signal by the photometry was resulted from the FITC-dextran dye injected. After a delay about 1.8 hours, fluorescent signal started to be detectable in the frontal cortex and increased rapidly. At around 6 hours after the start of the injection, fluorescence reaches its peak and started to decline gradually. This pattern of fluorescence intensity increase followed by gradual reduction was observed consistently across animals underwent the same experiment.

4.1.2 The spread of the dye can be predicted by diffusion

The physical distance between the position of dye injection and the position of fluorescence detection can be calculated from the coordinates of the two implantations: (-2.55, -0.58, -3.00), (-1.00, 2.22, -2.00) relative to Bregma in mm (M.L., A.P., D.V.) respectively. This gives a direct distance of 3350 µm between the point of source and point of detection. If the fluorescence intensity is a true representative of the concentration of FITC-dextran dye spread into the frontal cortex from a source in the caudate putamen, the course of three-dimensional spreading can be predicted by $M(t, r)$, where the concentration of the fluorescent dye is described as a function of time t and distance r from the source. Described by Carslaw (1906), this can be expressed as:

$$\boldsymbol{M(t,r) = \frac{Q}{(4\pi Dt)^{3/2}} exp\left[-\frac{r^2}{4Dt}\right]},$$

Equation [6]

where Q is the number of moles deposited at the source and D is the diffusion coefficient. The red dashed line in Figure 4-1 is a least-square fit to the experimental data (blue tracer) by Equation [6], using a value for r of 3350 µm and a value for D of 80 $\mu m^2\ s^{-1}$.

This result shows that the spread of FITC-dextran from its source in a posterior compartment of the brain to an anterior compartment of the brain was able to be characterised solely by diffusion. The assumption was that when diffusing, the dye can evenly distribute across the all the structural compartments of the brain and the dye spread to all directions at the same velocity. However, this is not the case, as observed histologically (Section 4.2), the dye did not spread evenly but followed specific brain structures.

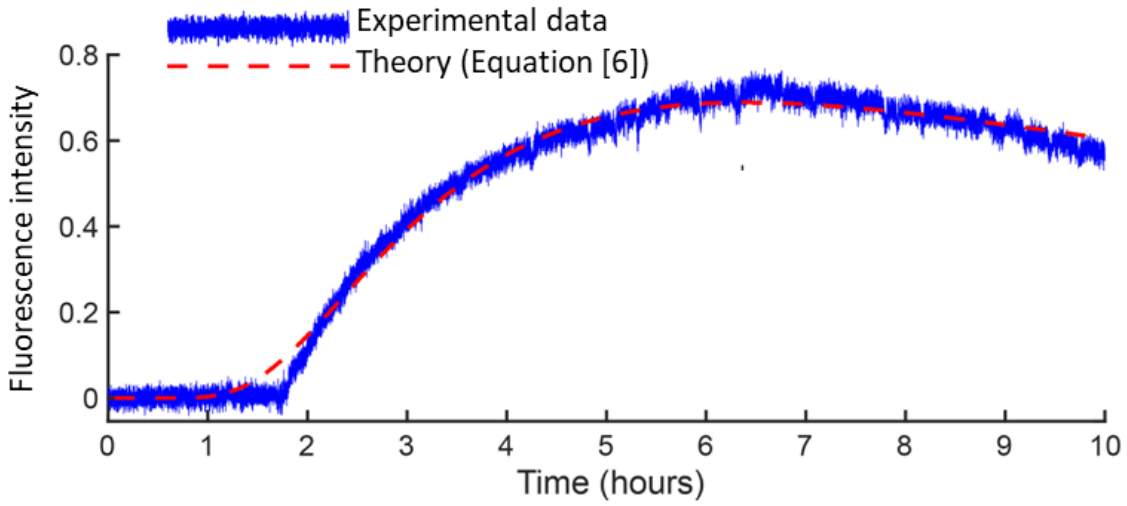

Figure 4-1 Fluorescence intensity detected via the optical fibre implanted in the frontal cortex of the brain after the start of FITC-dextran infusion. Optical fibre was implanted in the frontal cortex of the brain while an injection cannula was implanted in the caudate putamen. Photometry recording started when the infusion of FITC-dextran 4 kDa started. The dye was infused at a rate of 0.1 µl per minute. 10 µl was infused over 100 minutes. Blue tracer shows the fluorescence intensity recorded by the photometry system via the optical fibre. Red dotted line represents the theoretical prediction of Equation [6] when the concentration of fluorescent tracer is monitored at a distance to an instantaneous point source, and the spreading pattern of the molecule is diffusive.

4.1.3 Fluorescence reduces slowly after reaching the peak

After the fluorescence intensity in the frontal cortex reached its peak at approximately 6 hours after the start of infusion, it decreases slowly. It was calculated that the total level of fluorescence detectable in the frontal cortex decreased at a rate approximately by 6% hourly and remained above the baseline for at least 24 hours (estimated over the average of 18 mice).

This provides the opportunity for the method of photo-bleaching and recovery to function properly, since the method assumes the fluorescence intensity eventually recovers back to the level as same as the level prior to photo-bleaching. This also provides a time window of at least 24 hours per each injection to allow multiple measurements to be made at different time of day.

4.2 Spread of FITC-dextran was observed histologically

To observe the spread of FITC-dextran dye, mice were killed and have brain taken out by dissection at certain time after injection. Brains were snap frozen with cold liquid pentane to avoid movement of the dye post-dissection. Coronal sections were obtained by sectioning with a cryostat. Section remained frozen until mounted on a microscopy slide to avoid any additional movements. Whole sections were imaged, showing in Figure 4.2.

2 hours after the start of FITC-dextran in the caudate putamen, tracer started to spread out from the site of the infusion at the posterior part of the brain. At the site of infusion, tracer found to be concentrated at the immediate adjacent tissue of the implanted cannula. Tracer also distributed along the white matters of the lateral corpus callosum. Tracer concentrated in the side of hemisphere of cannula implantation, although some tracer distributed to the opposite side along the white matters. Limited amount of tracer was found at the anterior ventral part of the brain. The tracer continued to distribute out in a similar fashion during 4 to 6 hours after the start of the infusion. Consistent with the photometry data, tracer distributed more evenly at 6 hours after infusion. High level of fluorescence was found at the anterior part of the brain where the optical fibre was implanted. This even distribution of the dye provide an acceptable baseline fluorescence level for FRAP to function properly. Due to time limit of the current study, only One mouse was examined per one time point.

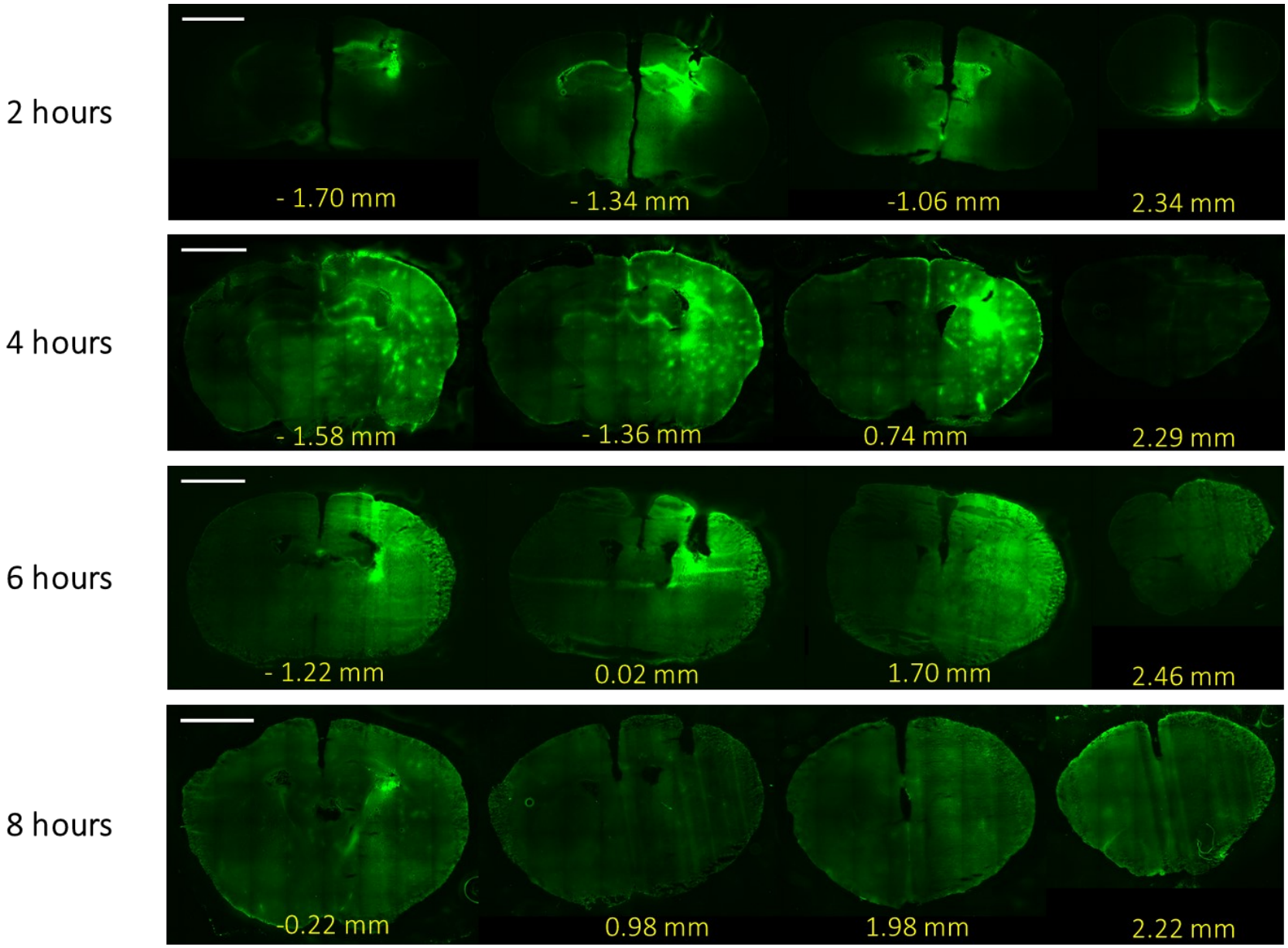
2 hours
- 1.70 mm
- 1.34 mm
-1.06 mm
2.34 mm
4 hours
- 1.58 mm
- 1.36 mm
0.74 mm
2.29 mm
6 hours
- 1.22 mm
0.02 mm
1.70 mm
2.46 mm
8 hours
-0.22 mm
0.98 mm
1.98 mm
2.22 mm

Figure 4-2 Spared of FITC-dextran (4 kDa) in the brain. After 2h, 4h, 6h and 8h of the start of the infusion, coronal section of the brain was sliced at 30 µm thickness with a cryostat machine. Tissue was unfixed. Cannula has been implanted in the caudate putamen of the left hemisphere at M.L. -2.55 mm, A.P. -0.58 mm, D.V. -3.00 mm. Optical fibre was implanted in the frontal cortex of the left hemisphere at M.L. -1.00 mm, A.P. 2.22 mm, D.V. -2.00 mm. All the cordinates are all relative to Bregma. Distance shown in the images are A.P. distance relative to Bregma. Scale bar: 2.5 mm.

4.3 Analysis of EEG, EMG and photometry data

The current study investigates fluid movements within the brain parenchyma when the animal was under different vigilance states and being sedated. To answer this question, three aspects of *in vivo* data were collected: a diffusion coefficient was estimated from the fluorescent recovery curve from the photometry data and the vigilance state was monitored by EEG and EMG recordings collected from the Neurologger. The three data were collected simultaneously and analysed in parallel.

4.3.1 EEG, EMG and photometry data were temporarily aligned

Figure 4-3A shows 10-hour recording of a typical aligned EEG, EMG, and photometry data of an *in vivo* experiment. First line show the filtered EEG data collected by the Neurologger. The EEG data was filtered with a high-pass filter to reduce noise and to increase signal to noise ratio. There is also a sonogram of the filtered EEG data on the second line, highlighting the dramatic changes in its frequencies during the recording period. The third line show filtered EMG data collected by the Neurologger. The raw EMG data was filtered by a band-pass filter between 1-50 Hz to reduce the noise level. Delta band and theta band of the EEG data were filtered out at 1-4 Hz and 5-10 Hz, respectively and the ratio between theta and delta were calculated (third to fifth lines of Figure 4-3A).

Blue tracer in the lower panel of Figure 4-3A shows 10 hours of photometry data, starting from 6 hours after the start of FITC-dextran infusion, when the baseline fluorescence intensity has entered the steady declining phase. This photometry data has been aligned with the above EEG

and EMG recordings. A 30-second photo-bleaching was initiated every hour, followed by a fluorescence recovery. During the 30 seconds of photo-bleaching, the photo-receiver of the photometry system was saturated, showing as a dropping to baseline in the fluorescence intensity. During the period of recording, animal was allowed to behave freely in its own cage, and the movement of the animal causes movements in the optical cable and optical connections between components. Such movements may interfere with the photometry signal recorded, causing more noise and sometimes glitches in the recording and creates artefactual changes in the recovery curves. These recording artifacts explain the imperfections in the smoothness of the recovery curves. Nonetheless, the overall good signal to noise ratio ensures good fittings of the recovery curves therefore accurate estimations of the effective diffusion coefficients.

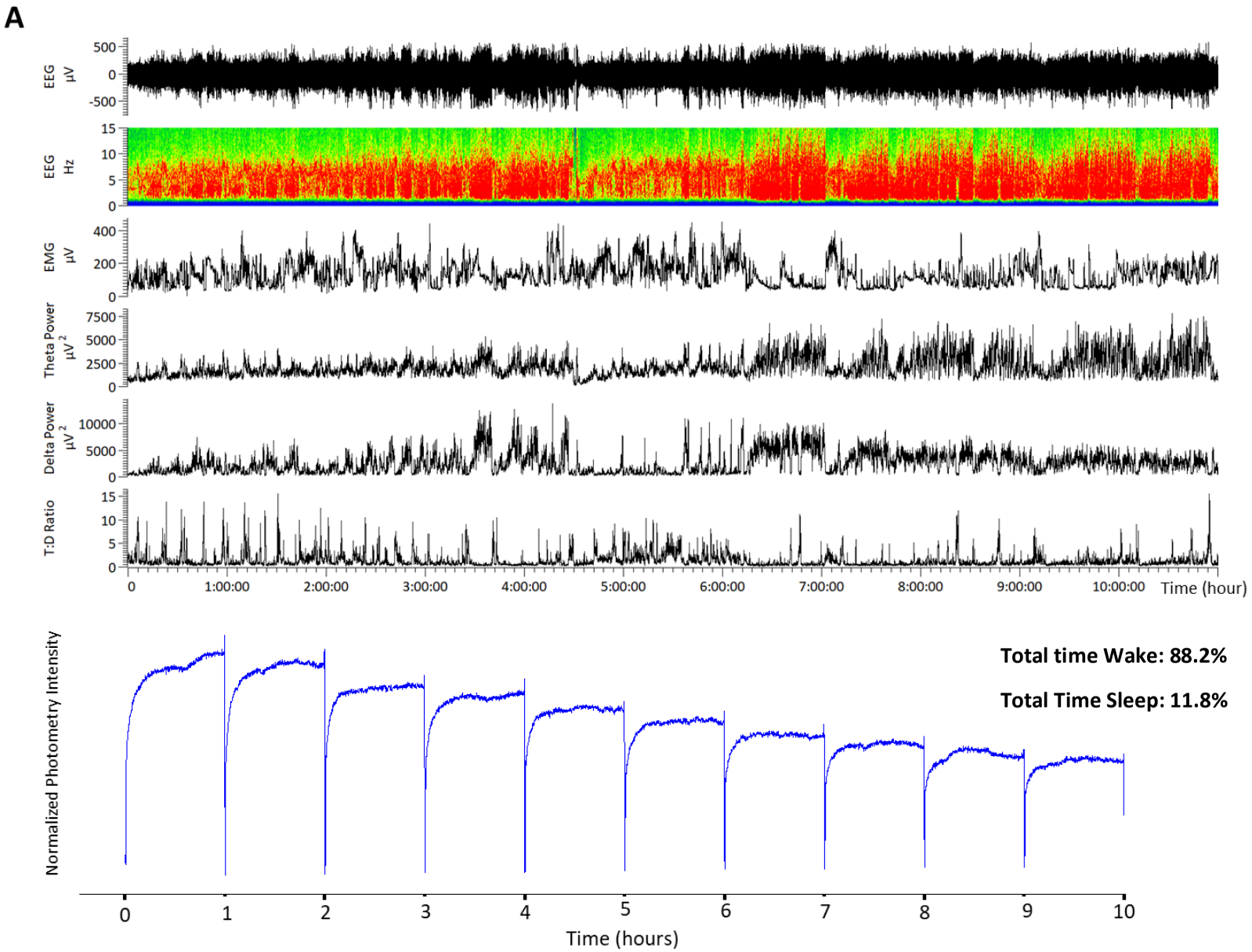
A
EEG µV
500
0
-500
EEG Hz
15
10
5
0
EMG µV
400
200
0
Theta Power µV²
7500
5000
2500
0
Delta Power µV²
10000
5000
0
T:D Ratio
15
10
5
0
0
1:00:00
2:00:00
3:00:00
4:00:00
5:00:00
6:00:00
7:00:00
8:00:00
9:00:00
10:00:00
Time (hour)
Normalized Photometry Intensity
Total time Wake: 88.2%
Total Time Sleep: 11.8%
0
1
2
3
4
5
6
7
8
9
10
Time (hours)

Figure 4-3

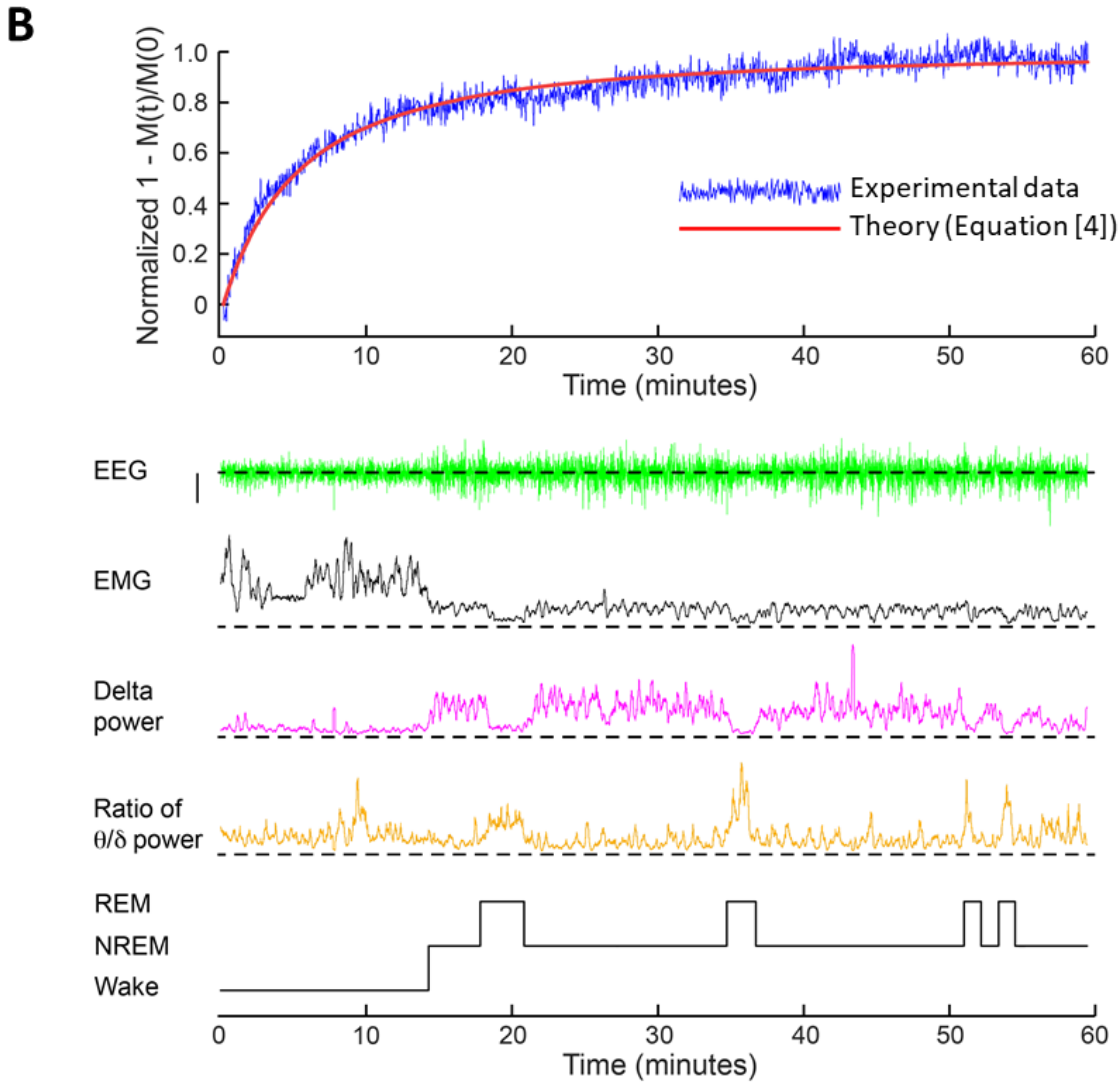

Figure 4-3

Figure 4-3 An example of EEG, EMG and photometry data collected for *in vivo* diffusion measurements. Photometry data were recorded in mice to obtain photo-bleaching and fluorescence recovery curves. The fluorescence recovery curves were used to estimate diffusion coefficient during each hour of recording. EEG and EMG data were collected by the device Neurologger and analysed to assess the vigilance state of the animal. **A**: 10 hours of continuous EEG, and EMG and photometry recording for one animal, starting from 6 hours after the start of the FITC-dextran (4 kDa) infusion, when the baseline entered the steady decrease phase. Data

shows EEG sonogram filtered EEG data with high-pass filter (0.5 Hz, -3 dB), filtered EMG data with band-pass filter (1-50 Hz (-3 dB)), theta to delta power band radio, the power of theta bands of the EEG frequencies (5-10 Hz), and the power of delta band of the EEG frequencies (5-10 Hz). Raw EEG and EMG data have the same sampling rate of 200 Hz. Photometry: 10 hour of photometry recording showing the normalised relative fluorescence intensity data temporally aligned the EEG and EMG data shown above. Photometry data has a sampling rate of 3.72 Hz. Data was smoothed with a moving average over 100 points. **B**: Photometry, EEG and EMG recording for one individual fluorescence recovery curve over 1 hour time. Blue tracer shows $1 - M(t)/M(0)$ of the normalised fluorescence intensity, according to Equation [3] of Section 2.1. Red line shows the curve fitting base on Equation [4]. Filtered EEG, filtered EMG, delta power, T/D ratio and sleep stages determined by the customise analytical script were also shown. All data shown within the hour are temporally aligned.

4.3.2 Recovery curves were fitted, and vigilance states were determined automatically

A MATLAB script was developed to analyse the data automatically. The two main functions of this script were to estimate diffusion coefficients by fitting the fluorescence recovery curves and determining the vigilance states of the animal.

The input of the script requires the followings: (a) the photometry recording of the whole experiment, starting from $t = 0$; (b) raw EEG and EMG recording data starting from $t = 0$; (c) zeitgeber time of the day when the recording was started. Firstly, the script identifies the time of bleaching and temporally align the EEG, EMG and photometry data. Then, it identifies each photo-bleaching events and calculates the baseline intensity $I(\infty)$ for each recovery curve by averaging the intensity over one minute prior to photo-bleaching (also see Figure 2-1). Then, it uses this and the intensity immediately after photo-bleaching $I(0)$ to normalise the recovery curves and calculate $M(t)$ according to Equation [3]. Then, a curve fitting is performed for each recovery curves according to Equation [4] and a value of D is obtained for each recovery curve. This shows that fluorescence recovery curve detected in the frontal cortex can be well fitted with the mathematical model proposed for diffusion.

Meanwhile, the determination of vigilance state based on EEG and EMG data is referred to as sleep scoring. One example of automatic sleep scoring of the script is shown in Figure 4-3B. The script automatically filters EEG data into theta and delta frequency bands and calculate the theta to delta ratio (T/D ratio). In combination with EMG data, the script utilises a probability-based algorithm to score sleep stages (details see Experimental Design Section 2.8.4). This automatic sleep scoring algorithm has been validated by comparing its accuracy with manual scoring conducted by three human expert scorers (five 24-hour recordings from each human scorer). The automatic script demonstrated higher than 90% sensitivity and specificity against all three scorers (data not shown).

The vigilance states of the animal are classified in three categories: Wake, NREM and REM. When there is a high level of EMG, it indicates that the animal is physically moving, thus being awake.

In principle, when the animal is awake, there is high EMG level, low delta power; when the animal is under NREM sleep, there is a high delta power, low EMG level and low T/D ratio; and when the animal undergoes brief REM episodes, there is a low EMG level, low delta power but T/D ratio spikes up. The script uses these principles and the probability-based algorithm to determine sleep stages automatically. Note that mouse sleep in relatively shorter episodes compared to humans: during the one-hour fluorescence recovery, the mouse may switch between the three vigilance states for many times, as seen in Figure 2-3B.

The script is able to automatically output a data table containing: the fitted D value ($\mu m^2 s^{-1}$), percentages of time the animal spent in Wake, NREM sleep, and REM sleep in each hour, zeitgeber time of the day when each photo-bleaching and recovery occurs as well other useful information. The script also presents and saves the curve fitting graphs automatically for manual inspections.

4.4 Relating diffusion coefficients with vigilance states

By analysing all *in vivo* data in the approach as described above, one D value is calculated from each fluorescence recovery curve during one hour of recording when the total duration of experiment is sleep scored. For each one hour of the fluorescence recovery curve, the total duration of time when the animal spent in Wake, NREM and REM was calculated and expressed as a fraction of one hour. In such way, the percentage of time that the animal spent under wake, NREM or REM during one fluorescence recovery curve was related to the D value calculated for that fluorescence recovery curve. For recordings that the animal was under the effect of a sedative drug, no sleep scoring was carried out.

Due to the fact that when not sedated the animal is free moving, it is impossible to keep the mouse to stay voluntarily in only one vigilance state voluntarily during the total duration of one fluorescence recovery. Diffusion coefficients calculated for each hour of fluorescence recovery were related to the vigilance state of the animal as the percentage of time the animal spent in each vigilance state during that hour. Therefore, each D value was related to three parameters: percentage wake hourly, percentage NREM hourly, and percentage REM hourly. Because the

mice typically spend less than 10% of their time in REM sleep, in the current study, REM and NREM sleep were considered collectively as sleep. Therefore, the comparisons were only made focusing on the potential change of diffusion coefficients between percentage of wake and percentage of sleep.

4.5 Diffusion was unchanged with percentage wake or sedation

The percentage of time during which the animal spent awake during a given specific hour of recovery curve is referred to as percentage wake. For each D value fitted, there is a corresponding percentage wake value for the specific hour. There are in total of 249 fluorescence recovery recordings fitted for D within 18 mice. Each animal underwent injection and recording experiments for a maximal of three rounds. The fitted D values from these 249 curves for each animal are shown in figure 4-4. These data were colour-grouped for different percentage wake: 0-25% wake, 25-50% wake, 50-75% wake and 75-100% wake.

As it is shown in Figure 4-4, the fitted D values lay between 0 to 100 $\mu m^2\ s^{-1}$ with a mean value of 34.9 $\mu m^2\ s^{-1}$ and median value 31.7 $\mu m^2\ s^{-1}$. Within each animal, fitted D values do not show any correlation against the four percentage sleep categories. Overall, there is no obvious difference between mouse nor difference between percentage wake categories within each mouse. Then the average D values for each percentage sleep category within each individual mouse was calculated and compared, shown in Figure 4-5. Each data point represents an averaged D value of one individual mouse when the mouse spent the specific percentage of time in wakefulness. Therefore. the n number here indicates the number of mice having data points fell into that percentage wake category. Fitted D values for animals sedated with Dexmedetomidine (DEX) was also added for comparison. The normality of the data has been tested with a Kolmogorov-Smirnov test with *p*-values of 0.64, 0.78, 0.92, 0.94 and 0.91 for the four percentage wake categories and the DEX group respectively. One-way ANOVA test shows that diffusion was unchanged for different percentages of wake or sedated with dexmedetomidine, ($F(4,55) = 0.90$, $p = 0.47$).

This result suggests that whether the mouse spent predominantly in awake or asleep, the movement of FITC-dextran tracer in the frontal cortex stays unchanged, and it is not affected by dexmedetomidine sedation.

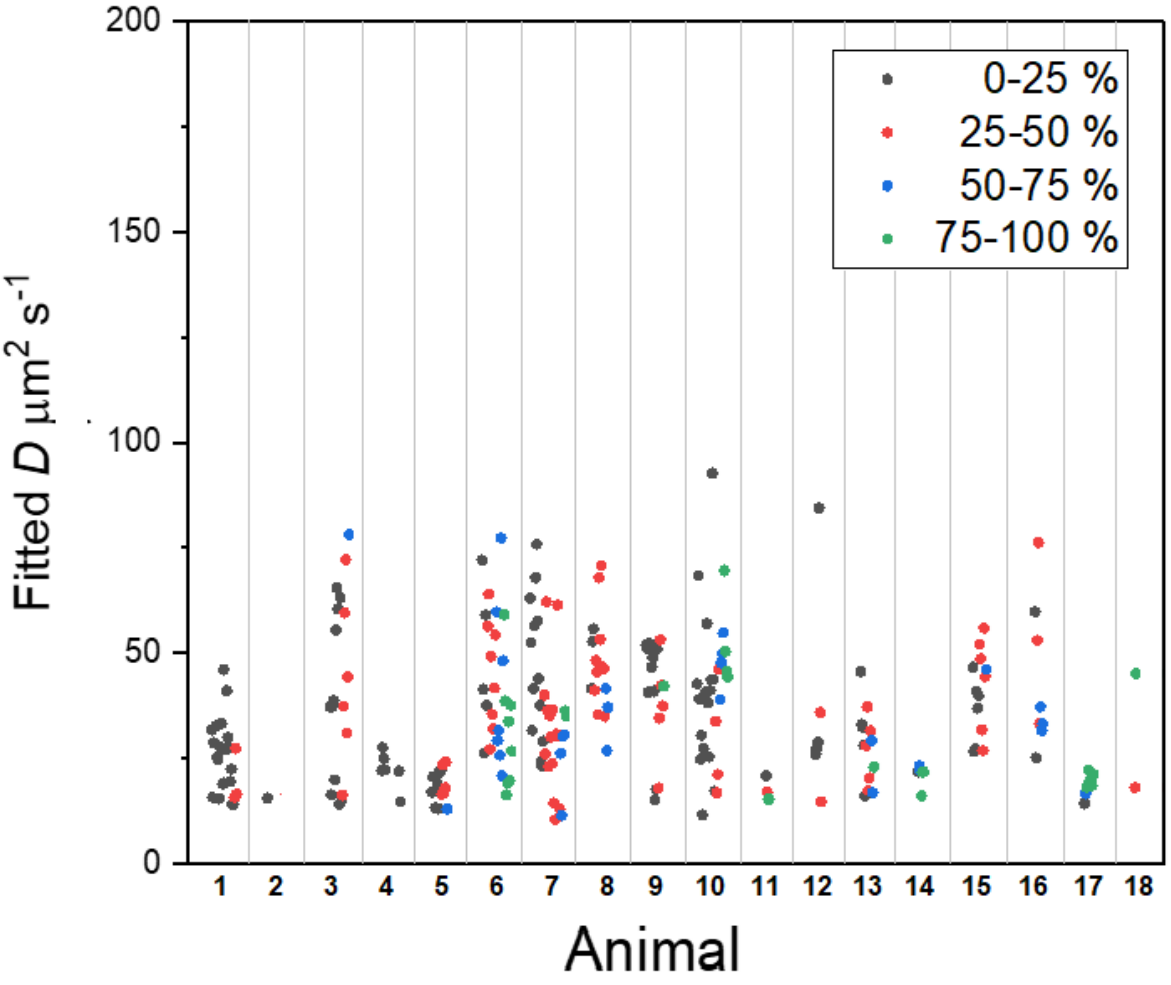

Figure 4-4 Fitted D values of recovery curves in each of the 18 individual animals shown in different percentage of wakefulness. All fluorescence recovery curves were fitted with a D value to estimate diffusion, at the same time the percentage of time the animal spend in wakefulness during that hour of fluorescence recovery was also estimated by the customise analytical script from the automatic sleep scoring algorithm. In total, 249 measurements were made in 18 mice.

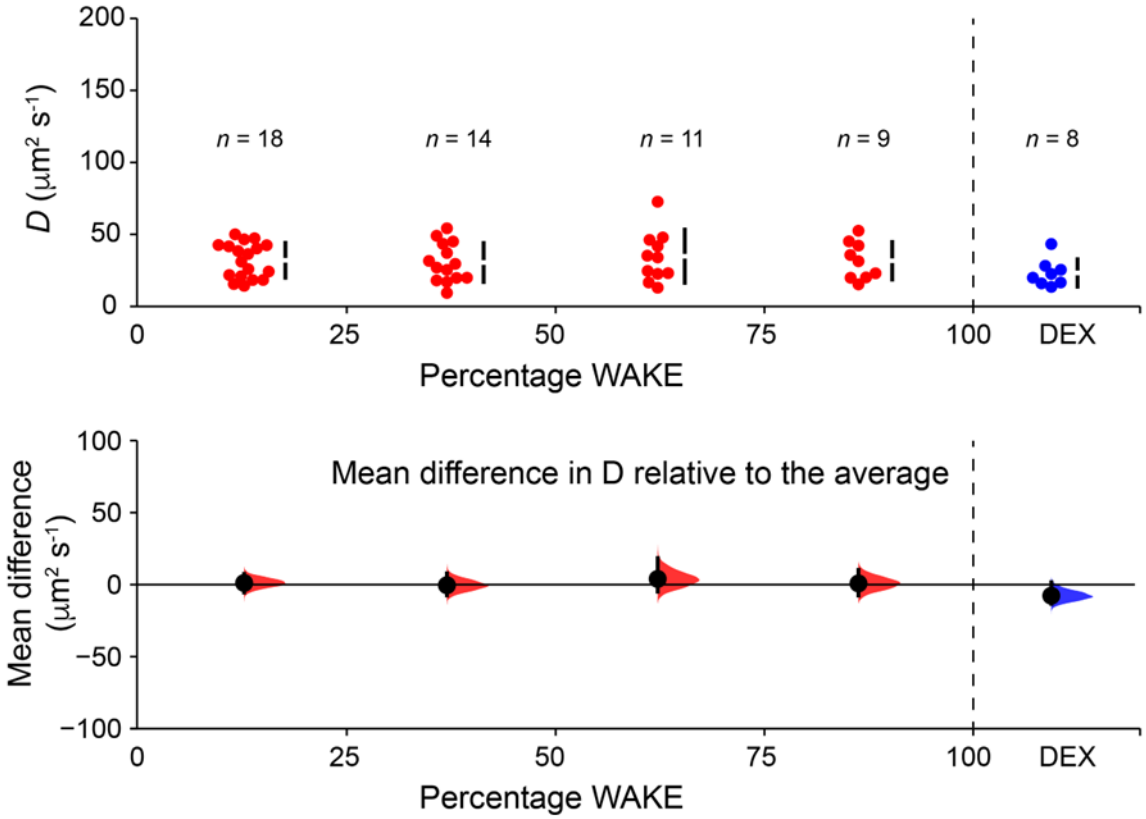

Figure 4-5 Mean fitted D values of each individual mouse compared between different percentage of sleep and sedation. The mean D values were calculated for each individual mouse within the same range of percentage wake. D values were also fitted when the animal was sedated with dexmedetomidine when no sleep scoring and percentage wake were calculated. **Upper panel** compares the mean of D values averaged over each individual mice with vertical bars next to the data points indicating 95% confidence interval of the data and the gap between the bars indicates the mean of the data set. **Lower panel** shows the difference between each percentage wake groups with the 95% confidence interval (the vertical bar) and the resampling distributions of the data using a bias-corrected and accelerated bootstrapping method (Ho *et al.*, 2019). Figure was generated with estimationstats.com.

4.6 Diffusion was unchanged with zeitgeber time

The time of the day when each *in vivo* measurement was made was also recorded. This was converted to zeitgeber time according to the day-night cycle of the animal husbandry schedule. The fitted D values of each individual mouse are shown in Figure 4-6, grouped by the zeitgeber time when each measurement was made. Within each animal, fitted D values do not show close correlation against different zeitgeber times. This suggests that the variation within each individual animal is random, therefore mean D values for each mouse during six zeitgeber time group were calculated. During the experiments, animal experienced Lights-ON during Zeitgeber time 0-12 hours and Lights-OFF during zeitgeber time 12-24 hours. Mice are nocturnal and therefore more active during the light-OFF period. The mean D values were compared across the six zeitgeber time groups (Figure 4-7). Normality of the data was tested with a Kolmogorov-Smirnov test with p values of 0.97, 0.63, <n=5, 0.58, 0.83 and 0.72 for each of the groups. One-way ANOVA test shows that diffusion was unchanged for different zeitgeber time groups, ($F(5,64) = 0.88$, $p = 0.50$).

This result suggests that the movement of FITC-dextran tracer in the frontal cortex stays unchanged during the day-night cycle.

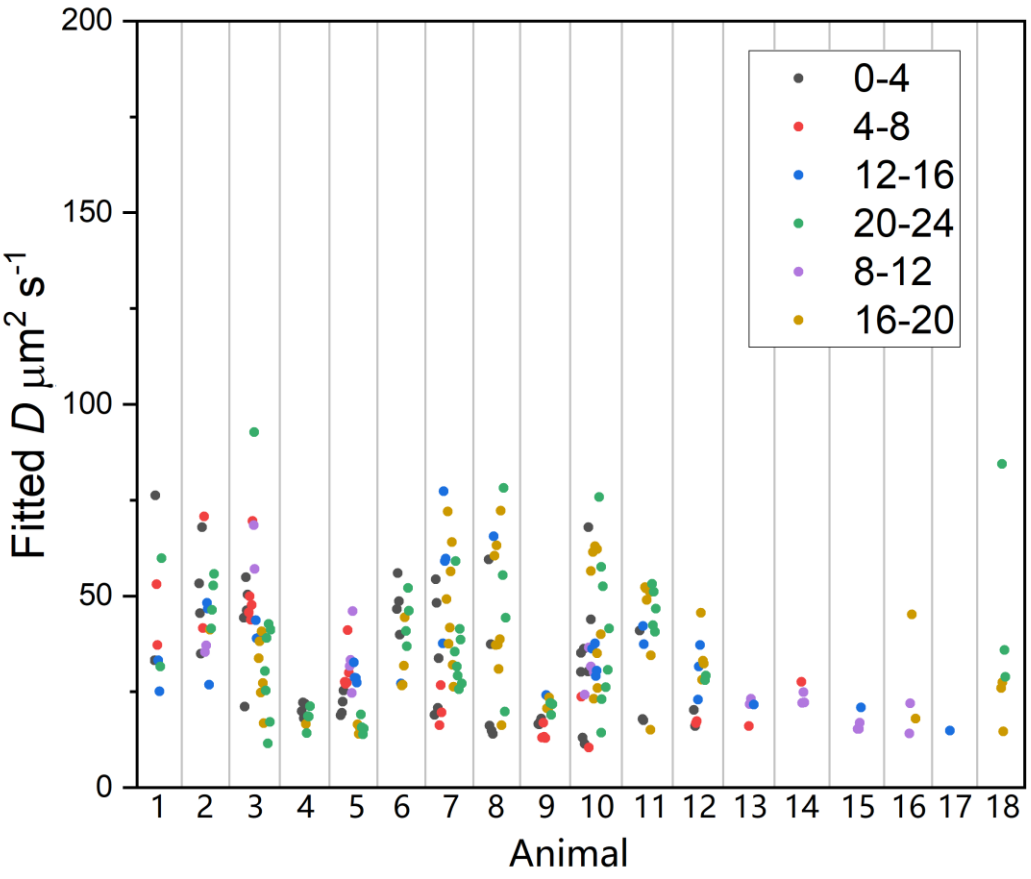

Figure 4-6 Fitted D values of recovery curves in each individual animal shown in six zeitgeber time groups. All fluorescence recovery curves were fitted with a D value to estimate diffusion, meanwhile the zeitgeber time at which the measurements were made were also recorded. The zeitgeber times when the recovery curves were recorded are grouped in five categories. In total, 249 measurements were made in 18 mice.

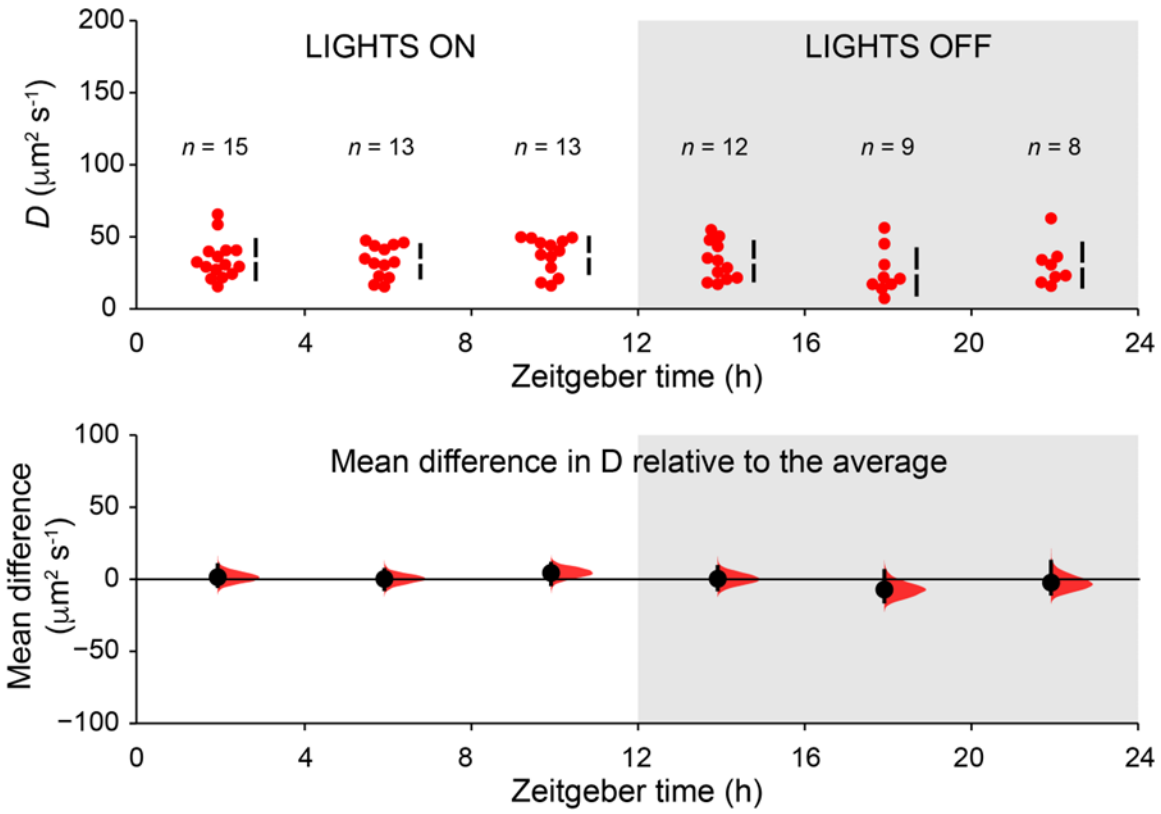

Figure 4-7 Mean fitted D values of each individual mouse compared between different zeitgeber time group. The mean D values were calculated for each individual animal for different zeitgeber time. Zeitgeber time 0-12 is when the lights have been turned on for the animals to stimulate day-time and lights were turned off to stimulate night-time between zeitgeber time 12-24. Note that mice are nocturnal and are more active during day-time. Upper panel compares the mean of D values averaged by each individual mice during different zeitgeber time group with vertical bars next to the data points indicating 95% confidence interval of the data and the gap between the bars indicates the mean of the data set. Lower panel shows the difference between each zeitgeber time groups with the 95% confidence interval (the vertical bar) and the resampling distributions of the data using a bias-corrected and accelerated bootstrapping method (Ho *et al.*, 2019). Figure was generated with estimationstats.com.

4.7 Conclusion

Fluorescent signal was detectable in the frontal cortex soon after the infusion of FITC-dextran in the caudate putamen started. The fluorescent intensity reached its peak around 6 hours after the start of the infusion, when there was a relatively even distribution of fluorescence in the frontal cortex. During the steady declining phase of the intensity, diffusion coefficients in the brain parenchyma were measured. The measured D values were correlated with the vigilance states of the animal in the form of percentage time spend in wakefulness or sleep. Based on the measured D values, it is concluded that diffusion in the parenchyma of the frontal cortex stays unchanged regardless of vigilance states, sedation by dexmedetomidine or the day-night cycle.

Chapter 5 Discussion

5.1 Summary of the results

Firstly, a mathematical model which allows an absolute number of diffusion coefficient, D, to be measured empirically was presented. This model works on the fluorescence recovery curve of the FRAP method with a three-dimensional condition co. It requires the data to be normalised between the fluorescent intensity prior to photo-bleaching $I(\infty)$ and immediately after photo-bleaching $I(0)$. Secondly, a fibre-optic photometry system was successfully established. With the use of the FITC-dextran dye (4 kDa, 10 kDa and 70 kDa), the system was able to effectively bleach a defined volume of a substrate and record the fluorescent recovery curve. Suitable protocols for effective bleaching and photometry recording were developed. And these system and protocols can be carried out on freely behaving mice.

Next, a series of *in vitro* experiments in gels and freshly cut brain sections were conducted to estimate the light distribution both in a phantom gel and in real brain tissues. This was to estimate the shape of the bleached volume at the tip of the optical fibre. This shape governs an important parameter σ when calculating the D from the mathematical model. σ values were successfully determined from taking images of the light distribution. Then an independent method of direct measurement of D *in vitro* was designed and carried out to measure the D of dextran 4 kDa, 10 kDa and 70 kDa in aqueous substrates. Then the photometry system was used to measure D of 4 kDa, 10 kDa and 70 kDa FITC-dextran in brain phantom gels using the mathematical model and the estimated σ values. Combining these two results, diffusion coefficients in aqueous solution measured by the two methods on the same substance were compared. Similar D values were yielded from the two methods. This validated the FRAP by the fibre-optic photometry method.

Moving onto *in vivo* experiments, a miniature datalogger device was used to record real time EEG and EMG data in mice brain. EEG and EMG data were combined and analysed together with FRAP recovery curves obtained via photometry recording. A customise MATLAB script was developed to analyse these data automatically. Mice were implanted with the optical fibre in the brain

parenchyma of the frontal cortex where diffusion coefficients were measured hourly throughout different time of day when the animal was freely behaving. Measurements were also measured when the animal was sedated by dexmedetomidine. The final results showed that flow of FITC-dextran tracer in the mouse parenchyma of the frontal cortex can be characterised with diffusion and the rate of diffusion stays unchanged between sleep, wake, or sedation and is not affected by time of the day.

5.2 ISF flow: convection or diffusion?

Empirical evidence from the current study identified the diffusive movement of ISF in the brain parenchyma of the mouse frontal cortex which is comparable to the diffusing in an aqueous solution. The mean value for the diffusion coefficient D across all vigilance states was calculated to be 35 $\mu m^2\ s^{-1}$.

The tortuosity of the extracellular space characterises how tortuous the gaps between cells that would allow ISF solutes to navigate through, in another word, how complex is the curvatures of the gaps between each cell. Tortuosity affects diffusion, as characterised by Gifford, (1955):

$$\boldsymbol{D = {D_{aq}}/{\lambda^2}}$$

where D is the effective diffusion coefficient measured, D_{aq} is the diffusion coefficient in aqueous solution, and λ is the effective tortuosity. With our independent measurement of D_{aq} of FITC-dextran 4 kDa averaged at 133.93 $\mu m^2\ s^{-1}$ and corrected to 37°C using the Stokes-Einstein equation giving 202 $\mu m^2\ s^{-1}$ (Syková and Nicholson, 2008), the effective tortuosity is therefore calculated to be 2.4. In Xie *et al.* (2013) study, the tortuosity in the extracellular space was measured to be approximately 1.5-1.6, using the real-time iontophoretic method. This two values are highly comparable to each other. The small discrepancy between the two results can be due to the error in the methods used. Further experiments using different molecular sizes of the tracer should be carried out to obtain a more accurate estimation of λ during different vigilance states or under sedation.

The current study was the first study to directly quantify diffusion under different vigilance states of freely moving mice. Previous studies (Xie *et al.*, 2013) attempted to correlate glymphatic influx with delta EEG wave when the animal was fixed under a microscope. Although intensive habituation was carried out to acclimate the mice to sleep or behave normally under the microscopy, it is hard to believe that animal experimented with completely normal behaviour. In the current study, mice were left in their home cage with water and food provided and all which was synchronised with their normal zeitgeber conditions. Meanwhile, accurate sleep scoring was carried out to evaluate the precise vigilance state of the animal instead of calculating the percentage prevalence of delta wave. The experiments were also carried out at different time of the day, where circadian influence on ISF flow rates can be detected.

By many groups and studies, the glymphatic function was often measured by the influx of CSF from the perivascular space into the parenchyma. ISF movement within the brain parenchyma on the other hand was rarely investigated. Davson *et al.*, (1963) has proposed the idea that CSF acts as a sink for ISF solutes. Continuous production of CSF at the ventricle resulting in the dilution of solutes in the CSF solution which then creates a concentration gradient of solutes between CSF and ISF. This concentration gradient extends into the parenchyma adjacent to ventricle walls and the perivascular space. Concentration gradients within the parenchyma allow effective diffusion of solutes deeper inside the tissue to diffuse towards the perivascular space more effectively. According to Davson's hypothesis, metabolites within the ISF moves towards the CSF for removal by diffusion which was driven by a chemical gradient. This diffusive removal of ISF solutes can be explained by diffusive mechanism detected in the current study.

Existing evidence on the directions of CSF flow in the perivascular space is also convectional, but this bulk flow is likely to be restricted to the perivascular space, at least restricted to the parenchymal tissue immediately adjacent to the perivascular space. Our finding suggests that ISF in the parenchyma is predominantly diffusive, consistent with many previous findings. However, based on the histological mapping of tracer spear pattern across the brain, it is clear that when FITC-dextran is injected into the parenchyma, it spreads along the fibrous axons of the white matter such as the corpus callosum. These findings are consistent with the conclusions raised by Abbott (2004) from reviewing various previous studies. Combining the literature with the current

study, it is highly possible that the mode of solute transport in the brain parenchyma is combined result of both convection and diffusion modes, depending on the local compartmentalisation and anatomical arrangement. When considering long range circulations of ISF and its solutes, bulk flow along preferential routes can be the predominant mode of transport. But when considering local movements of solutes between periarterial space and perivenous space, diffusion is more likely to be the dominate mode of transport. Hence, the assumption of ISF bulk flow of the glymphatic hypothesis needs more elaboration and reconsideration. Nedergaard and her group in her recent response to the controversies (Mestre *et al*., 2020) pointed out that convection and diffusion may co-exist in the interstitium, and the dominant mode of movement may be heavily influenced by other factors such as intracranial pressure, body position, region of interest, respiration conditions and many more. She emphasised on the net outcome being a more relevant argument when considering the efficiency of brain clearance. However, in order to pharmacologically interfere with the brain clearance mechanism, studies on the flow of ISF is still necessary.

There are other issues to consider when trying to understand the movement of solutes within the brain interstitium. Solutes in the interstitial fluid of the parenchyma are not all toxic metabolic wastes. Many of the molecules especially the ones secreted and regulated by glial cells serves function as cell-cell communication mediators. Cell signalling molecules may utilise diffusion or the preferential convective channels as communication routes between brain regions distally apart. Better understanding on the flow pattern of ISF solutes provides new frontiers to study neuronal circuit and communication.

5.3 Limitations of the study

There are limitations in different steps of the study which can be improved in the future; alternative approaches are also proposed to refine the current experimental designs.

5.3.1 Invasiveness of the implantations

The invasiveness of the fibre-optic approach was relatively bigger than previously conducted experiments (Thiagarajah., 2006) where a glass micropipette was used for FRAP and photometry

measurements (less than 10 µm fibre tip compared to 200 µm). Excessive damage to the local tissue may result in change of the local vasculature structure and tissue integrity, leading to imprecise measurements of diffusion. A large volume of tissue lesion at the fibre tip can result in a pocket of ISF accumulation. If recorded from this ISF pocket, the diffusion rate would be incorrectly estimated. Using a smaller diameter optical fibre would be preferable if minimal damage is more desirable, see the next section.

Tissue distortion by cannula insertion in the striatum was also reported to significantly affect the diffusion of tracer at the site of injection (Chen *et al.*, 1999). However, in the current study, the location of cannula implant and the location of optical fibre is relatively far away from each other, and time was taken to allow the intracranial pressure to recover to normal before any recordings were made. Therefore, the influence of cannula implantation should have been minimised.

5.3.2 Size of the optical fibre

The size of the optical fibre may raise separate issues when measuring ISF diffusion in the parenchyma. In the current study, a 200-µm diameter optical fibre was placed in the tissue which contains densely packed vasculatures. Based on the sigma estimated from light distribution, the diameter of the cross-section of the photometry recording area was estimated to be around 300 µm. This distance can be much larger than the average distance between the blood vessels within the brain parenchyma (Rovainen *et al.*, 1993; Adams *et al.*, 2014; Hill *et al.*, 2015). In fact, in the current study, the recorded space may indeed include multiple blood vessels including both arterioles and venioles. According to the glymphatic hypothesis, ISF flow originates from the arterioles and drains into the venioles. Therefore, the measured effective diffusion coefficient at the fibre tip may have been resulted from both the influx and efflux at the perivascular spaces of these vessels. Such influx and efflux may cancel out each other, resulting in an apparent diffusive mode of solute transport.

To overcome this issue, a thinner optical fibre, for example 50 µm fibre can be used. When using a thinner optical fibre, the light delivered and received through the optical fibre is drastically reduced. This would result in a lowered signal intensity, smaller signal to noise ratio and consequently larger errors in diffusion measurements. To mitigate these challenges, the LED

intensity which supports the light of excitation can be increased accordingly, but not too strong to introduce bleaching during recording. Currently, the tip of the optical implantation is a flat-cut tip, which can be converted to a pointed or angled cut to further decrease the detection area. However, changing the shape of the optical tip will also result in the change of light distribution at the optical fibre tip, making it no longer follow a semi-hemispherical Gaussian distribution. Under such scenarios, light distribution should be re-captured, and the mathematical basis of the diffusion estimation should be adjusted accordingly.

5.3.3 Molecular sizes of the tracer

The hallmark of diffusion is its character of being size-dependent. In order to distinguish between diffusive movement and convective movement, different molecular weights of the FITC-dextran tracer can be used. FITC-dextran materials at 4 kDa, 10 kDa and 70 kDa can be injected in the brain parenchyma followed by fluorescent bleaching and recovery recording. This can be done separately or simultaneously using different sets of wavelength filters. Because of the huge gap in the molecular weights of these tracers, the differences in the estimated diffusion coefficients between these molecular weights can help to confirm the diffusive nature of the ISF solutes, in a similar approach to the size-dependent experiments carried out by Smith *et al.* (2017).

However, when injected tracers with heavier molecular weights, the time it takes for the fluorescence signal to recover to the baseline would be prolonged significantly. It would not be possible for the fluorescent signal to fully return to the baseline within one hour, if it fully recovers at all. Therefore, the assumption for the mathematical model that the baseline fluorescence stays constant is no longer true. Although, comparing between molecular weights can help to identify the mode of solute movement, injecting heavier molecular weights may not be useful if an absolute number of diffusion coefficient is to be estimated.

Due to the abovementioned considerations and the time limits of the current study, only 4 kDa FITC-dextran was used to estimate diffusion coefficient *in vivo.*

5.3.4 Data variation and sensitivity of the method

Another major limitation of the current study is the large variation of the *in vivo* results. Identical experiment setup and data analysis approach was used for both the *in vivo* and *in vitro*

experiments, however, large data variations were only fond in the *in vivo* results. One Possible reason for these large variations can be the large noise in the animal recordings due to the movements of the animal. When connecting the optical cable to the optical implants, the gap between the two device was relatively large and any movement of the mouse can further loosen the connection, resulting in glitches in the recorded fluorescence recovery curve. Such negative influence is even more significant towards the end of the recording hours when the baseline fluorescence level is relatively smaller. The curve fitting is less effective when fitting curves with large numbers of glitches.

When testing the photometry system, it was found that the fitted diffusion coefficient sometimes showed dependency on the level of bleach, *i.e*., how much of the baseline level fluorescence was able to be reduced by the 30 seconds of intense bleaching light. When further investigated, the extend of bleaching was relatively stable with occasional fluctuation, resulting in curves that were "over-bleached" and "under-bleached" that occurred randomly. Unstable connections between the devices in the light path like mentioned before between the cable and implants can partially explain such random events. If indeed the large variations in the estimated diffusion coefficient were result from the differences in bleaching efficiency, repeating the *in vivo* measurements should overcome this issue. Therefore, it would be helpful to reduce the data variation and enhance the reliability of the *in vivo* results by repeating the experiments with more animal *N* numbers to enhance the statistical power of the results.

5.3.5 Quantification of fragmented sleep

In mice, sleep is highly fragmented, and the animal may switch vigilance states in a matter of minutes before one fluorescent recovery curve can be completely recorded. Therefore, it is impossible to keep a freely moving mice to voluntarily stay in one vigilance state and correlate one diffusion measurement with one vigilance state alone. In the current study, vigilance state for each diffusion measurement was represented by percentage of sleep time within that hour of recording. This might not be the best way of presenting these data, as any sudden shifts in diffusion coefficient due to switching of vigilance state may become undetectable. The ideal solution is to develop a method which could be able to measure a diffusion coefficient within

minutes. One proposed alternative method with FRAP is to use a less intense light to bleach some concentration of the dye and followed by more intense light to completely bleach the dye. This would allow the percentage of the bleachable dye under that light intensity to be calculated. Under the same bleaching intensity, the percentage level of bleachable dye depends on how quickly the unbleached dye flows back into the bleached volume during the bleaching duration. A mathematical model can be developed to correlate percentage bleachable with diffusion coefficients. FRAP with this approach should be carried out with different molecular weights, and the percentage bleachable dye can be compared between these molecular weights to verify diffusion.

5.3.6 Other refinements

When injecting FITC-dextran into the caudate putamen, FITC-dextran should be dissolved in freshly prepared aCSF solution instead of saline solutions to minimise the impact to the local osmotic potentials. In the current study, mice aged from 3-7 months were used for *in vivo* measurements. As age might have a big effect on the glymphatic system, mice within more narrow age range should be used.

5.4 Future works

The current study has set the scope to investigate the mode of solute transport in the brain parenchyma. It showed that ISF solutes in the frontal cortex follows a diffusive movement pattern similar to a static gel environment. However, this observation stays on a local tissue level due to the lack of consideration of the fine vasculature system existing in the brain parenchyma. As elaborated in the previous sections, CSF influx at arterioles and ISF efflux at venioles could cancel out each other and contribute collectively to an apparent no-net-transport result. This does not help to directly evaluate the glymphatic hypothesis. Therefore, future experiments should focus on the clearance of injected brain tracer on a global scale, i.e., considering the collective clearing effect of the brain vasculature system on a system scale.

In fact, in the current study, shortly after the tracer FITC-dextran was injected in the brain, the fluorescence signal can be detected in the frontal cortex. And the total detectable signal intensity increases to its peak at around 5-6 hours post-injection and then slowly decline for the following

20+ hours. This declining of fluorescence intensity in the frontal cortex is a representation of the brain clearance effect and the rate of fluorescence lost implies the rate of brain clearance.

After the completion of the work described in this report, future works have already begun to investigate the global brain clearance effect by injecting a fluorescent tracer, Alexa Fluor 488 dye (AF488) into the caudate putamen and to observe the fluorescent intensity in the frontal cortex. AF488 is a smaller fluorescent molecule with a molecular weight around 650 Dalton which diffuses faster in the brain. This would help to reduce the overall time for recording. Some preliminary result already showed that the time for the fluorescent signal to peak in the frontal cortex significantly reduces when animals were sedated with DEX compared to normally behaving mice. Such results may indicate a less profound brain clearance effect in sedated animals as opposite to the glymphatic hypothesis.

In the current study, an optimised photometry system was successfully established to measure the local fluorescence level in freely moving mice. When injecting fluorescent tracer into the brain parenchyma, the loss of tracer from the brain can be directly measured as an indication of brain clearance. Instead of injecting into the cisternal magna and measuring clearance by observing CSF influx as it was done in most of the glymphatic-supporting experiments, the current method is more direct, intuitive and logically straightforward. There are also plans to bring the injection site and detection site closer to each other so the time course for the detectable fluorescence increases and decreases to be further shortened. This would allow sleep deprivation and recovery sleep to be introduced when the animal was forced to stay awake for several hours and then go into continuous sleep for another few hours. Therefore, the rate of brain clearance can be estimated when the animal is fully awake or fully asleep for the entire time of fluorescence recording. In such way, the effect of sleep on the rate of brain clearance can be determined.

Future experiments are to be carried out to determine the total amount of fluorescent tracer remained in the brain tissue by dissecting the brain out at different time points after injection when the animal is sleep deprived, continuously sleeping or being sedated. By homogenising the brain and measuring total fluorescence level, the clearance effect can be directly measured,

further confirming the effects of sleep and sedation. Preliminary results have already shown a significant reduction of total fluorescence lost at 5 hours after injection when animals were sedated with DEX compared to normally behaving animals.

To further extend the works and gather more evidence to evaluate the method for brain clearance, there are more variables and conditions to be considered, for example the age and sex of the animals to be used, the effect of AQP-4 on the tracer efflux. The effect on brain clearance of all such conditions can be evaluated using the model described in the current study.

5.5 Concluding remarks

In this study, a novel approach using FRAP and fibre-optic photometry was successfully developed and verified to measure absolute diffusion coefficients in freely behaving mice. When tested in the parenchyma of the frontal cortex in mice, the results indicated there is no change of fluid movement with different vigilance states, sedation by dexmedetomidine or time of the day. The results also suggest the solute transport mode locally to the frontal cortex is diffusive rather than convective. These results do not support the glymphatic hypothesis which claims a convective flow in the parenchyma that helps to clean brain toxins during sleep. Contrasting with existing evidence from the literatures, it is more likely that the mode of solute transport in the brain parenchyma is a combination of diffusive and convective movements. Since many factors can affect fluid movements in the brain, a better understanding of the regulation of ISF movement would provide insights to brain clearance.

Future works following the current study should focus on the overall clearing effect of the brain as a functional organ. By injecting fluorescent tracers into the brain parenchyma and monitoring the total loss of fluorescent signal following injection using the fibre-optic photometry system, the rates of brain clearance can be directly measured. The method and protocols successfully established in the current study provides new technology to observe and quantify this critical brain function, allowing neurophysiologists to further investigate the reasons for sleep. It also opens new perspectives for modulating brain clearance and tackling neurodegenerative diseases from different directions.

Chapter 6 Reference

Abbott, N.J., 2004. Evidence for bulk flow of brain interstitial fluid: significance for physiology and pathology. *Neurochemistry international*, *45*(4), pp.545-552.

Abbott, N.J., Pizzo, M.E., Preston, J.E., Janigro, D. and Thorne, R.G., 2018. The role of brain barriers in fluid movement in the CNS: is there a 'glymphatic'system?. *Acta neuropathologica*, *135*(3), pp.387-407.

Adamantidis, A.R., Gutierrez Herrera, C. and Gent, T.C., 2019. Oscillating circuitries in the sleeping brain. *Nature Reviews Neuroscience*, *20*(12), pp.746-762.

Adams, D.L., Piserchia, V., Economides, J.R. and Horton, J.C., 2015. Vascular supply of the cerebral cortex is specialized for cell layers but not columns. *Cerebral Cortex*, 25(10), pp.3673-3681.

Akeju, O., Hobbs, L.E., Gao, L., Burns, S.M., Pavone, K.J., Plummer, G.S., Walsh, E.C., Houle, T.T., Kim, S.E., Bianchi, M.T. and Ellenbogen, J.M., 2018. Dexmedetomidine promotes biomimetic non-rapid eye movement stage 3 sleep in humans: a pilot study. *Clinical Neurophysiology*, *129*(1), pp.69-78.

Alhola, P. and Polo-Kantola, P., 2007. Sleep deprivation: Impact on cognitive performance. *Neuropsychiatric disease and treatment*.

Anafi, R.C., Kayser, M.S. and Raizen, D.M., 2019. Exploring phylogeny to find the function of sleep. *Nature Reviews Neuroscience*, *20*(2), pp.109-116.

Ara, S. and Islam, M., 2010. White fiber dissection of brain; the internal capsule: a cadaveric study. *Turkish neurosurgery*, *20*(3), pp.314-322.

Arrio-Dupont, M., Cribier, S., Foucault, G., Devaux, P.F. and d'Albis, A., 1996. Diffusion of fluorescently labeled macromolecules in cultured muscle cells. *Biophysical journal*, *70*(5), pp.2327-2332.

Atalik, K.E., Sahin, A.S. and Doğan, N., 2000. Interactions between phenylephrine, clonidine and xylazine in rat and rabbit aortas. *Methods and findings in experimental and clinical pharmacology*, *22*(3), pp.145-147.

Augustine, G.J., Fitzpatrick, D., Hall, W., Lamantia, A.S., Purves, D. and White, L., 2015. *Neurosciences*. De Boeck Superieur, pp.139.

Bass, M., Stryland, E.W.V., Williams, D.R. and Wolfe, W.L., 1995. Handbook of optics volume ii devices, measurements. *Handbook of Optics Volume II Devices*.

Bentivoglio, M. and Grassi-Zucconi, G., 1997. The pioneering experimental studies on sleep deprivation. *Sleep*, *20*(7), pp.570-576.

Benveniste, H., Liu, X., Koundal, S., Sanggaard, S., Lee, H. and Wardlaw, J., 2019. The glymphatic system and waste clearance with brain aging: a review. *Gerontology*, *65*(2), pp.106-119.

Berger A. 2002. Magnetic resonance imaging. *BMJ (Clinical research ed.)*, 324(7328), 35.

Besedovsky, L., Lange, T. and Born, J., 2012. Sleep and immune function. *Pflügers Archiv-European Journal of Physiology*, *463*(1), pp.121-137.

Biceroglu, H., Albayram, S., Ogullar, S., Hasiloglu, Z.I., Selcuk, H., Yuksel, O., Karaaslan, B., Yildiz, C. and Kiris, A., 2012. Direct venous spinal reabsorption of cerebrospinal fluid: a new concept with serial magnetic resonance cisternography in rabbits. *Journal of Neurosurgery: Spine*, *16*(4), pp.394-401.

Binder, D.K., Papadopoulos, M.C., Haggie, P.M. and Verkman, A.S., 2004. In vivo measurement of brain extracellular space diffusion by cortical surface photobleaching. *Journal of Neuroscience*, *24*(37), pp.8049-8056.

Blumberg, M.S., Lesku, J.A., Libourel, P.A., Schmidt, M.H. and Rattenborg, N.C., 2020. What is REM sleep?. *Current biology*, *30*(1), pp.R38-R49.

Braga, J., Desterro, J.M. and Carmo-Fonseca, M., 2004. Intracellular macromolecular mobility measured by fluorescence recovery after photobleaching with confocal laser scanning microscopes. *Molecular biology of the cell*, *15*(10), pp.4749-4760.

Brightman, M.W. and Reese, T., 1969. Junctions between intimately apposed cell membranes in the vertebrate brain. *The Journal of cell biology*, *40*(3), pp.648-677.

Brightman, M.W., 1965. The distribution within the brain of ferritin injected into cerebrospinal fluid compartments. II. Parenchymal distribution. *American Journal of Anatomy*, *117*(2), pp.193-219.

Brinker, T., Stopa, E., Morrison, J. and Klinge, P., 2014. A new look at cerebrospinal fluid circulation. *Fluids and Barriers of the CNS*, *11*(1), pp.1-16.

Brinkman, J.E., Reddy, V. and Sharma, S., 2018. Physiology, sleep.

Carslaw, H.S., 1906. *Introduction to the Mathematical Theory of the Conduction of Heat in Solids*. Macmillan and Company, limited.

Carter, M. and Shieh, J.C., 2015. *Guide to research techniques in neuroscience. Chapter 5 pp. 117-144*. Academic Press.

Cathcart III, R.S. and Worthington Jr, W.C., 1964. Ciliary movement in the rat cerebral ventricles: clearing action and directions of currents. *Journal of Neuropathology & Experimental Neurology*, *23*(4), pp.609-618.

Chen, A.K., Cheng, Z., Behlke, M.A. and Tsourkas, A., 2008. Assessing the sensitivity of commercially available fluorophores to the intracellular environment. *Analytical chemistry*, *80*(19), pp.7437-7444.

Chen, M.Y., Lonser, R.R., Morrison, P.F., Governale, L.S. and Oldfield, E.H., 1999. Variables affecting convection-enhanced delivery to the striatum: a systematic examination of rate of infusion, cannula size, infusate concentration, and tissue—cannula sealing time. *Journal of neurosurgery*, *90*(2), pp.315-320.

Cirelli, C. and Tononi, G., 2021, March. The why and how of sleep-dependent synaptic down-selection. In *Seminars in Cell & Developmental Biology*. Academic Press.

Conn, P.M. ed., 2016. *Conn's translational neuroscience*. Academic Press.

Cooper, C.B., Neufeld, E.V., Dolezal, B.A. and Martin, J.L., 2018. Sleep deprivation and obesity in adults: a brief narrative review. *BMJ open sport & exercise medicine*, *4*(1), p.e000392.

Crank, J., 1979. *The mathematics of diffusion.* Oxford university press.

Cumming, G., 2013. *Understanding the new statistics: Effect sizes, confidence intervals, and meta-analysis*. Routledge.

Damkier, H.H., Brown, P.D. and Praetorius, J., 2013. Cerebrospinal fluid secretion by the choroid plexus. *Physiological reviews*, *93*(4), pp.1847-1892.

Daneman, R. and Prat, A., 2015. The blood–brain barrier. *Cold Spring Harbor perspectives in biology*, *7*(1), p.a020412.

Daneman, R., Zhou, L., Kebede, A.A. and Barres, B.A., 2010. Pericytes are required for blood–brain barrier integrity during embryogenesis. *Nature*, *468*(7323), pp.562-566.

Davoodi-Bojd, E., Ding, G., Zhang, L., Li, Q., Li, L., Chopp, M., Zhang, Z. and Jiang, Q., 2019. Modeling glymphatic system of the brain using MRI. *Neuroimage*, *188*, pp.616-627.

Davson, H., Kleeman, C.F. and Levin, E., 1963. The blood-brain barrier drugs and membranes, Vol. 4.

Demchenko, A.P., 2020. Photobleaching of organic fluorophores: quantitative characterization, mechanisms, protection. *Methods and Applications in Fluorescence*, *8*(2), p.022001.

Dijk, D.J. and Landolt, H.P., 2019. Sleep physiology, circadian rhythms, waking performance and the development of sleep-wake therapeutics. In *Sleep-Wake Neurobiology and Pharmacology* (pp. 441-481). Springer, Cham.

Efron, B., 1992. Bootstrap methods: another look at the jackknife. In *Breakthroughs in statistics* (pp. 569-593). Springer, New York, NY.

Egnor, M., Zheng, L., Rosiello, A., Gutman, F. and Davis, R., 2002. A model of pulsations in communicating hydrocephalus. *Pediatric neurosurgery*, *36*(6), pp.281-303.

Eide, P.K., Vatnehol, S.A.S., Emblem, K.E. and Ringstad, G., 2018. Magnetic resonance imaging provides evidence of glymphatic drainage from human brain to cervical lymph nodes. *Scientific reports*, *8*(1), pp.1-10.

Elkin, R., Nadeem, S., Haber, E., Steklova, K., Lee, H., Benveniste, H. and Tannenbaum, A., 2018, September. GlymphVIS: visualizing glymphatic transport pathways using regularized optimal transport. In *International Conference on Medical Image Computing and Computer-Assisted Intervention* (pp. 844-852). Springer, Cham.

Elkin, R., Nadeem, S., Lee, H., Benveniste, H. and Tannenbaum, A., 2020, October. Fisher-Rao regularized transport analysis of the glymphatic system and waste drainage. In *International Conference on Medical Image Computing and Computer-Assisted Intervention* (pp. 573-582). Springer, Cham.

Fenstermacher, J.D. and Patlak, C.S., 1976. The movements of water and solutes in the brains of mammals. In *Dynamics of brain edema* (pp. 87-94). Springer, Berlin, Heidelberg.

Fick, A., 1855. V. On liquid diffusion. *The London, Edinburgh, and Dublin Philosophical Magazine and Journal of Science*, *10*(63), pp.30-39.

Frank, M.G. and Heller, H.C., 2018. The function (s) of sleep. In *Sleep-Wake Neurobiology and Pharmacology* (pp. 3-34). Springer, Cham.

Franks, N.P., 2008. General anaesthesia: from molecular targets to neuronal pathways of sleep and arousal. *Nature Reviews Neuroscience*, *9*(5), pp.370-386.

Fyfe, I., 2020. Brain waste clearance reduced by ageing. *Nature Reviews Neurology*, *16*(3), pp.128-128.

Geer, C.P. and Grossman, S.A., 1997. Interstitial fluid flow along white matter tracts: a potentially important mechanism for the dissemination of primary brain tumors. *Journal of Neuro-oncology*, *32*(3), pp.193-201.

Gelegen, C., Gent, T.C., Ferretti, V., Zhang, Z., Yustos, R., Lan, F., Yang, Q., Overington, D.W., Vyssotski, A.L., van Lith, H.A. and Wisden, W., 2014. Staying awake–a genetic region that hinders α2 adrenergic receptor agonist‐induced sleep. *European Journal of Neuroscience*, *40*(1), pp.2311-2319.

Ghannam, J.Y. and Al Kharazi, K.A., 2019. Neuroanatomy, cranial meninges.

Gifford, F., 1955. Atmospheric diffusion from volume sources. *Journal of the Atmospheric Sciences*, *12*(3), pp.245-251.

Gillooly, J.F., Brown, J.H., West, G.B., Savage, V.M. and Charnov, E.L., 2001. Effects of size and temperature on metabolic rate. *science*, *293*(5538), pp.2248-2251.

Grandin, L.D., Alloy, L.B. and Abramson, L.Y., 2006. The social zeitgeber theory, circadian rhythms, and mood disorders: review and evaluation. *Clinical psychology review*, *26*(6), pp.679-694.

Grandner, M.A., Seixas, A., Shetty, S. and Shenoy, S., 2016. Sleep duration and diabetes risk: population trends and potential mechanisms. *Current diabetes reports*, *16*(11), pp.1-14.

Greenberg, R.W., Lane, E.L., Cinnamon, J., Farmer, P. and Hyman, R.A., 1994, December. The cranial meninges: anatomic considerations. In *Seminars in Ultrasound, CT and MRI* (Vol. 15, No. 6, pp. 454-465). WB Saunders.

Guyton, A.C. and Hall, J.E., 2000. The body fluid compartments: extracellular and intracellular fluids; interstitial fluid and edema. *Textbook of medical physiology*, *9*, pp.306-8.

Hablitz, L.M., Plá, V., Giannetto, M., Vinitsky, H.S., Stæger, F.F., Metcalfe, T., Nguyen, R., Benrais, A. and Nedergaard, M., 2020. Circadian control of brain glymphatic and lymphatic fluid flow. *Nature communications*, *11*(1), pp.1-11.

Hablitz, L.M., Vinitsky, H.S., Sun, Q., Stæger, F.F., Sigurdsson, B., Mortensen, K.N., Lilius, T.O. and Nedergaard, M., 2019. Increased glymphatic influx is correlated with high EEG delta power and low heart rate in mice under anesthesia. *Science advances*, *5*(2), p.eaav5447.

Haines, D.E. and Mihailoff, G.A., 2017. *Fundamental neuroscience for basic and clinical applications E-book*. Elsevier Health Sciences.

Harding, E.C., Yu, X., Miao, A., Andrews, N., Ma, Y., Ye, Z., Lignos, L., Miracca, G., Ba, W., Yustos, R. and Vyssotski, A.L., 2018. A neuronal hub binding sleep initiation and body cooling in response to a warm external stimulus. *Current Biology*, *28*(14), pp.2263-2273.

Hawkins, B.T. and Egleton, R.D., 2006. Fluorescence imaging of blood–brain barrier disruption. *Journal of neuroscience methods*, *151*(2), pp.262-267.

Heinzmann, U., 1980. FITC-dextrans as fluorescence and electron microscopic tracers in studies on capillary and cell permeability of the CNS. *Experientia*, *36*(7), pp.885-887.

Hill, R.A., Tong, L., Yuan, P., Murikinati, S., Gupta, S. and Grutzendler, J., 2015. Regional blood flow in the normal and ischemic brain is controlled by arteriolar smooth muscle cell contractility and not by capillary pericytes. *Neuron*, 87(1), pp.95-110.

His, W., 1865. *Über ein perivasculäres Canalsystem in den nervösen Centralorganen und über dessen Beziehungen zum Lymphsystem*. W. Engelmann.

Hladky, S.B. and Barrand, M.A., 2014. Mechanisms of fluid movement into, through and out of the brain: evaluation of the evidence. *Fluids and Barriers of the CNS*, *11*(1), pp.1-32.

Ho, J., Tumkaya, T., Aryal, S., Choi, H. and Claridge-Chang, A., 2019. Moving beyond P values: data analysis with estimation graphics. *Nature methods*, *16*(7), pp.565-566.

Hoekstra, M.M., Emmenegger, Y., Hubbard, J. and Franken, P., 2019. Cold-inducible RNA-binding protein (CIRBP) adjusts clock-gene expression and REM-sleep recovery following sleep deprivation. *Elife*, *8*, p.e43400.

Holter, K.E., Kehlet, B., Devor, A., Sejnowski, T.J., Dale, A.M., Omholt, S.W., Ottersen, O.P., Nagelhus, E.A., Mardal, K.A. and Pettersen, K.H., 2017. Interstitial solute transport in 3D reconstructed neuropil occurs by diffusion rather than bulk flow. *Proceedings of the National Academy of Sciences*, *114*(37), pp.9894-9899.

Hoogstraate, A.J., Cullander, C., Nagelkerke, J.F., Senel, S., Verhoef, J., Junginger, H.E. and Boddé, H.E., 1994. Diffusion rates and transport pathways of fluorescein isothiocyanate (FITC)-labeled model compounds through buccal epithelium. *Pharmaceutical research*, *11*(1), pp.83-89.

Hsieh B., E. C. Harding, W. Wisden, N. P. Franks and T. G. Constandinou, "A Miniature Neural Recording Device to Investigate Sleep and Temperature Regulation in Mice," *2019 IEEE Biomedical Circuits and Systems Conference (BioCAS)*, 2019, pp. 1-4, doi: 10.1109/BIOCAS.2019.8918722.

Iliff, J.J. and Nedergaard, M., 2013. Is there a cerebral lymphatic system?. *Stroke*, *44*, pp.S93-S95.

Iliff, J.J., Wang, M., Liao, Y., Plogg, B.A., Peng, W., Gundersen, G.A., Benveniste, H., Vates, G.E., Deane, R., Goldman, S.A. and Nagelhus, E.A., 2012. A paravascular pathway facilitates CSF flow through the brain parenchyma and the clearance of interstitial solutes, including amyloid β. *Science translational medicine*, *4*(147), pp.147ra111-147ra111.

Jack Jr, C.R., Lowe, V.J., Senjem, M.L., Weigand, S.D., Kemp, B.J., Shiung, M.M., Knopman, D.S., Boeve, B.F., Klunk, W.E., Mathis, C.A. and Petersen, R.C., 2008. 11C PiB and structural MRI provide complementary information in imaging of Alzheimer's disease and amnestic mild cognitive impairment. *Brain*, *131*(3), pp.665-680.

Jessen, N.A., Munk, A.S.F., Lundgaard, I. and Nedergaard, M., 2015. The glymphatic system: a beginner's guide. *Neurochemical research*, *40*(12), pp.2583-2599.

Jin, B.J., Smith, A.J. and Verkman, A.S., 2016. Spatial model of convective solute transport in brain extracellular space does not support a "glymphatic" mechanism. *Journal of General Physiology*, *148*(6), pp.489-501.

Johanson, C.E., Duncan, J.A., Klinge, P.M., Brinker, T., Stopa, E.G. and Silverberg, G.D., 2008. Multiplicity of cerebrospinal fluid functions: new challenges in health and disease. *Cerebrospinal fluid research*, *5*(1), pp.1-32.

Johnston, M., Zakharov, A., Papaiconomou, C., Salmasi, G. and Armstrong, D., 2004. Evidence of connections between cerebrospinal fluid and nasal lymphatic vessels in humans, non-human primates and other mammalian species. *Cerebrospinal fluid research*, *1*(1), pp.1-13.

Jung, C.M., Melanson, E.L., Frydendall, E.J., Perreault, L., Eckel, R.H. and Wright, K.P., 2011. Energy expenditure during sleep, sleep deprivation and sleep following sleep deprivation in adult humans. *The Journal of physiology*, *589*(1), pp.235-244.

Kanaya, H.J., Park, S., Kim, J.H., Kusumi, J., Krenenou, S., Sawatari, E., Sato, A., Lee, J., Bang, H., Kobayakawa, Y. and Lim, C., 2020. A sleep-like state in Hydra unravels conserved sleep mechanisms during the evolutionary development of the central nervous system. *Science advances*, *6*(41), p.eabb9415.

Kaur, J., Fahmy, L.M., Davoodi-Bojd, E., Zhang, L., Ding, G., Hu, J., Zhang, Z., Chopp, M. and Jiang, Q., 2021. Waste Clearance in the Brain. *Frontiers in neuroanatomy*, p.53.

Keep, R.F. and Jones, H.C., 1990. A morphometric study on the development of the lateral ventricle choroid plexus, choroid plexus capillaries and ventricular ependyma in the rat. *Developmental Brain Research*, *56*(1), pp.47-53.

Khan, M.S. and Aouad, R., 2017. The effects of insomnia and sleep loss on cardiovascular disease. *Sleep medicine clinics*, *12*(2), pp.167-177.

Khasawneh, A.H., Garling, R.J. and Harris, C.A., 2018. Cerebrospinal fluid circulation: what do we know and how do we know it?. *Brain circulation*, *4*(1), p.14.

Kihara, T., Ito, J. and Miyake, J., 2013. Measurement of biomolecular diffusion in extracellular matrix condensed by fibroblasts using fluorescence correlation spectroscopy. *PLoS One*, *8*(11), p.e82382.

Kimelberg, H.K., 2004. Water homeostasis in the brain: basic concepts. *Neuroscience*, *129*(4), pp.851-860.

Klose, U., Strik, C., Kiefer, C. and Grodd, W., 2000. Detection of a relation between respiration and CSF pulsation with an echoplanar technique. *Journal of Magnetic Resonance Imaging*, *11*(4), pp.438-444.

Kress, B.T., Iliff, J.J., Xia, M., Wang, M., Wei, H.S., Zeppenfeld, D., Xie, L., Kang, H., Xu, Q., Liew, J.A. and Plog, B.A., 2014. Impairment of paravascular clearance pathways in the aging brain. *Annals of neurology*, *76*(6), pp.845-861.

Krueger, J.M., Nguyen, J.T., Dykstra-Aiello, C.J. and Taishi, P., 2019. Local sleep. *Sleep medicine reviews*, *43*, pp.14-21.

Kulik, T., Kusano, Y., Aronhime, S., Sandler, A.L. and Winn, H.R., 2008. Regulation of cerebral vasculature in normal and ischemic brain. *Neuropharmacology*, *55*(3), pp.281-288.

Lähdesmäki, J., Sallinen, J., MacDonald, E., Sirviö, J. and Scheinin, M., 2003. α2-Adrenergic drug effects on brain monoamines, locomotion, and body temperature are largely abolished in mice lacking the α2A-adrenoceptor subtype. *Neuropharmacology*, *44*(7), pp.882-892.

Lai, A.Y. and McLaurin, J., 2011. Mechanisms of amyloid-Beta Peptide uptake by neurons: the role of lipid rafts and lipid raft-associated proteins. *International journal of Alzheimer's disease*, *2011*.

Lazarus, M., Chen, J.F., Urade, Y. and Huang, Z.L., 2013. Role of the basal ganglia in the control of sleep and wakefulness. *Current opinion in neurobiology*, *23*(5), pp.780-785.

Le Merre, P., Ährlund-Richter, S. and Carlén, M., 2021. The mouse prefrontal cortex: Unity in diversity. *Neuron*, *109*(12), pp.1925-1944.

Lee, H., Xie, L., Yu, M., Kang, H., Feng, T., Deane, R., Logan, J., Nedergaard, M. and Benveniste, H., 2015. The effect of body posture on brain glymphatic transport. *Journal of Neuroscience*, *35*(31), pp.11034-11044.

Lehtinen, M.K., Bjornsson, C.S., Dymecki, S.M., Gilbertson, R.J., Holtzman, D.M. and Monuki, E.S., 2013. The choroid plexus and cerebrospinal fluid: emerging roles in development, disease, and therapy. *Journal of Neuroscience*, *33*(45), pp.17553-17559.

Li, L., Ding, G., Zhang, L., Davoodi-Bojd, E., Chopp, M., Li, Q., Zhang, Z.G. and Jiang, Q., 2022. Aging-related Alterations of Glymphatic Transport in Rat: in vivo MRI and Kinetic Study. *Frontiers in Aging Neuroscience*, p.208.

Libourel, P.A., Corneyllie, A., Luppi, P.H., Chouvet, G. and Gervasoni, D., 2015. Unsupervised online classifier in sleep scoring for sleep deprivation studies. *Sleep*, *38*(5), pp.815-828.

Lilius, T.O., Blomqvist, K., Hauglund, N.L., Liu, G., Stæger, F.F., Bærentzen, S., Du, T., Ahlström, F., Backman, J.T., Kalso, E.A. and Rauhala, P.V., 2019. Dexmedetomidine enhances glymphatic brain delivery of intrathecally administered drugs. *Journal of Controlled Release*, *304*, pp.29-38.

Liu, L. and Duff, K., 2008. A technique for serial collection of cerebrospinal fluid from the cisterna magna in mouse. *JoVE (Journal of Visualized Experiments)*, (21), p.e960.

Lo, A.C., Iscru, E., Blum, D., Tesseur, I., Callaerts-Vegh, Z., Buée, L., De Strooper, B., Balschun, D. and D'Hooge, R., 2013. Amyloid and tau neuropathology differentially affect prefrontal

synaptic plasticity and cognitive performance in mouse models of Alzheimer's disease. *Journal of Alzheimer's Disease*, *37*(1), pp.109-125.

Lun, M.P., Monuki, E.S. and Lehtinen, M.K., 2015. Development and functions of the choroid plexus–cerebrospinal fluid system. *Nature Reviews Neuroscience*, *16*(8), pp.445-457.

Lyamin, O., Pryaslova, J., Lance, V. and Siegel, J., 2005. Continuous activity in cetaceans after birth. *Nature*, *435*(7046), pp.1177-1177.

Lyamin, O.I. and Siegel, J.M., 2019. Sleep in aquatic mammals. In *Handbook of behavioral neuroscience* (Vol. 30, pp. 375-393). Elsevier.

Ma, Q., Ineichen, B.V., Detmar, M. and Proulx, S.T., 2017. Outflow of cerebrospinal fluid is predominantly through lymphatic vessels and is reduced in aged mice. *Nature communications*, *8*(1), pp.1-13.

Madsen, P.L., Schmidt, J.F., Wildschiodtz, G.O.R.D.O.N., Friberg, L.A.R.S., Holm, S.O.R.E.N., Vorstrup, S. and Lassen, N.A., 1991. Cerebral O2 metabolism and cerebral blood flow in humans during deep and rapid-eye-movement sleep. *Journal of applied physiology*, *70*(6), pp.2597-2601.

McMakin, D.L. and Alfano, C.A., 2015. Sleep and anxiety in late childhood and early adolescence. *Current opinion in psychiatry*, *28*(6), p.483.

Mestre, H., Mori, Y. and Nedergaard, M., 2020. The brain's glymphatic system: current controversies. *Trends in neurosciences*, *43*(7), pp.458-466.

Mestre, H., Tithof, J., Du, T., Song, W., Peng, W., Sweeney, A.M., Olveda, G., Thomas, J.H., Nedergaard, M. and Kelley, D.H., 2018. Flow of cerebrospinal fluid is driven by arterial pulsations and is reduced in hypertension. *Nature communications*, *9*(1), pp.1-9.

Millen, J.W. and Woollam, D.H.M., 1962. *The anatomy of the cerebrospinal fluid*. Oxford University Press.

Mori, T., Shimada, H., Shinotoh, H., Hirano, S., Eguchi, Y., Yamada, M., Fukuhara, R., Tanimukai, S., Zhang, M.R., Kuwabara, S. and Ueno, S.I., 2014. Apathy correlates with prefrontal amyloid β deposition in Alzheimer's disease. *Journal of Neurology, Neurosurgery & Psychiatry*, *85*(4), pp.449-455.

Muldoon, L.L., Alvarez, J.I., Begley, D.J., Boado, R.J., Del Zoppo, G.J., Doolittle, N.D., Engelhardt, B., Hallenbeck, J.M., Lonser, R.R., Ohlfest, J.R. and Prat, A., 2013. Immunologic privilege in the central nervous system and the blood–brain barrier. *Journal of Cerebral Blood Flow & Metabolism*, *33*(1), pp.13-21.

Müller, U.C. and Zheng, H., 2012. Physiological functions of APP family proteins. *Cold Spring Harbor perspectives in medicine*, *2*(2), p.a006288.

Munson, B.R., Young, D.F., Okiishi, T.H. and Huebsch, W.W., 2006. Fundamentals of Fluid Mechanics, John Wiley & Sons. *Inc., USA*.

Murtha, L.A., Yang, Q., Parsons, M.W., Levi, C.R., Beard, D.J., Spratt, N.J. and McLeod, D.D., 2014. Cerebrospinal fluid is drained primarily via the spinal canal and olfactory route in young and aged spontaneously hypertensive rats. *Fluids and Barriers of the CNS*, *11*(1), pp.1-9.

Musizza, B., Stefanovska, A., McClintock, P.V., Paluš, M., Petrovčič, J., Ribarič, S. and Bajrović, F.F., 2007. Interactions between cardiac, respiratory and EEG-δ oscillations in rats during anaesthesia. *The journal of Physiology*, *580*(1), pp.315-326.

Nakada, T. and Kwee, I.L., 2019. Fluid dynamics inside the brain barrier: current concept of interstitial flow, glymphatic flow, and cerebrospinal fluid circulation in the brain. *The Neuroscientist*, *25*(2), pp.155-166.

Nedergaard, M., 2013. Garbage truck of the brain. *Science*, *340*(6140), pp.1529-1530.

Nicholson, C., 1985. Diffusion from an injected volume of a substance in brain tissue with arbitrary volume fraction and tortuosity. *Brain research*, *333*(2), pp.325-329.

Nilsson, C., Stahlberg, F., Thomsen, C., Henriksen, O., Herning, M. and Owman, C., 1992. Circadian variation in human cerebrospinal fluid production measured by magnetic resonance imaging. *American Journal of Physiology-Regulatory, Integrative and Comparative Physiology*, *262*(1), pp.R20-R24.

Norwood, J.N., Zhang, Q., Card, D., Craine, A., Ryan, T.M. and Drew, P.J., 2019. Anatomical basis and physiological role of cerebrospinal fluid transport through the murine cribriform plate. *Elife*, *8*, p.e44278.

O'brien, R.J. and Wong, P.C., 2011. Amyloid precursor protein processing and Alzheimer's disease. *Annual review of neuroscience*, *34*, p.185.

Odackal, J., Colbourn, R., Odackal, N.J., Tao, L., Nicholson, C. and Hrabetova, S., 2017. Real-time iontophoresis with tetramethylammonium to quantify volume fraction and tortuosity of brain extracellular space. *JoVE (Journal of Visualized Experiments)*, (125), p.e55755.

Oros-Peusquens, A.M., Loução, R., Abbas, Z., Gras, V., Zimmermann, M. and Shah, N.J., 2019. A single-scan, rapid whole-brain protocol for quantitative water content mapping with neurobiological implications. *Frontiers in Neurology*, p.1333.

Owen, S.F., Liu, M.H. and Kreitzer, A.C., 2019. Thermal constraints on in vivo optogenetic manipulations. *Nature neuroscience*, *22*(7), pp.1061-1065.

Paxinos, G. and Franklin, K.B., 2019. *Paxinos and Franklin's the mouse brain in stereotaxic coordinates*. Academic press.

Pizzo, M.E., Wolak, D.J., Kumar, N.N., Brunette, E., Brunnquell, C.L., Hannocks, M.J., Abbott, N.J., Meyerand, M.E., Sorokin, L., Stanimirovic, D.B. and Thorne, R.G., 2018. Intrathecal antibody distribution in the rat brain: surface diffusion, perivascular transport and osmotic enhancement of delivery. *The Journal of physiology*, *596*(3), pp.445-475.

Prince, E.A. and Ahn, S.H., 2013, September. Basic vascular neuroanatomy of the brain and spine: what the general interventional radiologist needs to know. In *Seminars in interventional radiology* (Vol. 30, No. 03, pp. 234-239). Thieme Medical Publishers.

Proescholdt, M.G., Hutto, B., Brady, L.S. and Herkenham, M., 1999. Studies of cerebrospinal fluid flow and penetration into brain following lateral ventricle and cisterna magna injections of the tracer [14C] inulin in rat. *Neuroscience*, *95*(2), pp.577-592.

Pryaslova, J.P., Lyamin, O.I., Siegel, J.M. and Mukhametov, L.M., 2009. Behavioral sleep in the walrus. *Behavioural brain research*, *201*(1), pp.80-87.

Ratner, V., Gao, Y., Lee, H., Elkin, R., Nedergaard, M., Benveniste, H. and Tannenbaum, A., 2017. Cerebrospinal and interstitial fluid transport via the glymphatic pathway modeled by optimal mass transport. *Neuroimage*, *152*, pp.530-537.

Ratner, V., Zhu, L., Kolesov, I., Nedergaard, M., Benveniste, H. and Tannenbaum, A., 2015, March. Optimal-mass-transfer-based estimation of glymphatic transport in living brain. In *Medical Imaging 2015: Image Processing* (Vol. 9413, pp. 406-411). SPIE.

Rechtschaffen, A., Gilliland, M.A., Bergmann, B.M. and Winter, J.B., 1983. Physiological correlates of prolonged sleep deprivation in rats. *Science*, *221*(4606), pp.182-184.

Redzic, Z., 2011. Molecular biology of the blood-brain and the blood-cerebrospinal fluid barriers: similarities and differences. *Fluids and Barriers of the CNS*, *8*(1), pp.1-25.

Rennels, M.L., Blaumanis, O.R. and Grady, P.A., 1990. Rapid solute transport throughout the brain via paravascular fluid pathways. *Advances in neurology*, *52*, pp.431-439.

Rennels, M.L., Gregory, T.F., Blaumanis, O.R., Fujimoto, K. and Grady, P.A., 1985. Evidence for a 'paravascular'fluid circulation in the mammalian central nervous system, provided by the rapid distribution of tracer protein throughout the brain from the subarachnoid space. *Brain research*, *326*(1), pp.47-63.

Ringstad, G., Vatnehol, S.A.S. and Eide, P.K., 2017. Glymphatic MRI in idiopathic normal pressure hydrocephalus. *Brain*, *140*(10), pp.2691-2705.

Rovainen, C.M., Woolsey, T.A., Blocher, N.C., Wang, D.B. and Robinson, O.F., 1993. Blood flow in single surface arterioles and venules on the mouse somatosensory cortex measured with videomicroscopy, fluorescent dextrans, nonoccluding fluorescent beads, and computer-assisted image analysis. *Journal of Cerebral Blood Flow & Metabolism*, 13(3), pp.359-371.

Ruf, T. and Geiser, F., 2015. Daily torpor and hibernation in birds and mammals. *Biological Reviews*, *90*(3), pp.891-926.

Saadoun, S. and Papadopoulos, M.C., 2010. Aquaporin-4 in brain and spinal cord oedema. *Neuroscience*, *168*(4), pp.1036-1046.

Sakka, L., Coll, G. and Chazal, J., 2011. Anatomy and physiology of cerebrospinal fluid. *European annals of otorhinolaryngology, head and neck diseases*, *128*(6), pp.309-316.

Sallinen, Jukka, Richard E. Link, Antti Haapalinna, Timo Viitamaa, Maya Kulatunga, Birgitta Sjöholm, Ewen Macdonald et al. "Genetic alteration of α2C-adrenoceptor expression in mice: influence on locomotor, hypothermic, and neurochemical effects of dexmedetomidine, a subtype-nonselective α2-adrenoceptor agonist." *Molecular pharmacology* 51, no. 1 (1997): 36-46.

Schantz, E.J. and Lauffer, M.A., 1962. Diffusion measurements in agar gel. *Biochemistry*, *1*(4), pp.658-663.

Scheinin, A., Kallionpää, R.E., Li, D., Kallioinen, M., Kaisti, K., Långsjö, J., Maksimow, A., Vahlberg, T., Valli, K., Mashour, G.A. and Revonsuo, A., 2018. Differentiating drug-related and state-related effects of dexmedetomidine and propofol on the electroencephalogram. *Anesthesiology*, *129*(1), pp.22-36.

Schröder, H., Moser, N. and Huggenberger, S., 2020. The Mouse Caudate Putamen, Motor System, and Nucleus Accumbens. In *Neuroanatomy of the Mouse* (pp. 305-318). Springer, Cham.

Seksek, O., Biwersi, J. and Verkman, A.S., 1997. Translational diffusion of macromolecule-sized solutes in cytoplasm and nucleus. *The Journal of cell biology*, *138*(1), pp.131-142.

Siegel, J.M., 2005. Clues to the functions of mammalian sleep. *Nature*, *437*(7063), pp.1264-1271.

Siegel, J.M., 2009. Sleep viewed as a state of adaptive inactivity. *Nature Reviews Neuroscience*, *10*(10), pp.747-753.

Siegel, Jerome M., 2009. "Sleep viewed as a state of adaptive inactivity." *Nature Reviews Neuroscience* 10, no. 10: 747-753.

Silva, J.V.C., Peixoto, P.D.S., Lortal, S. and Floury, J., 2013. Transport phenomena in a model cheese: The influence of the charge and shape of solutes on diffusion. *Journal of Dairy Science*, *96*(10), pp.6186-6198.

Smith, A.J., Yao, X., Dix, J.A., Jin, B.J. and Verkman, A.S., 2017. Test of the 'glymphatic' hypothesis demonstrates diffusive and aquaporin-4-independent solute transport in rodent brain parenchyma. *elife*, *6*, p.e27679.

Sofroniew, M.V. and Vinters, H.V., 2010. Astrocytes: biology and pathology. *Acta neuropathologica*, *119*(1), pp.7-35.

Song, L., Hennink, E.J., Young, I.T. and Tanke, H.J., 1995. Photobleaching kinetics of fluorescein in quantitative fluorescence microscopy. *Biophysical journal*, *68*(6), pp.2588-2600.

Stujenske, J.M., Spellman, T. and Gordon, J.A., 2015. Modeling the spatiotemporal dynamics of light and heat propagation for in vivo optogenetics. *Cell reports*, *12*(3), pp.525-534.

Sullivan, K.D., Sipprell III, W.H., Brown Jr, E.B. and Brown III, E.B., 2009. Improved model of fluorescence recovery expands the application of multiphoton fluorescence recovery after photobleaching in vivo. *Biophysical journal*, *96*(12), pp.5082-5094.

Syková, E. and Nicholson, C., 2008. Diffusion in brain extracellular space. *Physiological reviews*, *88*(4), pp.1277-1340.

Thiagarajah, J.R., Kim, J.K., Magzoub, M. and Verkman, A.S., 2006. Slowed diffusion in tumors revealed by microfiberoptic epifluorescence photobleaching. *Nature methods*, *3*(4), pp.275-280.

Thomas, A., Wang, S., Sohrabi, S., Orr, C., He, R., Shi, W. and Liu, Y., 2017. Characterization of vascular permeability using a biomimetic microfluidic blood vessel model. *Biomicrofluidics*, *11*(2), p.024102.

Thorball, N., 1981. FITC-dextran tracers in microcirculatory and permeability studies using combined fluorescence stereo microscopy, fluorescence light microscopy and electron microscopy. *Histochemistry*, *71*(2), pp.209-233.

Thorne, R.G. and Nicholson, C., 2006. In vivo diffusion analysis with quantum dots and dextrans predicts the width of brain extracellular space. *Proceedings of the National Academy of Sciences*, *103*(14), pp.5567-5572.

Tithof, J., Kelley, D.H., Mestre, H., Nedergaard, M. and Thomas, J.H., 2019. Hydraulic resistance of periarterial spaces in the brain. *Fluids and Barriers of the CNS*, *16*(1), pp.1-13.

Tomita, S., Kirino, Y. and Suzuki, T., 1998. Cleavage of Alzheimer's amyloid precursor protein (APP) by secretases occurs after O-glycosylation of APP in the protein secretory pathway: identification of intracellular compartments in which APP cleavage occurs without using toxic agents that interfere with protein metabolism. *Journal of Biological Chemistry*, *273*(11), pp.6277-6284.

Tsuji, A. and Ohnishi, S., 1986. Restriction of the lateral motion of band 3 in the erythrocyte membrane by the cytoskeletal network: dependence on spectrin association state. *Biochemistry*, *25*(20), pp.6133-6139.

Vaccaro, A., Dor, Y.K., Nambara, K., Pollina, E.A., Lin, C., Greenberg, M.E. and Rogulja, D., 2020. Sleep loss can cause death through accumulation of reactive oxygen species in the gut. *Cell*, *181*(6), pp.1307-1328.

Verkman, A.S., 2003. [28] Diffusion in cells measured by fluorescence recovery after photobleaching. In *Methods in enzymology* (Vol. 360, pp. 635-648). Academic Press.

Verkman, A.S., 2013. Diffusion in the extracellular space in brain and tumors. *Physical biology*, *10*(4), p.045003.

Waharte, F., Steenkeste, K., Briandet, R. and Fontaine-Aupart, M.P., 2010. Diffusion measurements inside biofilms by image-based fluorescence recovery after photobleaching (FRAP) analysis with a commercial confocal laser scanning microscope. *Applied and environmental microbiology*, *76*(17), pp.5860-5869.

Watts, R., Steinklein, J.M., Waldman, L., Zhou, X. and Filippi, C.G., 2019. Measuring glymphatic flow in man using quantitative contrast-enhanced MRI. *American Journal of Neuroradiology*, *40*(4), pp.648-651.

Weed, L.H., 1914. Studies on Cerebro-Spinal Fluid. No. III: The pathways of escape from the Subarachnoid Spaces with particular reference to the Arachnoid Villi. *The Journal of medical research*, *31*(1), p.51.

Wolak, D.J. and Thorne, R.G., 2013. Diffusion of macromolecules in the brain: implications for drug delivery. *Molecular pharmaceutics*, *10*(5), pp.1492-1504.

Wolman, M., Klatzo, I., Chui, E., Wilmes, F., Nishimoto, K., Fujiwara, K. and Spatz, M., 1981. Evaluation of the dye-protein tracers in pathophysiology of the blood-brain barrier. *Acta neuropathologica*, *54*(1), pp.55-61.

Woollam, D.H.M. and Millen, J.W., 1954. Perivascular spaces of the mammalian central nervous system. *Biological Reviews*, *29*(3), pp.251-283.

Xie, L., Kang, H., Xu, Q., Chen, M.J., Liao, Y., Thiyagarajan, M., O'Donnell, J., Christensen, D.J., Nicholson, C., Iliff, J.J. and Takano, T., 2013. Sleep drives metabolite clearance from the adult brain. *science*, *342*(6156), pp.373-377.

Yamada, S., Miyazaki, M., Yamashita, Y., Ouyang, C., Yui, M., Nakahashi, M., Shimizu, S., Aoki, I., Morohoshi, Y. and McComb, J.G., 2013. Influence of respiration on cerebrospinal fluid movement using magnetic resonance spin labeling. *Fluids and Barriers of the CNS*, *10*(1), pp.1-7.

Zador, Z., Magzoub, M., Jin, S., Manley, G.T., Papadopoulos, M.C. and Verlanan, A.S., 2008. Microfiberoptic fluorescence photobleaching reveals size‐dependent macromolecule diffusion in extracellular space deep in brain. *The FASEB Journal*, *22*(3), pp.870-879.

Zhang, E.T., Inman, C.B. and Weller, R., 1990. Interrelationships of the pia mater and the perivascular (Virchow-Robin) spaces in the human cerebrum. *Journal of anatomy*, *170*, p.111.

Zhang, H. and Verkman, A.S., 2010. Microfiberoptic measurement of extracellular space volume in brain and tumor slices based on fluorescent dye partitioning. *Biophysical journal*, *99*(4), pp.1284-1291.

Zhang, L. and McClellan, A.D., 1999. Axonal regeneration of descending brain neurons in larval lamprey demonstrated by retrograde double labeling. *Journal of Comparative Neurology*, *410*(4), pp.612-626.

Zhuo, J.M., Prakasam, A., Murray, M.E., Zhang, H.Y., Baxter, M.G., Sambamurti, K. and Nicolle, M.M., 2008. An increase in Aβ42 in the prefrontal cortex is associated with a reversal-learning impairment in Alzheimer's disease model Tg2576 APPsw mice. *Current Alzheimer Research*, *5*(4), pp.385-391.

Appendix

The following is the custom MATLAB script for EEG/EMG and photometry data analysis.

```
% This script is to help the analysis of photometry data by automatically
% identifying the sections of data where
% there has been a bleaching and writing files, one for each bleaching
% experiment. The script also sleep scores and identifies the vigilance
% states over the region selected for analysis and outputs the percentages
% of each vigilance state, WAKE, NREM and REM automatically using a custom
% offline sleep stage scornig algorithm

% Data must be stored in three separate folders, labelled "Photometry","EEG","Time"
% The folders must contain Photometry data as .csv files , EEG and Time (starting time, one
% line per data) data as .txt files
% Photometry and EEG data need to be labelled with a two digit integer suffix and
% data from the same experiment must have the same suffix Eg, {EEG01,Photo01}, {EEG02,Photo02}.
% User will be asked at the start of the script to point to the folder
% containing the three separate sub folders
% The scrip will allow the user to either select a particular data to
% analyse or to analyse all data automatically

% The scrip reads in the first two columns of each photometry data
% Column one is real time in seconds and column 2 is the photometry intensity
% Note that the EEG data are sampled at 200 Hz while the photometry data
% are sampled at a different value (about 3.7 Hz)

% First choose the folder containing the subfolders organised as described above
% Count the number of EEG and Photometry files in the folders
folderpath = uigetdir();
if ~isequal(folderpath,0)
    photo_files_tmp = dir(folderpath+"\Photometry\*.csv");
    n_photo_files = numel(photo_files_tmp);
    eeg_files_tmp   = dir(folderpath+"\EEG\*.txt");
    n_eeg_files   = numel(eeg_files_tmp);
end

% Check if the number of EEG files match the number of Photometry files
if((n_photo_files<=0)||(n_photo_files~=n_eeg_files))
    msgbox('Number of EEG files doesnt matach with number of Photo files','Message','modal')
    return
end

% Read in the text file containing the starting times
time_stamp = dlmread(folderpath+"\Time\Time.txt");

% Organise each EEG data and Photometry data into structs by looking the
% suffix integer ( two digits )
for n=1:n_eeg_files
    idx = 10*str2double(photo_files_tmp(n).name(end-5)) + str2double(photo_files_tmp(n).name(end-
4));
    [photo_files_tmp(n).idx] = idx;

    idx = 10*str2double(eeg_files_tmp(n).name(end-5)) + str2double(eeg_files_tmp(n).name(end-4));
    [eeg_files_tmp(n).idx] = idx ;
end

% Sort the structs to match each EEG data with Photometry
photo_files = photo_files_tmp;
[x,idx] = sort([photo_files.idx]);
photo_files = photo_files(idx);

eeg_files = eeg_files_tmp;
[x,idx] = sort([eeg_files.idx]);
eeg_files = eeg_files(idx);


% Choose either automatic scoring or look at one particular data
```

```
script_mode = str2double(inputdlg('Enter 1 for Auto, 2 for Manual'));
if(script_mode==1)
    n_of_files = n_photo_files;
    starting_file = str2double(inputdlg('Enter starting file number'));
elseif(script_mode==2)
    list = struct2cell(photo_files);
    [idx,tf] = listdlg('ListString',list(1,1,:),'SelectionMode','single');
    starting_file = idx;
    n_of_files = idx;
else
    return;
end

% Loop until all data files have been processed
for n=starting_file:n_of_files
    % Clear previous variables and declare global sigma variable and epoch
    % length
    clearvars -except n photo_files eeg_files time_stamp folderpath script_mode
    global sigma
    sigma=134.38
    epoch_length=5;

    % Get the experiment starting time for the current index
    % Get the EEG and Photometry file names for the current index
    % Create an output folder for the current index ( different folder for
    % each data file )
    start_time_of_day = time_stamp(n);
    filename_sleep  = eeg_files(n).name
    filename_photo  = photo_files(n).name
    filename_output = folderpath + "\" + filename_photo(1:end-4);
    mkdir(filename_output);

    % establish the size of the sleep dataset
    expdata_sleep=dlmread(folderpath + "\EEG\" + filename_sleep);
    sz_sleep=size(expdata_sleep);
    N_sleep=sz_sleep(1);

    % Based on the file format, if EEG bands are availible then unpack them,
    % else filter the raw EEG into bands
    % unpack the data into five vectors, time, theta/delta, delta power, EMG and EEG
    if(sz_sleep(2) == 5)
        sleep_time=expdata_sleep(:,1);
        theta_over_delta=smooth(expdata_sleep(:,2),1000);
        delta_power=smooth(expdata_sleep(:,3),1000);
        EMG=smooth(expdata_sleep(:,4),1000);
        EEG=expdata_sleep(:,5);
        EEG_PS(:,3) = theta_over_delta;
        EEG_PS(:,5) = delta_power;
    elseif((sz_sleep(2) >= 4) && (sz_sleep(2) <=7))
        EEG = expdata_sleep(:,1);
        EEG = highpass(EEG,0.5,200);
        sleep_time=0:0.005:0.005*(N_sleep-1);
        EEG_PS = EEGBand(EEG);
        theta_over_delta=EEG_PS(:,3);
        delta_power=EEG_PS(:,5);
        EMG = expdata_sleep(:,3);
        EMG = bandpass(EMG,[1 50],200);
        EMG = smooth(sqrt(EMG.^2),1000);
    else
        errordlg("Wrong file format!")
        return
    end
    %%
    % work out the maximum time in the EEG data
    sleep_timemax=max(sleep_time)
    % Import the photometry data
    expdata=dlmread(folderpath + "\Photometry\" + filename_photo);
    % establish the size of the photometry dataset
    sz=size(expdata);
    N=sz(1);
```

```
% unpack the data into two vectors, time and photometry
longtime=expdata(:,1);
photometry=expdata(:,2);
% work out the maximum time in the photometry data
photo_timemax = max(longtime);

% Trim the data to the data with the shortest length
if(photo_timemax>sleep_timemax)
  photo_timemax = sleep_timemax;
elseif(sleep_timemax>photo_timemax)
  sleep_timemax = photo_timemax;
end

% work out the photometry sampling rate
points_per_sec=1/(longtime(2)-longtime(1));

% Filter the data and identify the baseline
intensitydata = lowpass(photometry,0.1,points_per_sec);
xbl = 3540:3600:photo_timemax;
ybl = intensitydata(round(xbl*points_per_sec));
baseline=csapi(xbl,ybl,longtime);% interpolate the baseline with points at 200 Hz
smoothbaseline=smooth(baseline,400);% 400 sets the span over which the window smooths
difference=smoothbaseline-intensitydata;

% Trim the data for sleep scoring
% Calculate number of bleaches to analyse, include incomplete curves > ten minutes
photo_timemax = floor(photo_timemax/80)*80;
sleep_timemax = photo_timemax;
number_hours  = floor(photo_timemax/3600);
if(photo_timemax>(number_hours*3600+600))
    number_bleaches = ceil(photo_timemax/3600);
else
    number_bleaches = floor(photo_timemax/3600);
end

% If manual mode choose the starting bleach
% If automatic mode, start from bleach number 1
start_time = 0;
if(script_mode==1)
    index = round(start_time/3600);
elseif(script_mode==2)
    index = str2double(inputdlg("Enter the starting curve"))-1;
    if(index>number_bleaches)
        msgbox("Starting curve > total number of curves");
    end
end

% Sleep score the EEG data
% Obtain high and low (mu,var) for each scoring feature ( EMG, delta, Theta/Delta )
% parameters from the Gaussian Mixture Model
t = 80*200;
t_cnt = floor(sleep_timemax/80);
seg = 1:t*t_cnt;
l = size(EMG(seg));
y = l(1)./t;
EMG_temp = reshape(EMG(seg)',[t y]);
EMG_avg  = mean(EMG_temp);
GMModel = fitgmdist(EMG_avg',2);
[v i] = sort(GMModel.mu,'ascend');
mu(1,1) = GMModel.mu(i(1));
mu(2,1) = GMModel.mu(i(2));
var(1,1) = GMModel.Sigma(i(1));
var(2,1) = GMModel.Sigma(i(2));

delta_temp = reshape(delta_power(seg)',[t y]);
delta_avg  = mean(delta_temp);
GMModel = fitgmdist(delta_avg',2);
[v i] = sort(GMModel.mu,'ascend');
mu(1,2) = GMModel.mu(i(1));
mu(2,2) = GMModel.mu(i(2));
var(1,2) = GMModel.Sigma(i(1));
```

```
    var(2,2) = GMModel.Sigma(i(2));

    TD_temp = reshape(theta_over_delta(seg)',[t y]);
    TD_avg  = mean(TD_temp);
    GMModel = fitgmdist(TD_avg',2);
    [v i] = sort(GMModel.mu,'ascend');
    mu(1,3) = GMModel.mu(i(1));
    mu(2,3) = GMModel.mu(i(2));
    var(1,3) = GMModel.Sigma(i(1));
    var(2,3) = GMModel.Sigma(i(2));

    % Run the automatic sleep scoring algorithm
    [StageDist,SleepStage,prob] = SSscoring2(EEG_PS,EMG,1000,mu,var);

    % loop until every curve has been analysed
    while index < number_bleaches
        % Get the time of bleaching event for the current index ( each curve
        % lasts 60 minutes )
        time_of_bleach = index*3600+1;
        time_of_day = start_time_of_day + index;
        time_of_day = mod(time_of_day,24);

        % Get the time to start the analysis
        % Currently set to 35 seconds after bleach event
        start_time_for_analysis = time_of_bleach+35;
        start_index_for_EEG_analysis=round(start_time_for_analysis*200);

        % Get the start and end times for data plotting
        if((time_of_bleach-60)>=0)
            start_time = time_of_bleach-60;
        else
            start_time = 1;
        end

        if((time_of_bleach+3660)<=photo_timemax)
            end_time = time_of_bleach+3660;
        else
            end_time = photo_timemax;
        end

        % Convert the starting and end times to matrix indices
        % Do this for both EEG and photo data
        start2=round((start_time)*points_per_sec);
        stop2=round((end_time)*points_per_sec);

        start2_sleep=round((start_time)*200);
        stop2_sleep=round((end_time)*200);

        % Fix the plotting limits for the x-axes
        plot_limit_1=(start2/(60*points_per_sec))-1;
        plot_limit_2=(stop2/(60*points_per_sec))+1;

        % --------plotting and analysis of sleep data starts here-----------------

        % In this major section we plot the sscored stage, EEG bands and
        % photometry data for selected curve
        figure(100+index+1)
        clf
        set(gcf, 'Units', 'Normalized', 'OuterPosition', [0 0 1 1]);

        subplot(5,4,[9,10])

plot(sleep_time(start2_sleep:stop2_sleep)/60,delta_power(start2_sleep:stop2_sleep),'m','LineWidth
',2)
        xl=xlim;
        xlabel('Time (minutes)','FontSize',18)
        ylabel('Delta power','FontSize',18)

        subplot(5,4,[13,14])

plot(sleep_time(start2_sleep:stop2_sleep)/60,EMG(start2_sleep:stop2_sleep),'g','LineWidth',2)
```

```
        xlabel('Time (minutes)','FontSize',18)
        ylabel('EMG','FontSize',18)

        subplot(5,4,[17,18])

plot(sleep_time(start2_sleep:stop2_sleep)/60,theta_over_delta(start2_sleep:stop2_sleep),'LineWidt
h',2)
        xlabel('Time (minutes)','FontSize',18)
        ylabel('Theta/Delta','FontSize',18)

        subplot(5,4,[5,6])
        plot(longtime(start2:stop2)/60, -difference(start2:stop2),'c','LineWidth',2)
        text(0.1,0.9,filename_photo,'Units','normalized','Interpreter', 'none','FontSize',14)
        xlabel('Time (minutes)','FontSize',18)
        ylabel('Intensity','FontSize',18)
        stop_time_for_analysis = end_time-65;
        y = ylim;
        h = line([stop_time_for_analysis/60 stop_time_for_analysis/60],[y(1)
y(2)],'Color','red','LineStyle','--','LineWidth',2)
        title("");

        % Convert the starting and end times for analysis to matrix indices
        % Do this for both EEG and photo data
        stop_index_for_EEG_analysis=round(stop_time_for_analysis*200);
        start_index_for_sleep_scoring = round(start_time_for_analysis/5);
        stop_index_for_sleep_scoring = round(stop_time_for_analysis/5);

        % Find the photometry intensity after five minutes,
        % time taken to recover half of its original intensity
        % set value to -1 if curve does not reach half recovery
        five_minute_value    = -difference(round((start_time_for_analysis +
300)*points_per_sec));
        intensity_segment    = -difference(round((start_time_for_analysis-
6)*points_per_sec):round(stop_time_for_analysis*points_per_sec));
        bleached_value       = mean(-
difference(round((start_time_for_analysis)*points_per_sec):round((start_time_for_analysis+2)*poin
ts_per_sec)));
        I = find(intensity_segment>=(bleached_value/2));
        subplot(5,4,[5,6])
        if(~isempty(I))
            half_recovery_time_relative = I(1)/points_per_sec;
            half_recovery_time  =  start_time_for_analysis+half_recovery_time_relative;
            half_recovery_value =  intensity_segment(I(1));
            line([(start_time_for_analysis-30)/60 half_recovery_time/60],[half_recovery_value
half_recovery_value],'Color','red','LineStyle','-','LineWidth',2)
            line([half_recovery_time/60 half_recovery_time/60],[bleached_value
half_recovery_value],'Color','red','LineStyle','--','LineWidth',2)
        else
            half_recovery_time_relative = -1;
        end

        line([(start_time_for_analysis-30)/60 (time_of_bleach + 300)/60],[five_minute_value
five_minute_value],'Color','red','LineStyle','--','LineWidth',2)
        line([(time_of_bleach + 300)/60 (time_of_bleach + 300)/60],[bleached_value
five_minute_value],'Color','red','LineStyle','-','LineWidth',2)

        % Work out sleep scoring percentages (NREM, REM, Wake)
        % For the times chosen, whole curve and whole data set
        if(start_index_for_sleep_scoring+720<length(SleepStage))
            SleepStageSeg60  =
SleepStage(start_index_for_sleep_scoring:start_index_for_sleep_scoring+720);
        else
            SleepStageSeg60  = SleepStage(start_index_for_sleep_scoring:end);
        end
        SleepStageSeg    =
SleepStage(start_index_for_sleep_scoring:stop_index_for_sleep_scoring);
        % expand the sleep stage matrix for 5 seconds/sample to 200Hz for plotting
        SleepStagePlot = kron(SleepStage,ones(1,1000));

        % work out the percentage of NREM, REM and WAKE
        ProbPlot = kron(prob,ones(1,1000));
```

```
        total_percentage_WAKE = 100*sum(SleepStage==1)./length(SleepStage);
        total_percentage_NREM = 100*sum(SleepStage==2)./length(SleepStage);
        total_percentage_REM  = 100*sum(SleepStage==3)./length(SleepStage);

        percentage_WAKE_60 = 100*sum(SleepStageSeg60==1)./length(SleepStageSeg60);
        percentage_NREM_60 = 100*sum(SleepStageSeg60==2)./length(SleepStageSeg60);
        percentage_REM_60  = 100*sum(SleepStageSeg60==3)./length(SleepStageSeg60);

        percentage_WAKE  = 100*sum(SleepStageSeg==1)./length(SleepStageSeg);
        percentage_NREM  = 100*sum(SleepStageSeg==2)./length(SleepStageSeg);
        percentage_REM   = 100*sum(SleepStageSeg==3)./length(SleepStageSeg);
        percentage_SLEEP = percentage_NREM+percentage_REM;

        % Stop times for calculating different diffusion coefficients
        % Calculate using the whole curve, first five minutes
        % time taken to recover half intensity and first minute
        stop_time_for_D(1) = stop_time_for_analysis;
        stop_time_for_D(2) = start_time_for_analysis+300;
        if(~isempty(I))
            stop_time_for_D(3) = half_recovery_time;
        else
            stop_time_for_D(3) = -1;
        end
        stop_time_for_D(4) = start_time_for_analysis+60;

        %---------------the diffusion coefficient calculation follows-----------
        error = zeros(1,4);
        % Now we use the code from Gifford_fit_1 to calculate D but first write
        % vectors for the segment of data to be analysed
        for t=1:3
            start_index_for_analysis=round(start_time_for_analysis*points_per_sec);
            stop_index_for_analysis=round((stop_time_for_D(t))*points_per_sec);

            time=longtime(start_index_for_analysis:stop_index_for_analysis); %Set the time
segment
            Aintensitydata=-difference(start_index_for_analysis:stop_index_for_analysis); % Now
set the intensity data

            % We want to have the first point being 0 seconds in time and 0 intensity
            % so we make it so:

            timedata=time-time(1);
            intensitydata_D=Aintensitydata-Aintensitydata(1);

            % Establish the length of the dataset and the maximum time in seconds
            sz=size(expdata); % This is the dimensions of the matrix
            max_timedata=max(timedata); % This is largest value of time in the time series (the
last point)

            time=timedata;% Create a vector time which is identical to timeedata (just to
distinguish between
            % the experimental data and the theoretical curve
            initialparameters=[100 1];% Set and initial value for the diffusion coefficient D and
scale factor

            % We now fit the data to the integrated Gifford equation, plus a scale factor
            % "Scale_factor" which will held in "parameters(2)"
            % "Diffusion_coefficient" is held in "parameters(1)"
            try
                parameters = lsqcurvefit(@Gifford,initialparameters,timedata,intensitydata_D);%
Get a LSQRS estimate for D and scalefactor
                D(t) = parameters(1);
                Scale_factor=parameters(2);

                intensity=Gifford(parameters,time); % This calculates the theoretical curve using
the LSQRS fit parameters

                % We now calculate the final (t=infinity) value of the fit determined by
                % the function Giffordend
                intensityend=Giffordend(parameters);
                % Next we scale the experimental data and the fitted data curve such that
```

```
                % the last value in the data set is equal to the value the theoretical curve
                % should have given the fitted parameters
                intensity_pred(t).values = intensity/parameters(2);
                intensity_pred(t).time   = time;
                intensity_act(t).values  = intensitydata_D/parameters(2);
                intensity_act(t).time    = time;
            catch
                D(t) = -1;
            end

        end
        %---------------the diffusion coefficient calculation follows-----------
        start_index_for_analysis=round(start_time_for_analysis*points_per_sec);
        stop_index_for_analysis=round((stop_time_for_D(4))*points_per_sec);

        time=longtime(start_index_for_analysis:stop_index_for_analysis); %Set the time segment
        Aintensitydata=-difference(start_index_for_analysis:stop_index_for_analysis); % Now set
the intensity data

        %Now the Gifford code

        % Now we normalise the data so that:
        % 1) It starts at 0,0 and
        % 2) The scale is such that the Intensity_just_before_bleaching =1
        time = time - time(1);
        intensitydata = Aintensitydata - Aintensitydata(1);
        %=Bintensitydata/(intensity_just_before_bleaching - Bintensitydata(1));

        % Give values for sigma and R in microns (normally we will set these to be equal
        R=sigma;

        % Take the first 60 seconds, so first work out the number of points
        initial_segment_time=time;
        initial_segment_intensity_data=intensitydata;

        % Set up the least square fit using a 2nd order polynomial
        fun=@(parameters,initial_segment_time)
parameters(1)+parameters(2).*initial_segment_time+parameters(3).*initial_segment_time.*initial_se
gment_time
        initialparameters=[0.01,0.01,0.001]; % Initial parameters, that probably don't matter
much
        try
            parameters =
lsqcurvefit(fun,initialparameters,initial_segment_time,initial_segment_intensity_data);
            initial_segment_theory=fun(parameters,initial_segment_time);
            initial_slope=parameters(2); % This is the fit least-squares value for the initial
slope
            % Now we convert this to a value for D using equation [6] of the paper
            term=(sqrt(pi*exp(1)*0.5)*erf(1/sqrt(2))-1);
            D(4)=initial_slope*sigma*sigma*term;
            intensity_pred(4).values = initial_segment_theory;
            intensity_pred(4).time   = initial_segment_time;
            intensity_act(4).values  = intensitydata;
            intensity_act(4).time    = time;
        catch
            D(4) = -1;
        end
        %-------------finally we output all the data calculated-----------------
        % Plot the curve for each D calculated
        if (D(1)>0)
            subplot(5,4,[3,7]) % final Gifford plot
            plot(intensity_act(1).time/60,intensity_act(1).values,'b','LineWidth',0.5);
            xlabel('Time (minutes)','FontSize',18)
            ylabel('Normalised 1- M(t)/M(0)','FontSize',18)
            hold on
            plot(intensity_pred(1).time/60,intensity_pred(1).values,'--r','LineWidth',3);
            text(0,0.15,sprintf('DfitF(microns^2 per second)
= %.2f',D(1)),'Units','normalized','FontSize',12)
            text(0,0.05,sprintf('Sigma (microns)
= %.2f',sigma),'Units','normalized','FontSize',12)
```

```
            text(0,0.25,sprintf('Bleach time
=  %.2f',start_time_for_analysis),'Units','normalized','FontSize',12)
        end

        if (D(2)>0)
            subplot(5,4,[4,8]) % final Gifford plot
            plot(intensity_act(2).time/60,intensity_act(2).values,'b','LineWidth',0.5);
            xlabel('Time (minutes)','FontSize',18)
            ylabel('Normalised 1- M(t)/M(0)','FontSize',18)
            hold on
            plot(intensity_pred(2).time/60,intensity_pred(2).values,'--r','LineWidth',3);
            text(0,0.15,sprintf('Dfit5(microns^2 per second)
= %.2f',D(2)),'Units','normalized','FontSize',12)
            text(0,0.05,sprintf('Sigma (microns)
= %.2f',sigma),'Units','normalized','FontSize',12)
            text(0,0.25,sprintf('Bleach time
=  %.2f',start_time_for_analysis),'Units','normalized','FontSize',12)
        end

        if (D(3)>0)
            subplot(5,4,[11,15]) % final Gifford plot
            plot(intensity_act(3).time/60,intensity_act(3).values,'b','LineWidth',0.5);
            xlabel('Time (minutes)','FontSize',18)
            ylabel('Normalised 1- M(t)/M(0)','FontSize',18)
            hold on
            plot(intensity_pred(3).time/60,intensity_pred(3).values,'--r','LineWidth',3);
            text(0,0.15,sprintf('DfitH (microns^2 per second)
= %.2f',D(3)),'Units','normalized','FontSize',12)
            text(0,0.05,sprintf('Sigma (microns)
= %.2f',sigma),'Units','normalized','FontSize',12)
            text(0,0.25,sprintf('Bleach time
=  %.2f',start_time_for_analysis),'Units','normalized','FontSize',12)
        end

        if (D(4)>0)
            subplot(5,4,[12,16]) % final Gifford plot
            plot(intensity_act(4).time/60,intensity_act(4).values,'b','LineWidth',0.5);
            xlabel('Time (minutes)','FontSize',18)
            ylabel('Normalised 1- M(t)/M(0)','FontSize',18)
            hold on
            plot(intensity_pred(4).time/60,intensity_pred(4).values,'--r','LineWidth',3);
            text(0,0.15,sprintf('DfitI (microns^2 per second)
= %.2f',D(4)),'Units','normalized','FontSize',12)
            text(0,0.05,sprintf('Sigma (microns)
= %.2f',sigma),'Units','normalized','FontSize',12)
            text(0,0.25,sprintf('Bleach time
=  %.2f',start_time_for_analysis),'Units','normalized','FontSize',12)
        end

        subplot(5,4,[1,2]) % final sleep stage plot

plot(sleep_time(start_index_for_EEG_analysis:stop_index_for_EEG_analysis)/60,SleepStagePlot(start
_index_for_EEG_analysis:stop_index_for_EEG_analysis),'-r','LineWidth',3);
        xlabel('Time (minutes)','FontSize',18)
        ylabel('Sleep stage','FontSize',18)
        ylim([0 4])
        xlim([xl(1) xl(2)]);
        text(0.75,0.85,sprintf('Epoch time (secs)
= %.1f',epoch_length),'Units','normalized','FontSize',12)

        % now write out the vigilance state percentages
        text(0.70,0.6,sprintf('Percent WAKE
= %.2f',percentage_WAKE_60),'Units','normalized','FontSize',12)
        text(0.70,0.4,sprintf('Percent NREM
= %.2f',percentage_NREM_60),'Units','normalized','FontSize',12)
        text(0.70,0.2,sprintf('Percent REM
= %.2f',percentage_REM_60),'Units','normalized','FontSize',12)
        text(0.70,1.1,sprintf('Duration Selected = %.2f',stop_time_for_analysis-
start_time_for_analysis),'Units','normalized','FontSize',12)
```

```
        text(0.0,0.1,sprintf('%% SLEEP
= %.1f',percentage_SLEEP),'Units','normalized','FontSize',12)
        text(0.2,0.1,sprintf('%% WAKE
= %.1f',percentage_WAKE),'Units','normalized','FontSize',12)
        text(0.4,0.1,sprintf('%% NREM
= %.1f',percentage_NREM),'Units','normalized','FontSize',12)
        text(0.6,0.1,sprintf('%% REM = %.1f',percentage_REM),'Units','normalized','FontSize',12)

        text(0.02,0.25,'WAKE','Units','normalized','FontSize',18)
        text(0.02,0.5,'NREM','Units','normalized','FontSize',18)
        text(0.02,0.75,'REM','Units','normalized','FontSize',18)
        text(0.1,0.9,filename_sleep,'Units','normalized','FontSize',14,'Interpreter', 'none')

        % Store the figure as a png
        filename_figure = filename_output +"\" +"figure"+num2str(100+index+1);
        print(figure(100+index+1),filename_figure,'-dpng')% Save the figure as a .png file
        saveas(figure(100+index+1),filename_figure)
        close(figure(100+index+1));
        %%
        %------------------ Write data to an excel spreadsheet ------------

        % The duration of analysis
        Duration = stop_time_for_analysis-start_time_for_analysis;
        filename_sleep;
        filename_photo;

        % The real time at which the current bleaching event occurs
        if((time_of_day>=4) && (time_of_day<16))
            lights_on = 'Off'
        else
            lights_on = 'On'
        end

        % Calculate if the first transistion in sleep stage occurs after
        % five minutes or half intensity recovery time
        SleepStageTranSeg =
SleepStage(1,round(start_time_for_analysis/5):round(stop_time_for_analysis/5))
        s_sz = size(SleepStageTranSeg);
        first_tran_time=0;
        for s=1:s_sz(2)-1
            prev = SleepStageTranSeg(1,s)
            curr = SleepStageTranSeg(1,s+1)
            if (curr~=prev)
                first_tran_time = s*5;
                break;
            end
        end
        first_tran_text="";
        five_minute_text="No";
        half_recovery_text="No";
        tran = 0;
        if(first_tran_time>=half_recovery_time_relative)
            half_recovery_text = "Yes";
            tran = 1;
        end
        if(first_tran_time>=300)
            five_minute_text = "Yes";
            tran = 1;
        end

        % Print out the first transition in the sleep stage
        if(tran==1)
            if(prev==1)
                first_tran_text = "Wake"
            end
            if(prev==2)
                first_tran_text = "NREM"
            end
            if(prev==3)
                first_tran_text = "REM"
            end
```

```
        end

        % Append all data to the excel spreadsheet
        data = table(string(filename_sleep),string(filename_photo),index+1, percentage_WAKE_60,
percentage_NREM_60, percentage_REM_60,percentage_WAKE,...
            percentage_NREM,percentage_REM,Duration,total_percentage_WAKE, total_percentage_NREM,
total_percentage_REM,five_minute_value,half_recovery_time_relative,...

D(1),D(2),D(3),D(4),time_of_day,string(lights_on),first_tran_time,string(five_minute_text),string
(half_recovery_text),string(first_tran_text),'VariableNames',{'SleepFileName','PhotoFileName','Bl
each_No','Wake', 'NREM', 'REM', 'Wake_Total', 'NREM_Total',...

'REM_Total','Duration','Wake_ALL','NREM_ALL','REM_ALL','Five_Minute_Value','Half_Recovery_Time','
D_Full','D_Five','D_Half_Recov','D_initial','Time_Of_Day','Lights_On','First_Trans_Time','5min','
Half','First_Trans_Stage'});

        excel_filename = filename_output + "\data.xlsx"
        writetable(data,excel_filename,'Sheet','Data',"WriteMode","append");

        excel_filename_combined = "Data_Combined.xlsx"
        writetable(data,excel_filename_combined,'Sheet','Data',"WriteMode","append");
        index = index+1;
    end
end
% Now close the redundant figure windows
if ishandle(figure(2000))
    close(2000)
end

function [StageDist, Stage_out, prob] = SSscoring2(EEG,EMG,noSamples,mu,sigma)
% Function for scoring the EEG data into sleep stages
j = 1;
tp = 0;
fp = 0;
fn = 0;
tn = 0;

% Trim data if EEG and EMG data are different lengths
eegl = length(EEG)/noSamples;
emgl = length(EMG)/noSamples;
if(eegl<emgl)
   L = eegl;
   max = length(EEG);
else
   L = emgl;
   max = length(EMG);
end

% Run until all epochs have been scored
% Take 1000 samples on every loop ( = 5 seconds )
StageDist = zeros(2,3);
prevStage = 1;
offset = 1000; % Controls how fragmented the scoring is
               % Higher values = less fragmentation
for i = 0:1:L-1

   % Work out the starting and ending indices to take data from
   index = i*noSamples;
   if((index-offset)<=0)
   start_idx = 0;
   stop_idx  = index+offset;
   elseif((index+offset)>=max)
   start_idx = index-offset;
   stop_idx  = max;
   else
   start_idx = index-offset;
   stop_idx  = index+offset;
   end

   % Calculate the average value of each feature for the current epoch
   ThetaAvg = mean(EEG(start_idx+1:stop_idx,4));
```

```
   DeltaAvg = mean(EEG(start_idx+1:stop_idx,5));
   EMGAvg   = mean(EMG(start_idx+1:stop_idx,1));
   TDAvg    = ThetaAvg/DeltaAvg;

    % Score the epoch using scoring templates based of mixture of Z-scores
    prob(1,j) =   -1.0*( ((mu(1,1)-EMGAvg)/(sqrt(sigma(1,1)))) + ((mu(2,1)-
EMGAvg)/(sqrt(sigma(2,1)))) );
    prob(2,j) =   0.4*( ((mu(1,1)-EMGAvg)/(sqrt(sigma(1,1)))) + ((mu(2,1)-
EMGAvg)/(sqrt(sigma(2,1)))) )  - 0.6*( ((mu(1,2)-DeltaAvg)/(sqrt(sigma(1,2)))) + ((mu(2,2)-
DeltaAvg)/(sqrt(sigma(2,2)))) );
    prob(3,j) =   0.1*( ((mu(1,1)-EMGAvg)/(sqrt(sigma(1,1)))) + ((mu(2,1)-
EMGAvg)/(sqrt(sigma(2,1)))) ) - 0.9*( ((mu(1,3)-TDAvg)/(sqrt(sigma(1,3)))) + ((mu(2,3)-
TDAvg)/(sqrt(sigma(2,3)))) );

   [val idx] = sort(prob(:,j),'desc');
   scoredStage = idx(1);

    % REM can not occur if previous stage is not REM or NREM
   if((scoredStage==3)&&(prevStage==1))
       scoredStage = idx(2);
   end
   prevStage = scoredStage;
   StageDist(1,scoredStage) = StageDist(1,scoredStage)+1;
   Stage_out(j) = scoredStage;
   j = j + 1;

end
end



function [DataFIR] = EEGBand(DataRaw)
% Function for filtering the EEG signal into bands ( delta, theta )
%%
smoothF = 1;
for i=1:size(DataRaw,3)
    % First round values to nearest integers
    EEGRaw = round(DataRaw);

    % Use MATLAB's bandpass filters
    % 1-4 Hz for Delta
    % 5-10 Hz for Theta
    DataDelta = round(bandpass(EEGRaw,[1 4],200));
    DataDelta = DataDelta.^2;
    DataTheta = round(bandpass(EEGRaw,[5 10],200));
    DataTheta = DataTheta.^2;

    % Smooth the data and store into a matrix
    DataFIR(:,4,i) = smooth(DataTheta,1000);
    DataFIR(:,5,i) = smooth(DataDelta,1000);
    DataFIR(DataFIR(:,5,i)==0,5,i) = 1;
    DataFIR(:,3,i) = DataFIR(:,4,i)./DataFIR(:,5,i);

end
end

function intensity=Gifford(parameters,time)
global sigma
% This function computes the integrated Gifford equation using specified
% values of sigma and R
R=sigma;
% First calculate M(t)
term1=4*parameters(1)*time+2*sigma*sigma;
term2=2*parameters(1)*time+sigma*sigma;
term3=R*R./(term1);
term4=sqrt(term3);
term5=sqrt(pi*(term2)/2);
term6=R*exp(-term3);
term7=4*pi*sigma*sigma*sigma./sqrt(term2);
term8=erf(term4);
```

```
M=term7.*(term5.*term8-term6);

% Next calculate M(0)
zeroterm1=2*sigma*sigma;
zeroterm2=sigma*sigma;
zeroterm3=R*R./(zeroterm1);
zeroterm4=sqrt(zeroterm3);
zeroterm5=sqrt(pi*(zeroterm2)/2);
zeroterm6=R*exp(-zeroterm3);
zeroterm7=4*pi*sigma*sigma*sigma./sqrt(zeroterm2);
zeroterm8=erf(zeroterm4);
M0=zeroterm7.*(zeroterm5.*zeroterm8-zeroterm6);

intensity=parameters(2)*(1-M/M0);
end

function intensityend=Giffordend(parameters)
global sigma

% This function computes the integrated Gifford equation at infinite time using specified
% values of sigma and R
R=sigma;

timeend=1e6; % This is, effectively, infinity time
% First calculate M(t)
term1=4*parameters(1)*timeend+2*sigma*sigma;
term2=2*parameters(1)*timeend+sigma*sigma;
term3=R*R./(term1);
term4=sqrt(term3);
term5=sqrt(pi*(term2)/2);
term6=R*exp(-term3);
term7=4*pi*sigma*sigma*sigma./sqrt(term2);
term8=erf(term4);
M=term7.*(term5.*term8-term6);

% Next calculate M(0)
zeroterm1=2*sigma*sigma;
zeroterm2=sigma*sigma;
zeroterm3=R*R./(zeroterm1);
zeroterm4=sqrt(zeroterm3);
zeroterm5=sqrt(pi*(zeroterm2)/2);
zeroterm6=R*exp(-zeroterm3);
zeroterm7=4*pi*sigma*sigma*sigma./sqrt(zeroterm2);
zeroterm8=erf(zeroterm4);
M0=zeroterm7.*(zeroterm5.*zeroterm8-zeroterm6);

intensityend=parameters(2)*(1-M/M0);
end
```